NOTE TO USERS

DISSERTATION

THE METHOD OF CHARACTERISTICS AND COMPUTATIONAL FLUID DYNAMICS APPLIED TO THE PREDICTION OF UNDEREXPANDED JET FLOWS IN ANNULAR GEOMETRY

Submitted by

Sangwon Kim

Department of Mechanical Engineering

In partial fulfillment of the requirements

for the Degree of Doctor of Philosophy

Colorado State University

Fort Collins, Colorado

Summer, 2005

COLORADO STATE UNIVERSITY

December 20, 2004

WE HEREBY RECOMMEND THAT THE DISSERTATION PREPARED UNDER OUR SUPERVISION BY SANGWON KIM ENTITLED THE METHOD OF CHARACTERISTICS AND COMPUTATIONAL FLUID DYNAMICS APPLIED TO THE PREDICTION OF UNDEREXPANDED JET FLOWS IN ANNULAR GEOMETRY FOR THE DEGREE OF DOCTOR OF PHILOSOPHY.

Committee on Graduate Work

Adviser

Department Head

ABSTRACT OF DISSERTATION

THE METHOD OF CHARACTERISTICS AND COMPUTATIONAL FLUID DYNAMICS APPLIED TO THE PREDICTION OF UNDEREXPANDED JET FLOWS IN ANNULAR GEOMETRY

Natural gas engine efficiency can be improved by enhancing fuel-air mixing through an injection pressure increase. To achieve this mixing benefit, experiments show that a high pressure (3.4 MPa) injection valve needs a shroud to direct the supersonic fuel jet toward the center of the cylinder. Since the fuel jet issuing from the shroud valve has a nearly annular jet flow configuration, it is necessary to analyze the annular jet flow to understand the fuel jet behavior in the mixing process and to improve the shroud design for better mixing. The method of characteristics (MOC) was used as the primary modeling algorithm in this work because the MOC has distinct advantages in computing supersonic flows, notably speed of computation, shock wave capturing and ease of physical interpretation. Computational Fluid Dynamics (CFD) was used primarily to validate the MOC results.

A consistent process for dealing with the coalescence of compression characteristic lines into a shock wave during the method of characteristics (MOC) computation was developed. In the MOC results for axisymmetric jet flow, the incident shock wave discontinuity was clearly shown. By the application of shock polar in the pressure-flow angle plane to the incident shock wave for an axisymmetric underexpanded jet, the von Neumann and detachment criteria for the incident

shock was compared with the triple point location found in experimental results. It was found that, in the nozzle-exit-to-ambient-static pressure ratios of 2 - 50, a triple point of the axisymmetric jet was located at the point where the flow angle after the incident shock became $-5°$ relative to the axis and this point was situated between the von Neumann and detachment criteria on the incident shock. In addition, the computations showed that the static pressure ahead of the incident shock formed in a sonic jet, when plotted as a function of axial distance, falls on the same curve for pressure ratios of 2 - 50.

MOC computations of the jet flow with annular geometry were performed for pressure ratios of 10 and 20 with $r_{annulus}$ = 10 - 50 units, $\triangle r$ = 2 units. In this pressure ratio range, the MOC results did not predict a Mach disc in the core flow of the annular jet, but did indicate the formation of a Mach disc where the jet meets the axis of symmetry. The MOC results display the annular jet configurations clearly. An outer incident shock much stronger than an inner incident shock in the annular jet flow was seen to occur.

Three types of nozzles for application to gas injectors (convergent-divergent nozzle, conical nozzle, and aerospike nozzle) were designed using the MOC and evaluated in on- and off-design conditions using CFD. The average axial momentum per unit mass was improved by 17 to 24 % and the average kinetic energy per unit fuel mass was improved by 30 to 80 % compared with a standard shrouded poppet valve. Of the candidate designs, the convergent-divergent nozzle gave the best performance.

Sangwon Kim
Department of Mechanical Engineering
Colorado State University
Fort Collins, Colorado 80523
Summer, 2005

ACKNOWLEDGEMENTS

The author wishes to express his sincere appreciation to his major professor, Charles E. Mitchell, for his guidance and suggestions in the direction of this research. Gratitude is also extended to Professor Allan T. Kirkpatrick, Professor Bryan D. Willson, and Professor Robert N. Meroney for serving as a member of the author's final examination committee. The author offers his heartfelt thanks to Professor Grant Lee and Ms. Grace Lee, Dr. Hyosup Woo and Ms. Sangyong Woo, Dr. Yo-Jun Song and Ms. Eun-Joo Song, Rev. Randy Sung Ju and Ms. Hannah Ju, Professor Robert W. Woody and Dr. A-Young Woody for their thoughtful help and favor. The author would like to thank all his friends, Gi-heon Kim, Jinsoo Uh, Jinchul Joo, Moo-Sup Eom, Yoong-Goog Cho, Sang-Hun Lim, Byung-Kwan Cho, Jang-Hi Lim and all Korean Student Christian Fellowship members for their helpful assistance and friendship.

The author is deeply grateful to his parents, Soo-Han Kim and Hyung-Ja Park, his parents-in-law, Boo-Jo Kang and Hae-Young Park and his brothers and sisters, Mi-Jung Kim, Mi-Hyang Kim, Mi-Jin Kim, Sung-Il Kim, and Dong-Gyun Kang for their loving care and prayer.

The author also owes gratitude to his beloved wife, Minjeong Kang, for her understanding and support which made this research possible.

Finally, the author gives thanks to God.

Contents

List of Figures

Chapter 1

Introduction

Natural gas fueled engines have been widely used in industries such as gas compression and electric power generation for many years. The basic features of natural gas fueled engines for industrial applications are a large bore ($\geq$ 0.3 m) and operated at slow speed ($\leq$ 500 rpm). The most common configuration of the natural gas fueled engines is a two stroke cycle with direct injection of natural gas into the cylinder. Natural gas is injected into the engine cylinder through the poppet valve, which is actuated mechanically or electronically. The design of the fuel injection system of the natural gas fueled engines has been barely changed through the years and the effect of the poppet valve on the mixing of the natural gas with the air in the cylinder is still not fully understood.

Natural gas is typically injected at low pressure (0.4 MPa) although natural gas pipelines operate at high pressure, of the order of 3.4 MPa. Consequently it is reasonable to consider the use of the high pressure pipeline gas for direct injection into the engine cylinder. When the natural gas is injected at high pressure (3.4 MPa), the resulting fuel jet can have significantly more momentum and kinetic energy than in conventional low pressure (0.4 MPa) injection systems. It is hypothesized that the impact of the high pressure natural gas jet with the piston top creates both large scale mixing and vigorous small scale turbulent structures. As consequence the fuel-air mixing inside the cylinder of natural gas fueled engines may be enhanced.

Many studies of the injection and mixing of the natural gas into the engine cylinder have been conducted at the Engines and Energy Conversion Laboratory of Colorado State University. Olsen *et al.* [35] investigated the fuel injection process for low pressure (0.4

MPa) and high pressure (3.4 MPa) gas injection valves using planar laser induced florescence (PLIF) and showed that for a high pressure valve the primary mixing occurs after piston impingement while the low pressure valve achieves more effective mixing during jet penetration. Kim *et al.* [36] computed the fuel-air mixing process of a low pressure (0.4 MPa) and a high pressure (3.4 MPa) injection valve numerically and concluded that high pressure injection produces significantly better mixing at the top dead center position compared to low pressure injection.

For high pressure injection, shrouds have been employed around the poppet valve to direct the supersonic fuel jet into the center of the cylinder and onto the piston surface. However, these shrouds can cause a significant loss of stagnation pressure if they are not carefully designed to accelerate the flow to a supersonic condition isentropically. Both shock waves and flow separation may occur, resulting in substantial flow losses. It is necessary to replace the simple shroud with an efficient fuel injection nozzle designed to improve performance and reduce flow losses.

Steady, subsonic flow is defined by elliptic partial differential equations and steady, supersonic flow is defined by hyperbolic partial differential equations. In supersonic flow, the phenomena are essentially those of wave propagation, in which disturbances at individual points of the flow are propagated along the downstream Mach lines passing through these points. The method of characteristics is a highly developed method for the solution of inviscid supersonic flows, for which the governing flow equations are hyperbolic partial differential equations (PDE). For many years the method of characteristics was the only method used for solving practical problems described by hyperbolic PDEs.

Prandtl and Busemann were the first to use the method of characteristics (MOC) to compute supersonic two dimensional flow. Subsequently Frankl, Ferrari, Guderley and Sauer used the method of characteristics for determining the supersonic phenomena for flow with axial symmetry and every type of boundary condition, assuming potential flow. Ferri [6] extended the method of characteristics to the rotational flow behind an oblique shock by use of the stream function, as suggested by Crocco, instead of the potential function for the differential equation of motion.

Pack [7] computed the flow conditions in a steady two-dimensional jet using the method

of characteristics and interpreted the intersection of characteristics of the same family as the origin of a shock wave and explained the development of the incident shock formed by the reflection of compression waves from the jet boundary by an application of the equations of flow through an oblique discontinuity. He stated that Mach disc starts to appear at higher pressure ratio in two-dimensional jet than in axisymmetric jet.

Adamson and Nichols [9] suggested an approximate method of calculating the position of the first normal shock in the jet flow behind highly underexpanded nozzles using the method of characteristics based on calculations upstream of the shock. The approximate method assumed that the axial location of the normal shock was that point at which the static pressure behind the shock was equal to the atmospheric pressure. However, its validity is limited to relatively low nozzle-exit-to-ambient pressure ratios and supersonic Mach numbers at the nozzle exit, and does not yield detailed information of the over-all flowfield.

Eastman and Radtke [10] suggested that the location of the normal shock waves coincided with the point where the static pressure downstream of the incident shock wave was minimum. The static pressure is an insensitive parameter behind the incident shock because the largest static pressure drop (90%) occurs at the nozzle exit and the static pressure varies in a relatively narrow range behind the incident shock.

Abbett [12] proposed a criterion for locating the Mach disc, which is a normal shock that forms on the axis of symmetry. Abbett's criterion is that the triple point Mach disc location reflects quantitatively the interaction between the subsonic core and supersonic outer flow downstream of the Mach disc and is determined by the requirement that the centerline core flow, which is subsonic just downstream of the Mach disc, must pass smoothly through a throat-like region where the flow becomes supersonic. However, Abbett's criterion required a complex iterative process for locating a Mach disc in the characteristic net and assumed that the central core flow behind the Mach disc is uniform one-dimensional flow. Therefore Abbett's criterion is not adequate for the high pressure ratio. Fox [14, 19] and Chang [15, 20], respectively, applied Abbett's criterion to pressure ratios less than 16.

Love and Grigsby [5] conducted comprehensive experimental and theoretical studies of the structure of the jet flow behind nozzles of various configurations. In their theoretical work they did not consider the entropy change across the incident shock and used the "foldback

method" (neglecting the weaker characteristic line, see Ref. [4] for detail explanation) for the coalescence of the characteristic lines of the same family. Their experimental results remain the most comprehensive available and are used to validate the analytical solutions of this dissertation.

Von Neumann [22] first proposed that both regular reflection (RR) and Mach reflection (MR) are feasible in a discrete range of an incident shock angle, α_i. When the incident shock angle is small enough, the incident shock can be reflected regularly at the surface (Regular reflection), but when the incident shock angle is larger than certain value, the reflected shock is detached from the surface and Mach stem is formed between the reflected shock and the surface (Mach reflection). The lower limit of the range is denoted as the von Neumann criterion angle, α_N, and the upper limit of the range is denoted as the detachment criterion angle, α_D. Theoretically, RR is not possible for $\alpha > \alpha_D$ and MR is not possible for $\alpha < \alpha_N$. In the range of $\alpha_N \leq \alpha \leq \alpha_D$, which is known as the dual solution domain, both RR and MR are theoretically possible.

Hornung *et al.* [23] first hypothesized that a hysteresis in the RR→MR transition would occur at the detachment criterion angle, α_D, whereas the reversed MR→RR transition would take place at the von Neumann criterion angle, α_N. Shock reflection hysteresis was verified experimentally by Chpoun *et al.* [25] and numerically by Ivanov *et al.*[27] using the direct simulation Monte Carlo (DSMC) method and by Vullion *et al.* [26] using a Flux-Corrected Transport (FCT) -based algorithm respectively. Li *et al.* [28] showed analytically that the RR is stable in most of the dual solution domain, $\alpha_N \leq \alpha \leq \alpha_D$, by applying the principle of minimum entropy production.

In engines with natural gas direct injection at high pressure, the injected natural gas flows over the poppet valve, which acts as a bluff body, producing a more or less annular type flow pattern into the cylinder. It is necessary to analyze the annular supersonic jet to understand the mixing process of natural gas fueled engines. To date the method of characteristics has not been applied to this kind of underexpanded jet with annular geometry. The objective of the research is 1) the analysis of the shock wave development in the axisymmetric underexpanded jet, 2) the application of the method of the characteristics to the underexpanded jet with annular geometry, and 3) the use of the MOC and CFD for

development of nozzles for high pressure (3.0 MPa) injection poppet valves to enhance the performance of natural gas engines.

This dissertation is structured as follows. The theoretical background of this dissertation is presented in Chapter 2. The method of characteristics is explained in detail with the derivation of the compatibility equations and the characteristics for axisymmetric rotational flow. Shock wave phenomena are explained with emphasis on the shock wave treatment in the characteristic net. In Chapter 3, results from MOC and CFD for the axisymmetric underexpanded jet analysis are presented. A criterion for locating the triple point on the incident shock wave is developed and the relations between the nozzle-exit-to-ambient pressure ratio and the axial location of a triple point in terms of a mathematical expression are presented. Also, MOC results are compared with experimental results and FLUENT calculations. In Chapter 4, the results of the annular underexpanded jet analysis are presented. The differences between the axisymmetric jet and the annular jet are discussed and MOC results are compared with FLUENT calculations. In Chapter 5, nozzle designs for high pressure injection valves are presented and the enhancement of the newly designed nozzles are validated by comparing the average axial momentum and average kinetic energy per unit fuel mass. Finally, the conclusions are summarized in Chapter 6.

Chapter 2

Theory

2.1. The Method of Characteristics for Axisymmetric Rotational Flow

Steady, supersonic flow is governed by hyperbolic partial differential equations. For hyperbolic PDEs, the flow properties at each point in the flow field depend on those properties in a finite region of the upstream flow field, but are independent of the downstream conditions. Thus marching-type numerical methods may be applied for obtaining the solutions to such flow fields. The most accurate marching-type method applicable to hyperbolic PDEs is the method of characteristics. Since the solution of hyperbolic PDEs is determined along characteristics, the important properties of the exact solution are preserved in the numerical solution. The method of characteristics can be adapted easily to the computation of problems that contain discontinuities, such as shock waves in supersonic flow. Also, the method of characteristics is very fast in numerical computation and therefore good as a tool for designing efficient nozzles.

2.1.1. Flow conditons

From kinetic theory, the kinematic viscosity of a gas is $\nu \simeq al$, where l is the mean free path for collision and the sound speed, a, represents the mean thermal molecular velocity. Since the characteristic fluid velocity, U, is the order of the sound speed or larger, the Reynolds number scales as

$$Re = \frac{UL}{\nu} = \frac{UL}{al} > \frac{L}{l} \tag{2.1}$$

L is the characteristic length for the flow. Since $L \gg l$, the Reynolds number is large and this means for supersonic flows that viscous forces are small compared to inertial forces and can be ignored except in highly localized regions of the flow. Kirkpatrick *et al.* (2001) showed through numerical computation that the effects of viscosity and turbulence on the supersonic jet structure are not significant for high nozzle-exit-to-ambient pressure ratios. Therefore, the fluid can be treated as inviscid in supersonic flow.

Crocco's theorem is

$$T\nabla s = \nabla h_0 - \vec{V} \times \left(\nabla \times \vec{V}\right) + \frac{\partial \vec{V}}{\partial t} \tag{2.2}$$

For steady flow, Crocco's theorem becomes

$$T\nabla s = \nabla h_0 - \vec{V} \times \left(\nabla \times \vec{V}\right) \tag{2.3}$$

Since $\bigtriangledown h_0 = 0$ behind the shock, Eq. (2.3) becomes

$$T\nabla s = -\vec{V} \times \left(\nabla \times \vec{V}\right) \tag{2.4}$$

Since $\bigtriangledown \times \vec{V}$ is vorticity and $\bigtriangledown s$ is nonzero behind curved shocks, the flow behind curved shocks is rotational. (A flow where $\bigtriangledown \times \vec{V} \neq 0$ throughout is called a rotational flow.) Therefore rotation must be considered in solving the problems including curved shocks.

If we apply a vector product with $\vec{V}$ on both sides of Eq. (2.4), Eq. (2.4) becomes

$$T\vec{V} \bullet \bigtriangledown s = -\vec{V} \bullet \vec{V} \times \left(\nabla \times \vec{V}\right) \tag{2.5}$$

The right hand side of Eq. (2.5) is zero from the definition of the dot product and cross product of vectors. Since $\vec{V} \bullet \bigtriangledown s = \frac{Ds}{Dt}$, Eq. (2.5) becomes

$$\frac{Ds}{Dt} = 0 \tag{2.6}$$

This means that the entropy is constant along a streamline in an adiabatic, inviscid flow.

We assume that the natural gas behaves as a calorically perfect gas:

$$c_p = constant \tag{2.7}$$

$$c_v = constant \tag{2.8}$$

$$\gamma = \frac{c_p}{c_v} = constant \tag{2.9}$$

Though the jet is composed of natural gas, in order to compare our results with existing experimental results for jets of air, we took $\gamma = 1.4$ in our calculations. An exception is the design calculations of Chapter 5, in which $\gamma = 1.3$, typical for natural gas was used. We do not include combustion in our research. Thus, the system we are considering in this dissertation is calorically perfect, adiabatic, inviscid, rotational, compressible supersonic flow of an underexpanded sonic jet with axisymmetry emanating from an orifice or annular nozzle.

2.1.2. Derivation of the Differential Equations

The continuity equation may be written

$$\rho\frac{\partial u}{\partial x} + \rho\frac{\partial v}{\partial r} + u\frac{\partial \rho}{\partial x} + v\frac{\partial \rho}{\partial r} = -\frac{\rho v}{r} \tag{2.10}$$

If there are no viscous forces, Euler's equations may be written

$$u\frac{\partial u}{\partial x} + v\frac{\partial u}{\partial r} + \frac{1}{\rho}\frac{\partial p}{\partial x} = 0 \tag{2.11}$$

$$u\frac{\partial v}{\partial x} + v\frac{\partial v}{\partial r} + \frac{1}{\rho}\frac{\partial p}{\partial r} = 0 \tag{2.12}$$

For regions of flow from which shocks are excluded, the entropy is a continuous function of x and r (shock jump conditions will connect shock free zones in this work).

$$ds = \frac{\partial s}{\partial x}dx + \frac{\partial s}{\partial r}dr \tag{2.13}$$

Under the assumption of axial symmetry, the definition of a streamline is $dr/dx = v/u$. Along a streamline, the entropy is constant in the absence of viscous and combustion effects, thus,

$$ds = u\frac{\partial s}{\partial x} + v\frac{\partial s}{\partial r} = 0 \tag{2.14}$$

Since the pressure is a continuous function of entropy and density,

$$dp = \left(\frac{\partial p}{\partial s}\right)_\rho ds + \left(\frac{\partial p}{\partial \rho}\right)_s d\rho \tag{2.15}$$

For a calorically perfect gas,

$$\frac{ds}{c_v} = \frac{dp}{p} - \gamma\frac{d\rho}{\rho} \tag{2.16}$$

Therefore,

$$\left(\frac{\partial p}{\partial s}\right)_\rho = \frac{p}{c_v} \tag{2.17}$$

The definition of sound velocity applied to a perfect gas gives

$$\left(\frac{\partial p}{\partial \rho}\right)_s = a^2 = \frac{\gamma p}{\rho} \tag{2.18}$$

Thus Eq. (2.15) may be expressed as

$$dp = \frac{\rho a^2}{\gamma} d\left(\frac{s}{c_v}\right) + a^2 d\rho \tag{2.19}$$

and the partial derivatives $\partial p/\partial x$ and $\partial p/\partial r$ which appears in Eqs. (2.11) and (2.12) becomes

$$\frac{\partial p}{\partial x} = \frac{\rho a^2}{\gamma}\frac{\partial\left(s/c_v\right)}{\partial x} + a^2\frac{\partial \rho}{\partial x} \tag{2.20}$$

$$\frac{\partial p}{\partial r} = \frac{\rho a^2}{\gamma}\frac{\partial\left(s/c_v\right)}{\partial r} + a^2\frac{\partial \rho}{\partial r} \tag{2.21}$$

Substituting Eqs. (2.20) and (2.21) into Eqs. (2.11) and (2.12) respectively, Euler's equations for axisymmetric rotational flow become

$$u\frac{\partial u}{\partial x} + v\frac{\partial u}{\partial r} + \frac{a^2}{\rho}\frac{\partial \rho}{\partial x} + \frac{a^2}{\gamma}\frac{\partial (s/c_v)}{\partial x} = 0 \tag{2.22}$$

$$u\frac{\partial v}{\partial x} + v\frac{\partial v}{\partial r} + \frac{a^2}{\rho}\frac{\partial \rho}{\partial r} + \frac{a^2}{\gamma}\frac{\partial (s/c_v)}{\partial r} = 0 \tag{2.23}$$

Eq. (2.14) can be rewriten

$$u\frac{\partial (s/c_v)}{\partial x} + v\frac{\partial (s/c_v)}{\partial r} = 0 \tag{2.24}$$

Since u, v, ρ, and s are all continuous function of x and y, we may written

$$du = \frac{\partial u}{\partial x}dx + \frac{\partial u}{\partial r}dr \tag{2.25}$$

$$dv = \frac{\partial v}{\partial x}dx + \frac{\partial v}{\partial r}dr \tag{2.26}$$

$$d\rho = \frac{\partial \rho}{\partial x}dx + \frac{\partial \rho}{\partial r}dr \tag{2.27}$$

$$d(s/c_v) = \frac{\partial (s/c_v)}{\partial x}dx + \frac{\partial (s/c_v)}{\partial r}dr \tag{2.28}$$

Now we have eight unknowns, namely, $\partial u/\partial x$, $\partial u/\partial y$, $\partial v/\partial x$, $\partial v/\partial y$, $\partial \rho/\partial x$, $\partial \rho/\partial y$, $\partial u/\partial y$, $\partial s/\partial x$, and $\partial s/\partial y$, which are connected by eight independent, linear, nonhomogeneous equations, namely Eqs. (2.10), (2.22), (2.23), (2.24), (2.25), (2.26), (2.27), and (2.28). These equations may be written in matrix form

$$\begin{pmatrix} \rho & 0 & 0 & \rho & u & v & 0 & 0 \\ u & v & 0 & 0 & \frac{a^2}{\rho} & 0 & \frac{a^2}{\gamma} & 0 \\ 0 & 0 & u & v & 0 & \frac{a^2}{\rho} & 0 & \frac{a^2}{\gamma} \\ 0 & 0 & 0 & 0 & 0 & 0 & u & v \\ dx & dr & 0 & 0 & 0 & 0 & 0 & 0 \\ 0 & 0 & dx & dr & 0 & 0 & 0 & 0 \\ 0 & 0 & 0 & 0 & dx & dr & 0 & 0 \\ 0 & 0 & 0 & 0 & 0 & 0 & dx & dr \end{pmatrix} \begin{pmatrix} \frac{\partial u}{\partial x} \\ \frac{\partial u}{\partial y} \\ \frac{\partial v}{\partial x} \\ \frac{\partial v}{\partial y} \\ \frac{\partial \rho}{\partial x} \\ \frac{\partial \rho}{\partial y} \\ \frac{\partial (s/c_v)}{\partial x} \\ \frac{\partial (s/c_v)}{\partial y} \end{pmatrix} = \begin{pmatrix} \frac{\rho v}{r} \\ 0 \\ 0 \\ 0 \\ du \\ dv \\ d\rho \\ d\left(\frac{s}{c_v}\right) \end{pmatrix} \tag{2.29}$$

In general, the characteristic curves are defined as those curves on the integral surfaces comprising the solution to the eight equations on which the eight derivatives may be either indeterminate or discontinuous. The conditions for this to be so is that each of the derivatives be of the form $0/0$. We set the determinants of numerator and denominator to equal to zero and simplify the equations and express the velocity vector in terms of polar coordinates V and θ by means of the relations $u = V\cos\theta$ and $v = V\sin\theta$ and get the differential equations of the characteristics. The required algebra is somewhat complex and the details will not be presented here (see Ref. [2] for example).

The Mach angle defined as

$$\mu = \arcsin\left(\frac{1}{M}\right) \tag{2.30}$$

The Prandtl-Meyer function is defined as

$$\nu(M) = \int \frac{\sqrt{M^2 - 1}}{1 + \frac{\gamma - 1}{2} M^2} \frac{dM}{M} \tag{2.31}$$

Characteristic Line Equations:

$$\left(\frac{dr}{dx}\right)_{C_{\mp}} = \tan(\theta \mp \mu) \tag{2.32}$$

These equations define the slope of two curves, the characteristic curves, at all points in $x - r$ space.

Compatibility Equations:

$$d(\theta \pm \nu)_{C_\mp} = \pm \frac{1}{\sqrt{M^2-1} \mp \cot\theta} \frac{dr}{r} \mp \frac{\sin\mu \cos\mu}{\gamma(\gamma-1)} \frac{ds}{c_v} \tag{2.33}$$

The effects of vorticity are contained in the third term of Eq. (2.33). This term depends partly on the spatial variable x and r because the entropy is determined by the streamline rather than the Mach number. The compatibility conditions give the variation of the Mach number along the characteristic curves but require an additional equation to determine the entropy, s - thus the third characteristic equation, $Ds/Dt = 0$ (Eqs. 2.14 and 2.24).

2.1.3. Characteristics

Figure 2.1 shows the characteristics for rotational flow. Since the $C_\pm$ characteristics are inclined at the angles $\pm\mu$ to the streamline, the $C_\pm$ characteristics are physically the Mach lines of the flow. The C_+ characteristic is a left-running characteristic and the C_- characteristic is a right-running characteristic. For axisymmetric rotational flow, any streamline is another characteristic line because $s = constant$ along $\frac{dr}{dx} = \frac{v}{u}$. Since the entropy and the stagnation enthalpy are invariant along streamlines, their values at 3 are the same as at 3′ in Fig. 2.1. The stagnation enthalpy is assumed the same everywhere in the case under consideration and the entropy remains constant on each streamline, but will vary from streamline to streamline when curved shocks are present.

In a steady supersonic flow, disturbances are felt only in limited regions whereas disturbances are felt everywhere throughout the flowfield in a subsonic flow. In Fig. 2.1, the line between the two upstream characteristics (points 1 and 2) influences the point 3. Similarly the disturbances generated at point 3 influence the region between the two downstream characteristics. Thus, in steady supersonic flow no upstream propagation occurs.

2.1.4. Finite Difference Equations

For an adiabatic process of a perfect gas, the change of entropy can be related to the variation of stagnation pressure through the second law of thermodynamics.

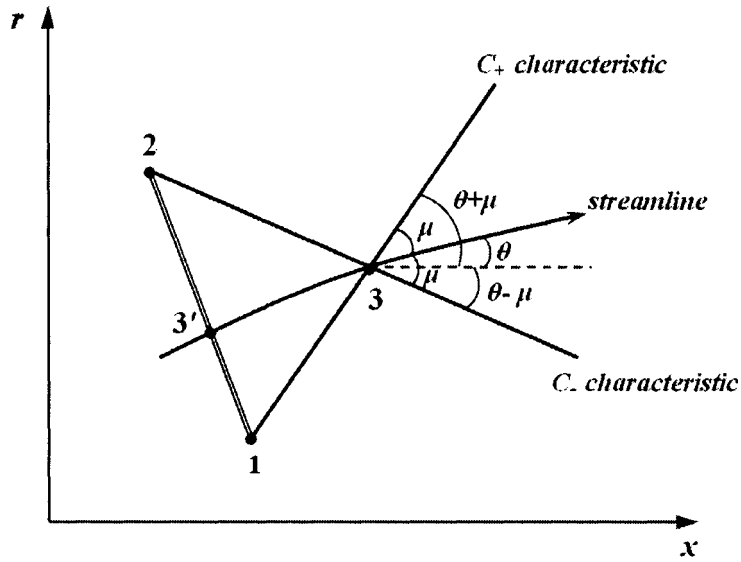

Figure 2.1. Characteristics.

$$\frac{ds}{c_v} = -(\gamma - 1)\frac{dp_0}{d\rho_0} \tag{2.34}$$

In finite difference form,

$$\frac{s_2 - s_1}{c_v} = -(\gamma - 1)\ln\left(\frac{p_{02}}{p_{01}}\right) \tag{2.35}$$

Using this Eq. (2.34) along with Eqs. (2.33) and converting to finite difference forms, the compatibility equations becomes

$$\theta_3+\nu_3 = \theta_2+\nu_2+\frac{1}{\sqrt{\left(\frac{M_2+M_3}{2}\right)^2 - 1} - \cot\left(\frac{\theta_2+\theta_3}{2}\right)}\frac{r_3 - r_2}{\left(\frac{r_2+r_3}{2}\right)} - \frac{\sin\left(\frac{\mu_2+\mu_3}{2}\right)\cos\left(\frac{\mu_2+\mu_3}{2}\right)}{\gamma}\ln\left(\frac{p_{03}}{p_{02}}\right) \tag{2.36}$$

along the C_- characteristic,

$$\theta_3 - \nu_3 = \theta_1 - \nu_1 - \frac{1}{\sqrt{\left(\frac{M_1+M_3}{2}\right)^2 - 1} + \cot\left(\frac{\theta_1+\theta_3}{2}\right)} \frac{r_3 - r_1}{\left(\frac{r_1+r_3}{2}\right)} + \frac{\sin\left(\frac{\mu_1+\mu_3}{2}\right)\cos\left(\frac{\mu_1+\mu_3}{2}\right)}{\gamma} \ln\left(\frac{p_{03}}{p_{01}}\right) \tag{2.37}$$

along the C_+ characteristic.

Note that the third characteristic equation, $s = constant$ along streamline, must be used in order to relate $p_{03'}$ to p_{01} in Fig. 2.1.

2.2. Shock Waves

Shock waves are established in a supersonic flow by nature to resolve physical requirements having to do with the propagation and reinforcement of disturbances in the flow. It is necessary that flow properties suddenly change across a shock wave. It is desirable to avoid shock waves in designing systems such as supersonic nozzles because shock waves cause a significant loss of the kinetic energy across the shock.

It is necessary to study shock waves in the expansion region of an underexpanded jet for two reasons: 1) shock waves are formed by coalescence of compression waves which are reflected at the jet boundary, and 2) a Mach disc causing transition from supersonic to subsonic flow and consequent large losses in kinetic energy can form at the axis of symmetry.

2.2.1. Shock Wave Relations

Oblique shock relations are used to determine jump conditions caused by the coalescence of characteristics of the same family. The geometry of flow through an oblique shock is given in Fig. 2.2. The velocity upstream of the shock is V_1, and is horizontal. The corresponding Mach number is M_1. The oblique shock has a wave angle, α, with respect to the upstream flow direction, V_1. Behind the shock, the flow is deflected toward the shock by the flow-deflection angle, θ. The velocity and Mach number behind the shock are V_2 and M_2, respectively. The components of V_1 and V_2 perpendicular to the shock wave are V_{n1} and V_{n2}, respectively. Therefore, we can consider the normal Mach numbers to be M_{n1} and M_{n2} and defined as

$$M_{n1} = M_1 \sin\alpha \tag{2.38}$$

$$M_{n2} = M_2 \sin(\alpha - \theta) \tag{2.39}$$

The oblique shock relations between the region 1 and 2 in Fig. 2.2 are

$$\frac{\rho_2}{\rho_1} = \frac{(\gamma+1)\,M_{n1}^2}{(\gamma-1)\,M_{n1}^2+2} \tag{2.40}$$

$$\frac{p_2}{p_1} = 1 + \frac{2\gamma}{\gamma+1}\left(M_{n1}^2 - 1\right) \tag{2.41}$$

$$\frac{T_2}{T_1} = \left(1 + \frac{2\gamma}{\gamma+1}\left(M_{n1}^2 - 1\right)\right)\frac{(\gamma-1)\,M_{n1}^2+2}{(\gamma+1)\,M_{n1}^2} \tag{2.42}$$

$$M_{n2}^2 = \frac{M_{n1}^2 + (2/(\gamma-1))}{(2\gamma/(\gamma-1))\,M_{n1}^2 - 1} \tag{2.43}$$

$$\tan\theta = 2\cot\alpha\left(\frac{M_1^2\sin^2\alpha - 1}{M_1^2(\gamma+\cos 2\alpha)+2}\right) \tag{2.44}$$

Equation (2.44) is called the θ-α-M *relation*, and specifies the flow-deflection angle, θ, as a unique function of upstream Mach number, M_1, and shock angle, α.

2.2.2. Shock Treatment in Characteristic Net

Figure 2.3 shows the formation of a shock. When the flow direction of the supersonic flow changes gradually upward following the curved wall, Mach waves are generated by the small disturbance at the wall and converge to each other because of the concave wall and also because the compression, which occurs, increases the temperature and therefore μ. Eventually an oblique shock is formed by the coalescence of the successive compressive Mach waves. As additional compressive Mach waves are added to an oblique shock, the strength of the shock increases. Since the $C_{\pm}$ characteristics are physically Mach waves,

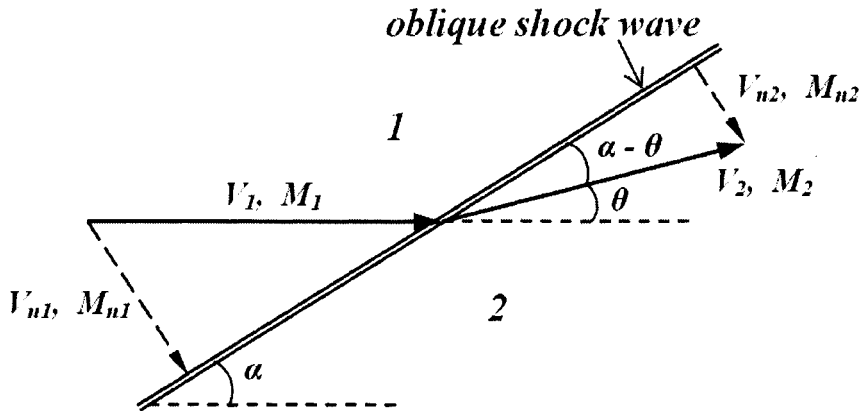

Figure 2.2. Oblique shock wave geometry.

the intersection of the $C_{\pm}$ characteristics of the same family forms an oblique shock. In the same way, the compression waves (characteristics) reflected at the jet boundary form an incident shock wave by coalescing with each other. When a characteristic encounters a shock wave, the characteristic is merged into the shock wave or passes through the shock wave depending on the family of the characteristic. It is necessary to establish a consistent method dealing with the interaction between characteristics and shock waves.

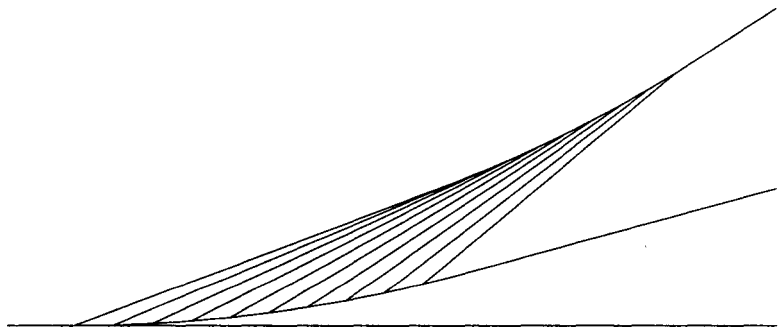

Figure 2.3. Shock wave formation caused by coalescence of the characteristics of the same family.

2.2.2.1. Intersection of Two Compression Characteristics

The treatment of the intersection of two compression waves is shown in Fig. 2.4. In the absence of a shock wave the properties at point $(i-1)$ are determined by the properties at points $(k-1)$ and $(i-2)$ and the properties at point (i) are determined by the properties at points (k) and $(i-1)$ in Fig. 2.4 (a). However, the characteristic lines $\overrightarrow{(k-1)(i-1)}$ and $\overrightarrow{(k)(i)}$ intersect at a point labeled A or B, where a shock wave is assumed to start. The flow direction heads from left to right. The points A and B represent the point slightly ahead of a the shock and the point slightly behind the shock, respectively. These two points are located at the same coordinates but have different properties because the shock is very thin and discontinuous. The shock thickness is usually on the order of a few molecular mean free paths, typically 10^{-7}m for air at standard conditions. Since the points $(k-1)$ and (k) are not aware of the existence of the intersection of characteristics (see Section 2.1.3), the information on the characteristics can be calculated using continuous flow equations until these characteristics intersect each other. The flow properties at point A, slightly ahead of the shock, are obtained from linear interpolation of the flow properties at points $(k-1)$ and $(i-1)$. Similarly, the flow properties at point B, immediately behind the shock, are obtained from linear interpolation of the flow properties at points (k) and (i). The shock wave angle at the intersection point is obtained from the information about the upstream Mach number, M_A, and the flow deflection angle across the shock wave, $\theta = \theta_B - \theta_A$, using the oblique shock relations in Section 2.2.1. The shock wave is extended from point A with the shock wave angle thus obtained and intersects the characteristic line $\overrightarrow{(i-2)(i-1)}$ in Fig. 2.4 (a). This intersection point is the new location of points $(i-1)$ and (i), shown in Fig. 2.4 (b). The flow properties of point $(i-1)$ in Fig. 2.4 (b) are determined from the linear interpolation of the flow properties at points $(i-2)$ and $(i-1)$ in Fig. 2.4 (a). The flow properties of point (i) in Fig. 2.4 (b) are determined by the shock wave angle at point A and the upstream Mach number M_{i-1} in Fig. 2.4 (b) using the oblique shock relations. It is assumed that the shock wave angle does not change unless a compression wave is added to the shock wave because the radial effect on the shock wave angle is relatively small in a cell

of dense characteristic net. Therefore, the shock wave angle at point $(i-1)$ is considered to be equal to the shock wave angle at point A.

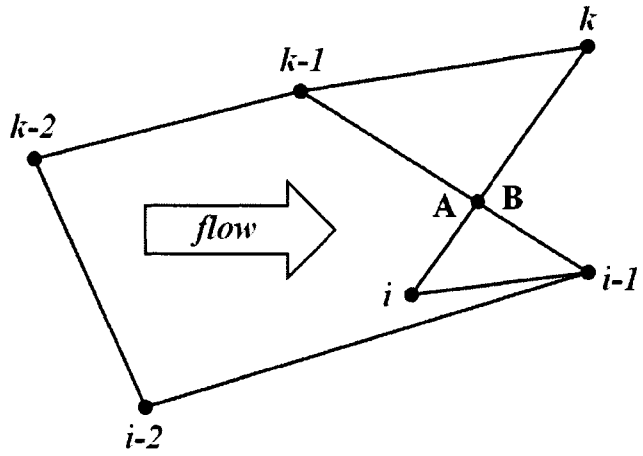

(a)

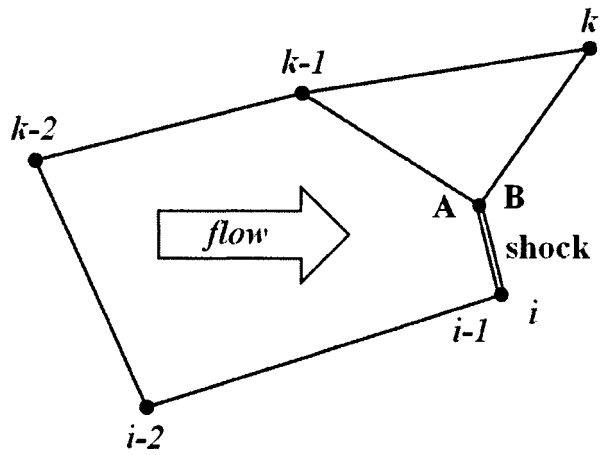

(b)

Figure 2.4. Shock wave formation by coalescence of compression waves: (a) intersection of two compression waves of the same family, (b) coalescence of two compression waves into a shock wave.

2.2.2.2. Shock Wave Extension

A shock wave is not a characteristic. Information upstream and downstream of the shock wave propagates only along characteristic lines. The flow properties at point $(i-1)'$are determined by the flow properties at point $(k-1)$ and $(i-2)$ in Fig. 2.5 (Note change in point labeling system from Fig. 2.4). However, since point $(k-1)$ is the upstream shock

point, the shock is extended from this point. As shown in Fig. 2.5, the shock wave is inclined downward more than the characteristic line $\overrightarrow{(k-1)(i-1)'}$ because the shock wave angle, α, is larger than the Mach angle, μ. The extended shock intersects characteristic $\overrightarrow{(i-2)(i-1)'}$ at point $(i-1)$, which is the upstream shock point. The properties at point $(i-1)$ are linearly interpolated from the flow properties at points $(i-2)$ and $(i-1)'$. The flow properties at point (i) are obtained from the flow properties at point $(i-1)$ using the oblique shock relations.

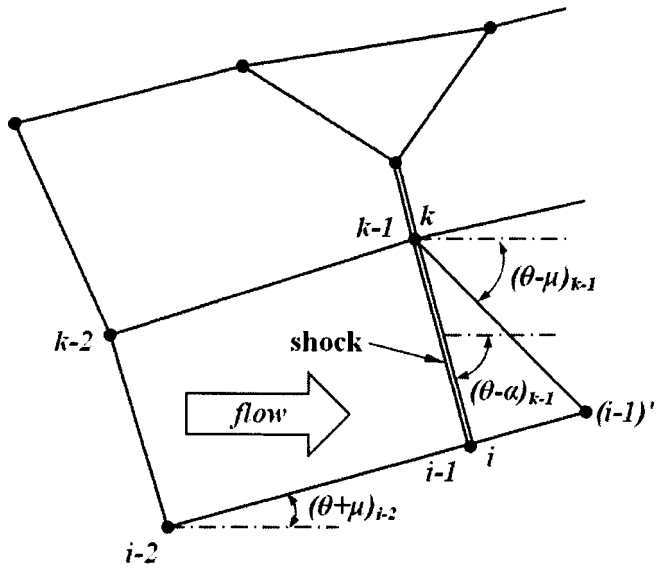

Figure 2.5. Shock wave extension.

2.2.2.3. Intersection of Compression Characteristic with Shock Wave

When a compression wave intersects a shock wave, the shock wave strength increases. As shown in Fig. 2.6 (a), the flow properties of point (i) are established from a characteristic calculation with the flow properties at points (k) and $(i-1)$. Compression characteristic $\overrightarrow{(k)(i)}$ intersects shock wave $\overline{(k-1)(i-1)}$ at point B. The upstream shock conditions at point A are obtained by linear interpolation of the flow properties at points $(k-2)$ and $(i-2)$. The flow properties at point B are linearly interpolated from the flow properties at points (k) and (i) in Fig. 2.6 (a). The shock wave angle at point A is calculate.d from the flow deflection angle across the shock and the upstream Mach number at point A. Since the shock wave strength increases by coalescence of compression waves, the shock wave angle

increases too. The strengthened shock is extended from point A and intersects characteristic $\overrightarrow{(i-3)(i-2)}$ in Fig. 2.6 (b). This intersection point is the new location of points $(i-2)$ and $(i-1)$. The flow properties at point $(i-2)$ in Fig. 2.6 (b) are determined by the interpolation of the flow properties at points $(i-3)$ and $(i-2)$ in Fig. 2.6 (a). The flow properties at point $(i-1)$ in Fig. 2.6 (b) are calculated from the shock wave angle and the flow properties at point $(i-2)$ in Fig. 2.6 (b) using the oblique shock relations in Section 2.2.1. The point (i) is only a temporary, hypothetical downstream point.

2.2.3. Shock Wave Reflection

Figure 2.7 shows two reflection configurations. In both cases the upstream Mach number is fixed and uniform. When the incident shock angle, α_i, is sufficiently small, the incident shock wave can be reflected at the wall and the streamline deflection caused by the incident shock wave can be cancelled by the reflected shock wave, as shown in Fig. 2.7 (a) so the flow remains parallel to the wall. This phenomenon is called a regular reflection (RR). As the incident shock angle, α_i, is increased beyond a critical value, the incident shock wave cannot be reflected at the wall. Instead a normal, or nearly normal, third shock appears near the wall, joining the incident shock and the reflected shock in a triple point off the wall, as shown in Fig. 2.7 (b). Due to the difference in entropy on streamlines above and below the triple point, the streamline which extends downstream from the triple point is a slipline. Above the slipline the flow is uniform in properties and direction while below the slipline the entropy continuously increases with a consequent decrease in velocity. This phenomenon is called a Mach reflection (MR). In the case of MR, the streamline deflection cannot be cancelled completely by the reflected shock wave as the case of RR but the streamlines behind the triple point are directed slightly towards the wall.

The flow conditions of regions I, II, and III in Fig. 2.7 (a) are uniform because the shock waves are straight. In Fig. 2.7 (b), the flow conditions of regions I, II and III are uniform but the flow conditions of region IV are not uniform because the Mach stem is curved and the flow direction just behind the Mach stem changes continuously. The flow deflection angle of the MR should be considered locally in the vicinity of the triple point.

The smallest value of α_i at which the configuration of Fig. 2.7 (b) is theoretically

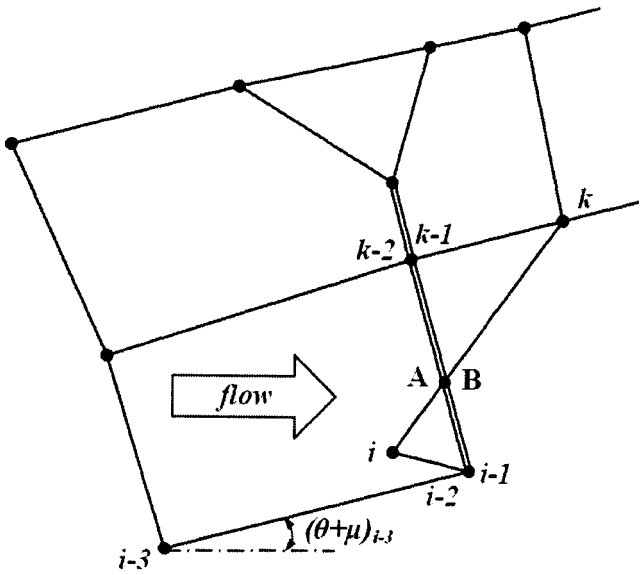

(a)

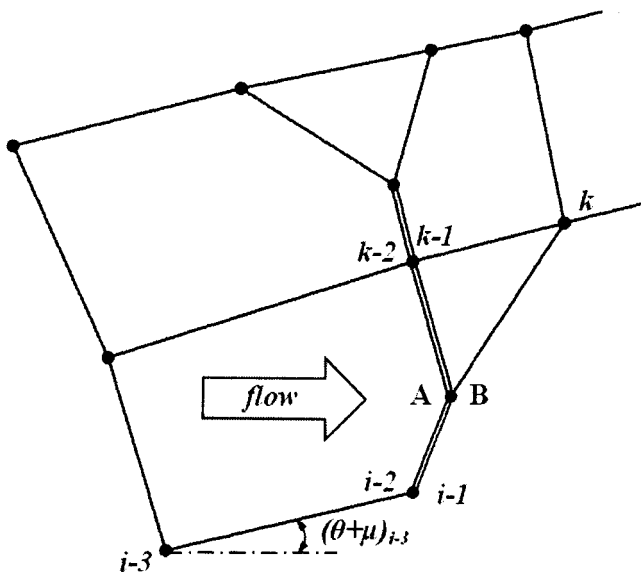

(b)

Figure 2.6. Addition of a compression wave to a shock wave; (a) intersection of a compression wave and a shock wave, (b) coalescence of a compression wave into a shock wave.

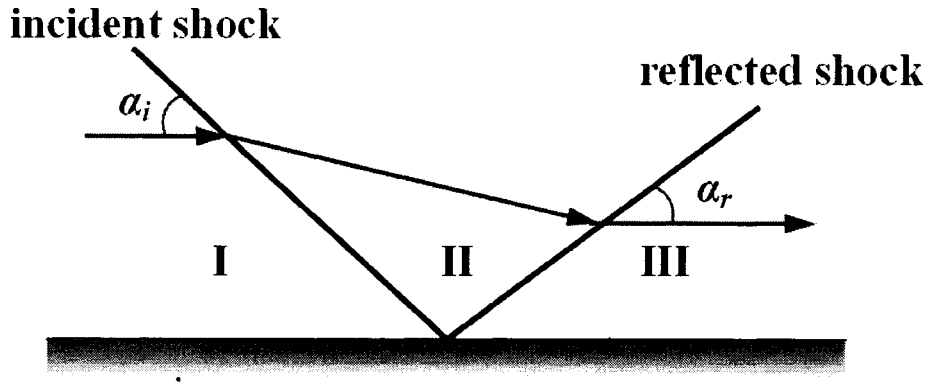

(a) regular reflection

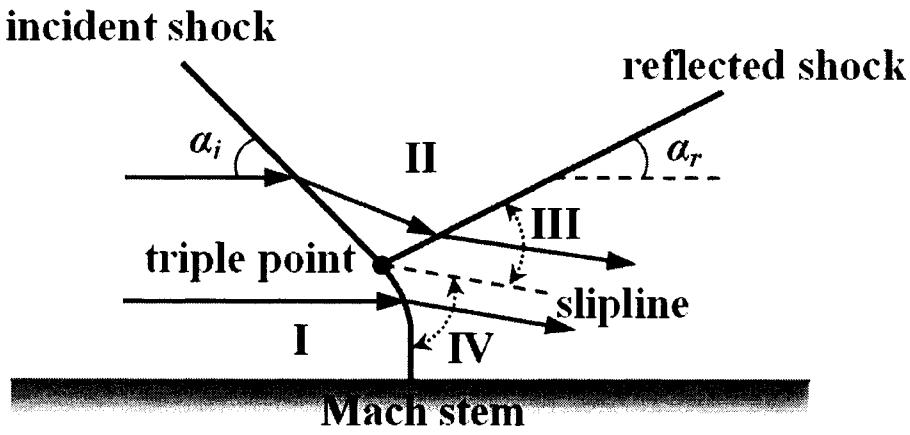

(b) Mach reflection

Figure 2.7. Schematic illustration of the wave configuration.

possible is the von Neumann criterion angle, α_N, and the largest value of α_i at which the configuration of Fig. 2.7 (a) is theoretically possible is the detachment criterion angle, α_D. For the dual solution domain, $\alpha_N \leq \alpha_i \leq \alpha_D$, both RR and MR are possible.

To understand better these criteria and the shock wave reflection phenomenon, it is instructive to map the configurations of Fig. 2.7 into the pressure-flow angle plane. The locus of all possible static pressures behind an incident oblique shock wave as a function of deflection angle for given upstream conditions of region I is given by the incident shock polar in Fig. 2.8 (a). Thus the regions I and II in Fig. 2.7 (a) map into the points I and II in Fig. 2.8 (a), respectively. The flow deflection angle in Fig. 2.7 is considered positive in

a clockwise direction. From the point II of the incident shock polar, a second shock polar may be drawn to represent all possible static pressures achievable via the reflected shock as a function of deflection angle for given upstream conditions of region II. This is called the reflected shock polar. Since the flow direction in region III in Fig. 2.7 (a) is horizontal, the region III maps into the point where the reflected shock polar intersects the pressure axis. There exist two such points in shock polars but the strong solution is not favored and is seldom of interest. Consequently, the region III in Fig. 2.7 (a) maps into the point III in Fig. 2.8 (a).

Figure 2.8 (b) shows the von Neumann criterion, $\alpha_i = \alpha_N$. This is the smallest incident shock wave angle where both RR and MR are theoretically possible. The incident shock polar intersects the reflected shock polar at the normal shock point of the incident shock polar. In this case there is no curved shock in Fig. 2.7 and region IV is a uniform flow region.

Figure 2.8 (c) shows the dual solution domain, $\alpha_N < \alpha_i < \alpha_D$. The point where the incident shock polar intersects the reflected shock polar represents a possible MR solution. The point where the incident shock polar intersects the pressure axis represents a possible RR solution.

Figure 2.8 (d) shows the detachment criterion, $\alpha_i = \alpha_D$. This is the largest incident shock wave angle where both RR and MR are theoretically possible. If we increase α_i further, the reflected shock polar does not intersect the pressure axis. As a result, a regular reflection becomes impossible for $\alpha_i > \alpha_D$.

The regions I and II in Fig. 2.7 (b) map into the points I and II in Fig. 2.8 (e), respectively. Since the streamlines in regions III and IV are in the same direction near the triple point, the downstream shock conditions at the triple point are at the point where the incident shock and reflected shock polars intersect in Fig. 2.8 (e). The region III in Fig. 2.7 (b) maps into the point III on the reflected shock polar in Fig. 2.8 (e). The region IV near the triple point in Fig. 2.7 (b) maps into the point IV on the incident shock polar in Fig. 2.8 (e).

For invisicd flow the incident shock angle, α_i, depends on the parameters M_I and γ by shock wave relations (see Section 2.2.1) and can be expressed as

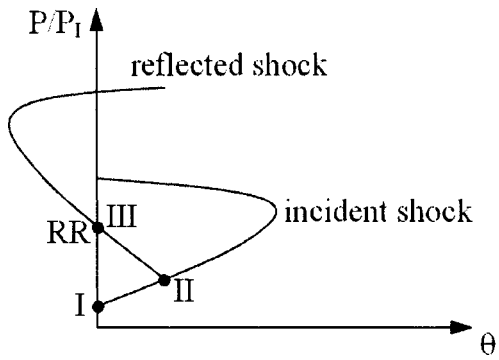

(a) a regular reflection, $\alpha_i < \alpha_N$

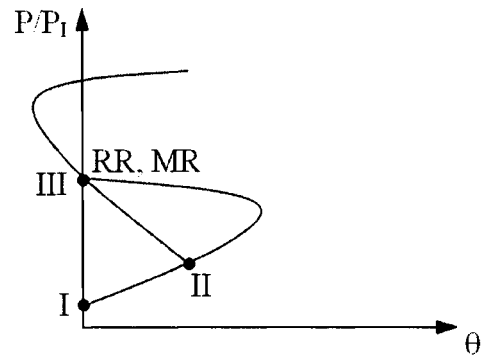

(b) the von Neumann criterion, $\alpha_i = \alpha_N$

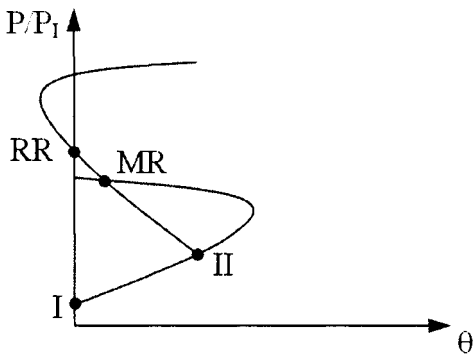

(c) regular and Mach reflections, $\alpha_N < \alpha_i < \alpha_D$

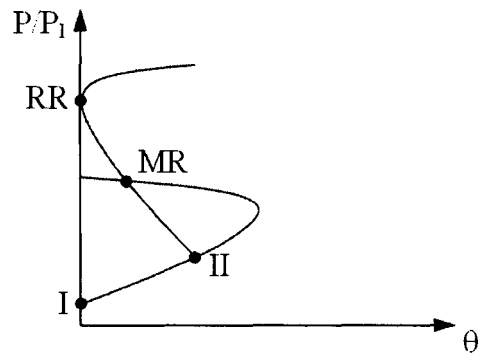

(d) the detachment criterion, $\alpha_i = \alpha_D$

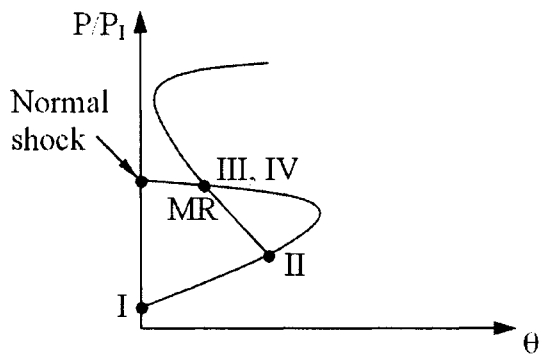

(e) a Mach reflection, $\alpha_i > \alpha_D$

Figure 2.8. Shock polars in the pressure-flow angle plane; (a) $\alpha_i < \alpha_N$, (b) $\alpha_i = \alpha_N$, (c) $\alpha_N < \alpha_i < \alpha_D$, (d) $\alpha_i = \alpha_D$, and (e) $\alpha_i > \alpha_D$.

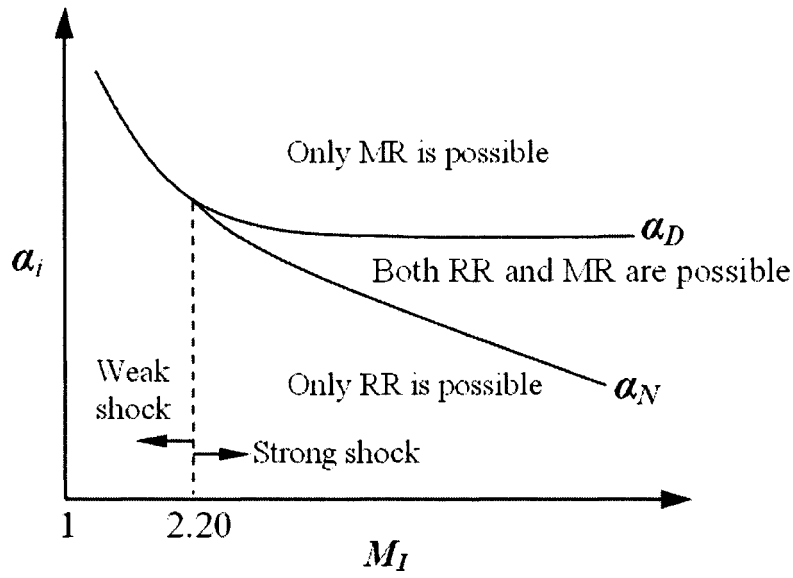

Figure 2.9. The (M_I, α_i)-plane for $\gamma = 1.4$; α_D and α_N are the transition lines corresponding to the detachment criterion and the von Neumann criterion, respectively (from Ref. [25]).

$$\alpha_i = \alpha_i(M_I, \gamma) \tag{2.45}$$

For fixed $\gamma = 1.4$, Figure 2.9 shows the shock angle as a function of the upstream Mach number M_I. The transition line of the von Neumann criterion intersects the transition line of the detachment criterion at the point $M_I = 2.20$. For the range of $M_I > 2.20$, the dual solution domain for RR and MR exists in the (M_I, α_i)-plane. While the detachment criterion exists for all values of $M_I > 1$,the von Neumann criterion does not exist in the range of $M_I \leq 2.20$ for $\gamma = 1.4$. Traditionally, the point $M_I = 2.20$ has been used to distinguish between weak and strong incident shock waves. (See Ref. [24] and [25] for details.)

Shock reflection hysteresis is illustrated schematically in the (α_i,L_M)-plane in Fig. 2.10. The L_M is the Mach stem height. If the incident shock angle, α_i, is increased slowly from a certain angle less than the von Neumann criterion angle, α_N, while the upstream Mach number is kept constant, the RR is maintained until $\alpha_i = \alpha_D$,where a sudden transition from RR to MR occurs. If α_i is decreased slowly from a certain angle larger than the detachment criterion angle, α_D, with a constant upstream Mach number, the MR is maintained while the Mach stem height decreases continuously until it becomes zero at $\alpha_i = \alpha_N$, where the

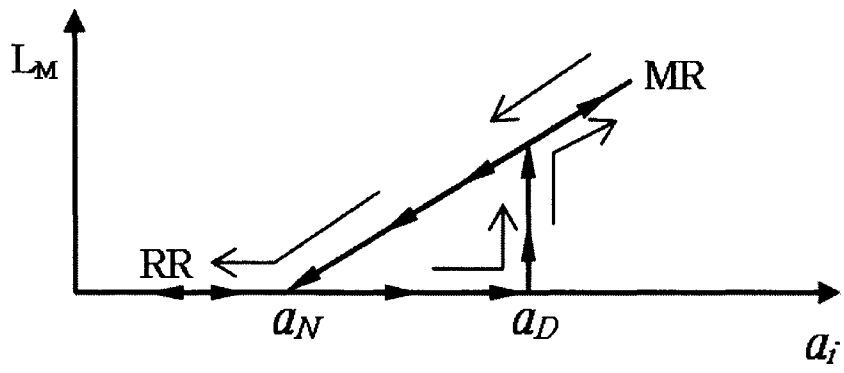

Figure 2.10. Schematic illustration on the possible hysteresis in the RR↔MR transition in the (α_i,L_M)-plane: L_M is the Mach stem height (from Ref. [25]).

MR with a zero Mach stem height is identical with the RR and ultimately a transition from MR to RR occurs. This phenomenon is called a hysteresis in shock wave reflections, first hypothesized by Hornung et. al [23]. Chpoun et. al [25] confirmed the existence of a hysteresis in the RR ↔ MR transition experimentally and showed that the MR→ RR transition occurs at the von Neumann criterion, $\alpha_i = \alpha_N$, but the RR→MR transition can occur anywhere inside the dual solution domain, $\alpha_N \leq \alpha_i \leq \alpha_D$.

2.2.4. Shock Wave in Numerical Analysis

The shock thickness is on the scale of a few mean free paths (10^{-7}m). Therefore, we ignore the structure of the very thin transition layer in a strong shock and approximate a shock wave as a discontinuity. This discontinuous feature of a shock wave is hard to maintain in CFD calculations because of the restriction on the grid size. It is necessary to refine a mesh near a shock wave to obtain a satisfactory model of the discontinuity. But the location of a shock is unknown initially, so a long time is required to process the iterations and calculate several times for a refined mesh. In contrast, for the MOC it is straightforward and fast to treat a shock wave because the MOC predicts the location and strength of shock

waves and the oblique shock relations are used to model exactly the discontinuity occurring at a shock wave.

The interaction of an oblique shock and expansion waves is illustrated in Fig. 2.11. The result in Fig. 2.11 (a) was calculated using the oblique shock relations and the method of characteristics and the result in Fig. 2.11 (b) was calculated using FLUENT, a widely used commercial CFD code. The upper surface is angled downward and the flow streamlines are deflected parallel to the upper surface. In order to turn the flow, an oblique shock is formed at the upper corner A. The lower surface is angled downward and the flow streamlines are turned downward by expansion waves emanating from the lower corner B. When a left-running oblique shock crosses a right-running expansion fan, the oblique shock is steepened slightly and the inclination of the expansion waves is decreased a little. This tendency is shown distinctively in Fig. 2.11 (a). On the other hand, in 2.11 (b) the overall tendency is observed but the oblique shock is smeared and the expansion waves emanate from a finite region near the lower corner instead of the corner point B.

The comparison of shock reflections between the oblique shock calculation and CFD is illustrated in Fig. 2.12. Shock waves are reflected regularly at similar locations initially (points B and C). The regular reflection occurs farther upstream in the CFD prediction than in the oblique shock calculation and the difference is shown clearly at point F. In Fig. 2.12 (a), the shock cannot be reflected regularly at point F because the incident shock angle is beyond the weak shock solution domain for a given upstream Mach number while in Fig. 2.12 (b) the shock is reflected at point F. The discrepancies described above may result from the effects of turbulence, heat conduction and/or viscosity within the boundary layer and near shock waves.

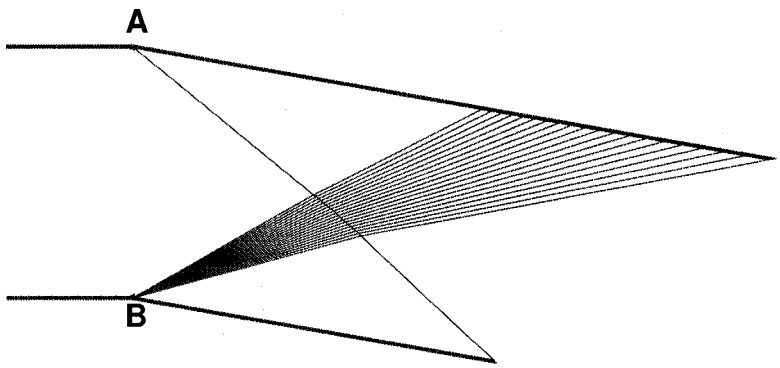

(a) MOC

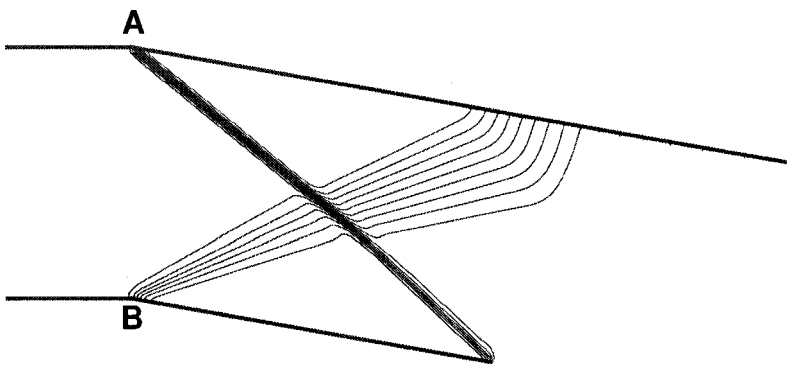

(b) CFD

Figure 2.11. Interaction of an oblique shock and expansion waves.

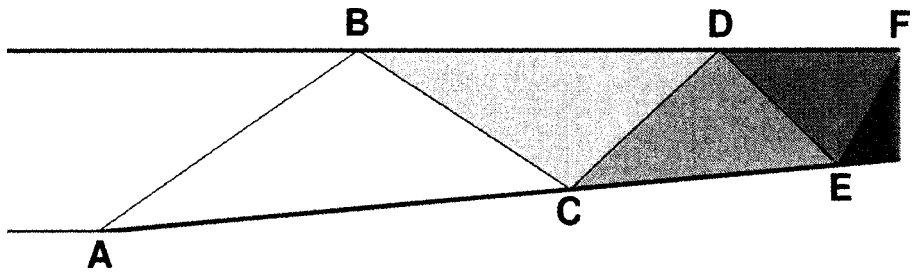

(a) oblique shock relations

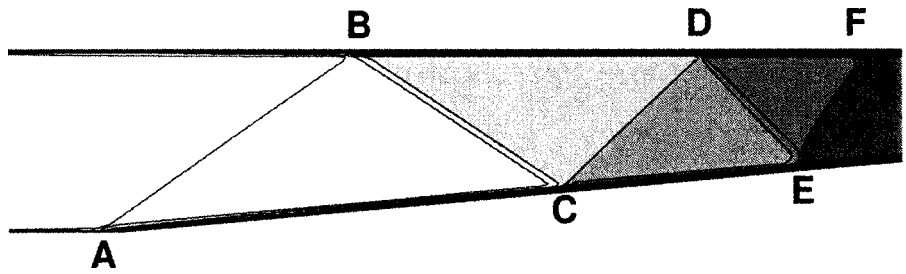

(b) CFD

Figure 2.12. Shock reflections.

Chapter 3

Axisymmetric Underexpanded Jet Analysis

3.1. Axisymmetric Underexpanded Jet Flow

When the pressure at a nozzle exit is higher than the ambient pressure, and hence the flow is capable of additional expansion after leaving the nozzle, the nozzle is said to be underexpanded. If the Mach number at the nozzle exit is unity, the jet is called a sonic jet. We are interested in the axisymmetric jet behind an underexpanded sonic nozzle.

A schematic of the underexpanded jet is shown in Fig. 3.1. An expansion fan (expansion waves) emanates from the nozzle lip because of the pressure difference between the nozzle exit and the surrounding ambient gas. The flow expands into the low pressure ambient gas through the expansion waves. The expansion waves extend to the free jet boundary and are reflected as compression waves. These compression waves coalesce to form an incident shock wave. The incident shock is a curved shock and the flow behind the incident shock is still supersonic but has a lower Mach number than the core flow of the jet. As compression waves merge into the incident shock, the incident shock strength increases and the incident shock wave angle also increases gradually to the axis of symmetry in the absence of a Mach disc. However, the incident shock cannot be reflected regularly at the axis because the incident shock angle is larger than the detachment criterion angle an obliqueat the axis (see Fig. 2.8 and the related discussion). As a result, a Mach disc occurs to adjust the flow disturbance. The reflected shock is formed at the intersection point of the incident shock and the Mach disc. (actually a line, of course, since we are looking at a single plane.) This intersection point is called the triple point because three shocks meet at this point. The Mach disc is a

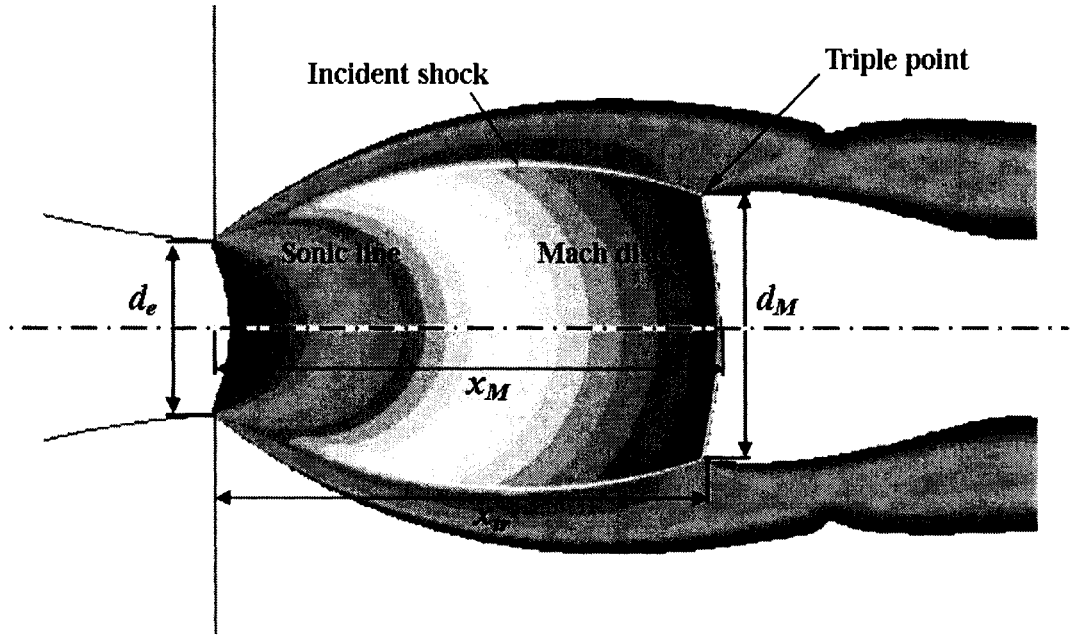

Figure 3.1. Schematic of axisymmetric underexpanded jet configuration.

curved shock and perpendicular to the flow at the axis of symmetry. The flow behind the Mach disc is subsonic, at least near the axis.

The distance of the Mach disc from the nozzle exit plane is denoted by x_M and the distance of the triple point from the nozzle exit plane is denoted by x_{tr}. These distances are nondimensionalized in terms of the nozzle exit diameter, d_e. Since the Mach disc is curved, x_M is different from x_{tr} as shown in Fig. 3.1. In previous research, the Mach disc is frequently assumed to be a straight shock and x_M is considered to coincide with x_{tr} (see Ref. [15, 20]). But in this dissertation x_{tr} is distinguished from x_M and the objective is to find the location of x_{tr}, not x_M.

3.2. Numerical Details

3.2.1. MOC Model

The accuracy of the method of characteristics (MOC) depends on the number of characteristic lines used. Actually, the number of characteristics (waves) is infinite in nature but we assume a finite number of characteristic lines in computation of a supersonic jet because

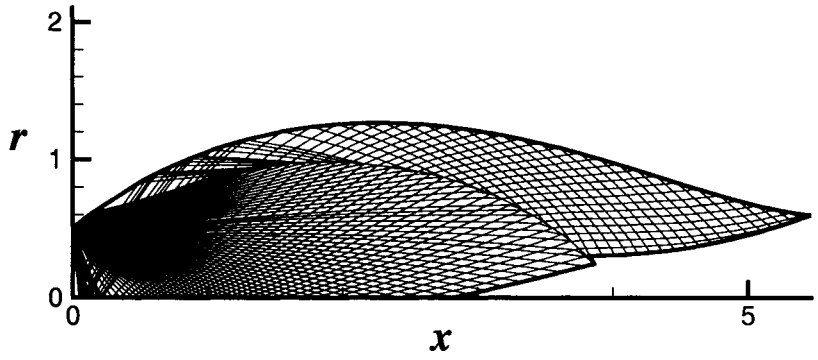

Figure 3.2. Characteristic Net; $M_e = 1$, $p_e/p_\infty = 10$, $p_e = 1$ MPa, $d_e = 1$ unit, NC=80, PC =10.

of limitations in computer capability. We define two numbers that determine the number of characteristic lines in axisymmetric calculation. First, the number of characteristic lines emanating from a nozzle lip which will be denoted by NC and second, the number of the characteristic lines starting from the initial lip characteristic, which will be denoted by PC. In contrast, two dimensional MOC needs only NC because the compatibility equations do not depend on spatial location. In this research, NC varies from 80 to 90 and PC varies from 10 to 15. The nozzle-exit-to-ambient static pressure ratio varies from 2 to 50 because the injection pressure ratios of natural gas engines are in this range. Each computation time is less than 10 seconds using double precision on a 2.80 GHz Pentium 4 processor computer. The results are plotted using Tecplot 9.0 and Kaleida Graph 9.5. A representative result for the characteristic net is shown in Fig. 3.2.

3.2.2. CFD Model

The mesh was designed for dimensional geometry using cylindrical coordinates because of the axisymmetric feature of the jet flow, as shown in Fig. 3.3. The computation domain was designed to be large enough for the jet flow not to be affected by back flow at the computational boundary. The dimensions of the computational domain are 10 units in radial direction and 20 units in axial direction with one unit being the diameter of the nozzle exit. The mesh was created with 21100 cells originally and refined several times up to 45600 cells using grid adaptation by examining the region and gradient of the flow variables

after the completion of each computation (Fig. 3.3 (b)). As can be seen in Fig. 3.3 (a), the nozzle is a convergent type so that the flow at the nozzle exit is sonic. The coupled implicit solver with the Sparlart-Allmaras turbulence model (one-equation model) and second order upwind scheme for the discretization of governing equations was used. CFD simulations were performed for three injection pressures. At the nozzle inlet, these stagnation pressures were given as boundary conditions with the values of 1.89 MPa, 3.79 MPa, and 5.68 MPa, so that the static pressure at the nozzle exit becomes 1 MPa, 2 MPa, and 3MPa, respectively. The ambient static pressure was set to 0.1 MPa. Therefore, the nozzle-exit-to-ambient static pressure ratios are 10, 20, and 30 in each case. The specific heat ratio of the injecting gas, γ, is 1.4.

In Fig. 3.3 (b), the adapted grids are concentrated near the shock waves (the Mach disc and incident shock), nozzle lip, and free jet boundary because the gradients of the flow properties are large in these regions and need to be reduced by grid adaptation. Especially the nozzle lip from which an expansion fan emanates behaves as a singular point (circumference) and it is hard to simulate an expansion fan correctly with quadratic grids because the expansion fan is directed diagonally and originates from a point (nozzle lip).

3.3. Results

3.3.1. Comparison of MOC and CFD in Jet Analysis

The MOC results are compared with CFD results for the static pressure ratio of 10. Thus, as discussed above, the static pressure at the nozzle exit is 1 MPa and the ambient pressure is 0.1 MPa in this case. The main difference is that the Mach disc predicted in CFD does not appear in MOC. The method of characteristics does not predict the existence of a Mach disc until the incident shock encounters the axis of symmetry because the MOC is a marching-type scheme and hence, downstream information does not propagate upstream. It is necessary for MOC results to introduce a criterion which defines the location of a Mach disc on an incident shock and this will be discussed later in this chapter. In this connection earlier works of Abbetts [12] used the downstream condition to terminate the

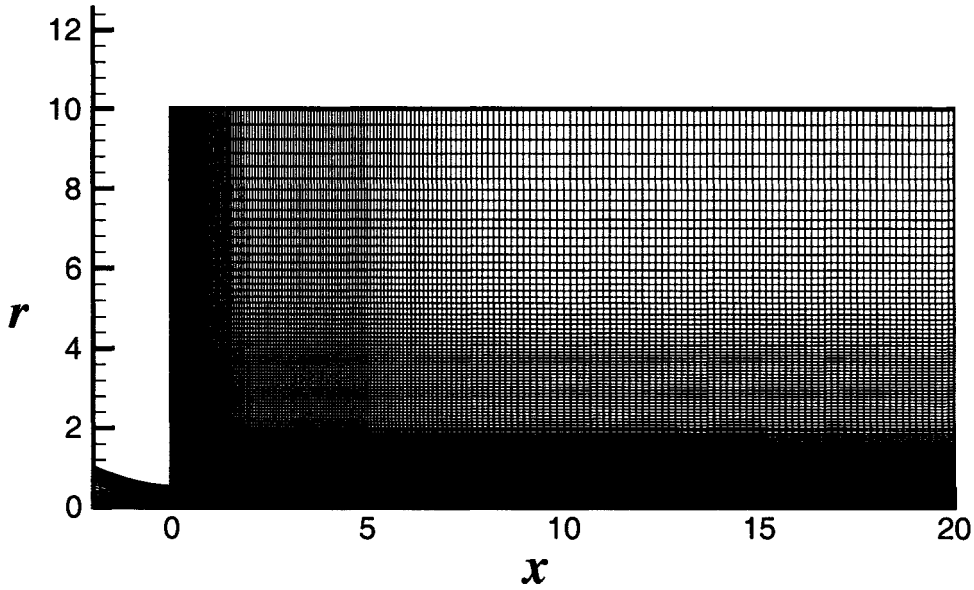

(a) Overall view of the mesh.

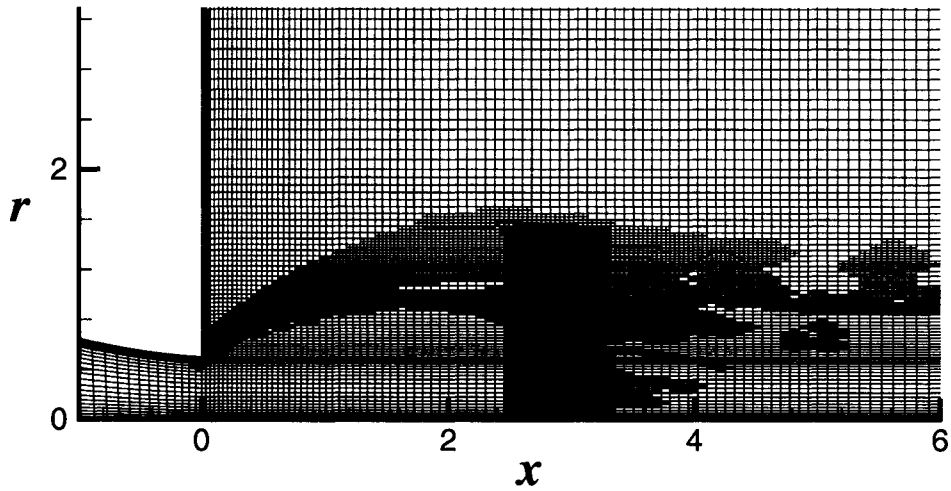

(b) Closer look at the grid near the nozzle exit.

Figure 3.3. CFD mesh; $d_e = 1$ unit.

MOC calculations. Therefore, it is meaningful to compare the results only in the regions before a Mach disc.

The contours of the flow properties are compared between MOC and CFD in Figures 3.4 - 3.8; Mach number, stagnation pressure, static pressure, static temperature, and streamlines. The contours of each property are plotted with the same scale in both MOC and CFD. Figure 3.4 shows the Mach number contours for CFD and MOC. Mach number increases continuously in the jet core flow, but decreases immediately and discontinuously after the incident shock and Mach disc. The Mach number contour for the MOC shows very good agreement with the CFD result before the Mach disc. The jet core flow of MOC result is not interrupted by a Mach disc and accelerates continuously. This may not be real but shows the jet flow behavior and the development of an incident shock wave in the absence of a Mach disc.

The stagnation pressure contours for CFD and MOC are plotted in Fig. 3.6. For an inviscid, adiabatic flow, the stagnation pressure does not decrease except across shock waves. Thus, the stagnation pressure must not decrease in the core flow of the jet before the Mach disc. Since the strength of the incident shock wave is increasing downstream, the stagnation pressure loss across the incident shock is also increasing downstream and, therefore, the flow along each streamline has a different stagnation pressure and also a different entropy. In the MOC contour, the stagnation pressure is constant in the whole region of the jet core and decreases suddenly only across the incident shock and stays constant following streamlines after the incident shock. However, in the CFD contour, there is a nonphysical decrease of the stagnation pressure inside the core flow of the jet.

The static pressure contours are plotted in Fig. 3.6. Although the injection static pressure is 1 MPa, the scale of the contours needs to be adjusted to the range of 0.005 MPa to 0.1 MPa to show the variation of the static pressure of the flow. The ninety percent drop of the static pressure occurs through the initial expansion waves. The static pressure contours also show very good agreement between CFD and MOC in the region ahead of Mach disc. The static temperature contours are depicted in Fig. 3.7 and show a good agreement with each other.

The streamlines are drawn in Fig. 3.8. The streamline direction varies radially at the

nozzle exit; the flow is deflected upward isentropically through an expansion fan near the nozzle lip but becomes parallel to the axis as it approaches the axis. The streamline of the core flow deflects downward discontinuously as it traverses the incident shock. As a flow goes downstream, the flow deflection angle across the shock increases because the incident shock is strengthened gradually.

The Mach number distribution along a jet axis is shown in Fig. 3.9 (a). As mentioned earlier, there is a sudden decrease of Mach number in CFD results because of a Mach disc while this sudden drop of Mach number does not appear in MOC results. The CFD calculations were performed for inviscid model and one-equation turbulence model, separately. In the CFD results, the Mach disc occurs slightly earlier in the inviscid model than in the one-equation model. Turbulence appears to weaken the incident shock strength by energy dissipation and interference with wave propagation and reflection at the jet boundary and, therefore, delays the development of Mach disc. However, local Mach number profiles upstream of the Mach disc coincide with each other in all three cases.

The static pressure ratio distribution along a jet axis is shown in Fig. 3.9 (b). As for the Mach disc profile, the pressure ratio distributions agree with each other before the Mach disc and the pressure recovery caused by Mach disc occurs earlier in inviscid model than in one-equation model. Overall, then, the viscosity and turbulence do not affect the core flow of a jet significantly but influence the location of a Mach disc to a small extent.

3.3.2. Flow Analysis in MOC Results

MOC computations were performed for five injection pressure ratios (the nozzle exit pressure to the ambient pressure; 10, 20, 30, 40, and 50) with constant Mach number of $M_e = 1.0$ at the nozzle exit. The local pressure ratios, Mach numbers and axial static pressures along the jet axis of symmetry are compared for various injection pressure ratios in Fig. 3.10. The static pressure at the axis, p_{axis}, is nondimensionalized by the static pressure at the nozzle exit, p_e. The static pressure ratio and Mach number profiles, respectively, coincide perfectly with each other for five injection pressure ratios, as shown in Fig. 3.10. If p_e is increased, the stagnation pressure, p_0, is increased and the static pressure at a certain location on the axis, p_{axis},is also increased, but the pressure ratio, p_0/p_e, remains constant

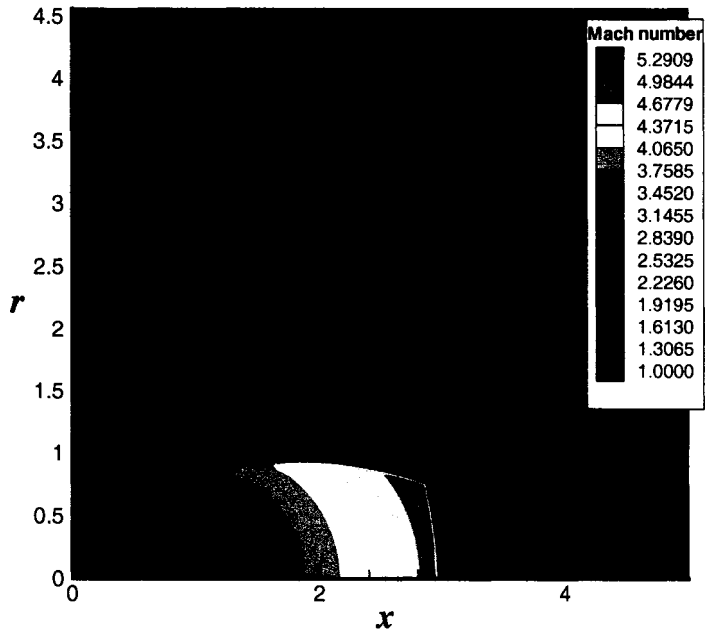

(a) CFD.

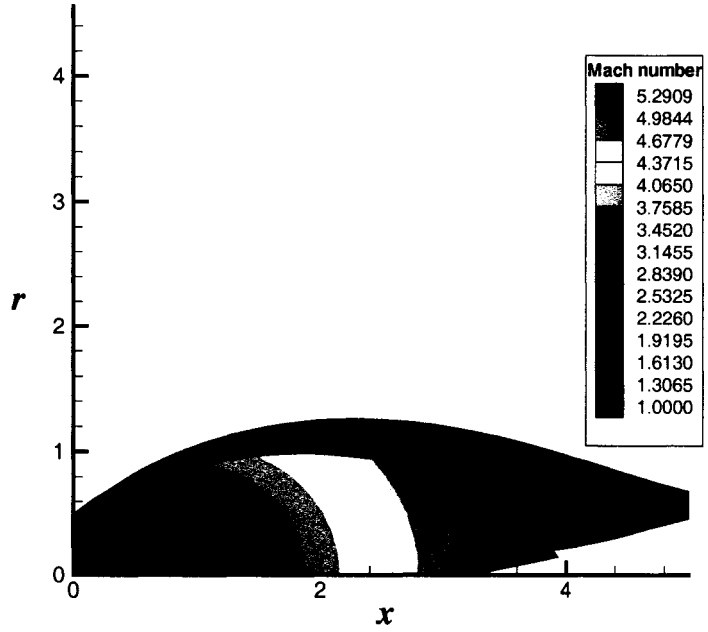

(b) MOC; NC = 89, PC = 11.

Figure 3.4. Mach number contours; $M_e = 1$, $p_e/p_\infty = 10$, $p_e = 1$ MPa.

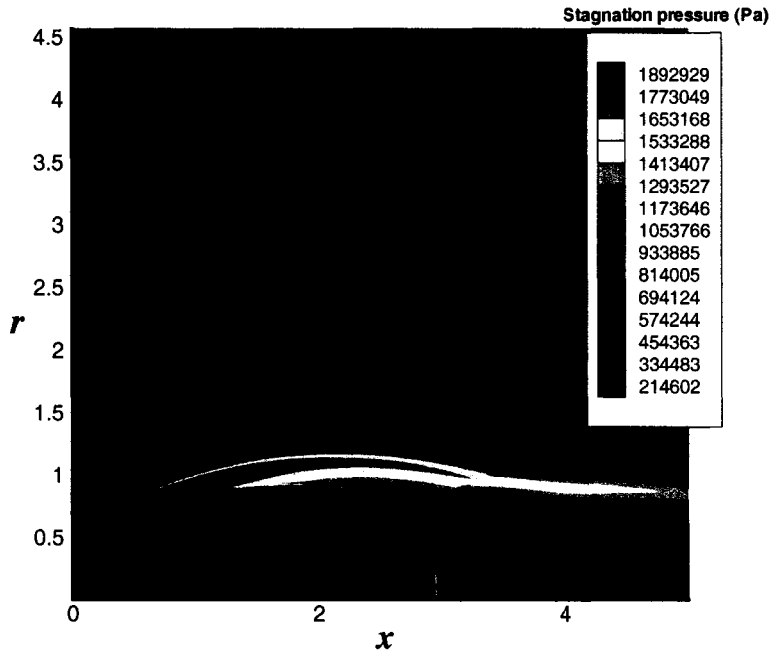

(a) CFD.

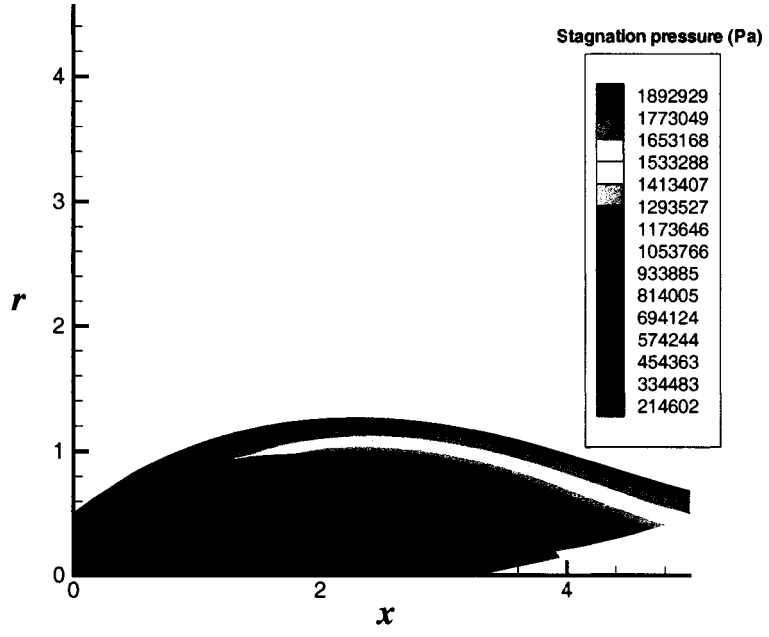

(b) MOC; NC = 89, PC = 11.

Figure 3.5. Stagnation pressure contours; $M_e = 1$, $p_e/p_\infty = 10$, $p_e = 1$ MPa.

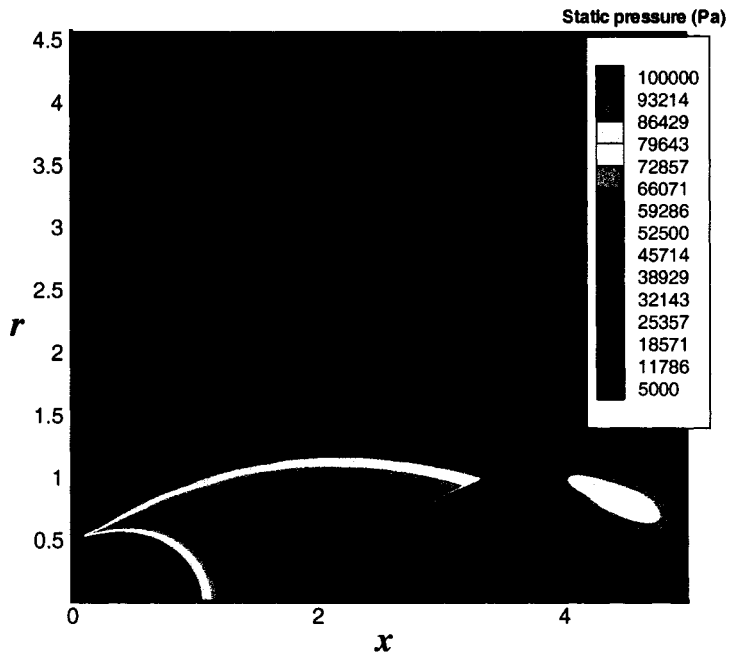

(a) CFD.

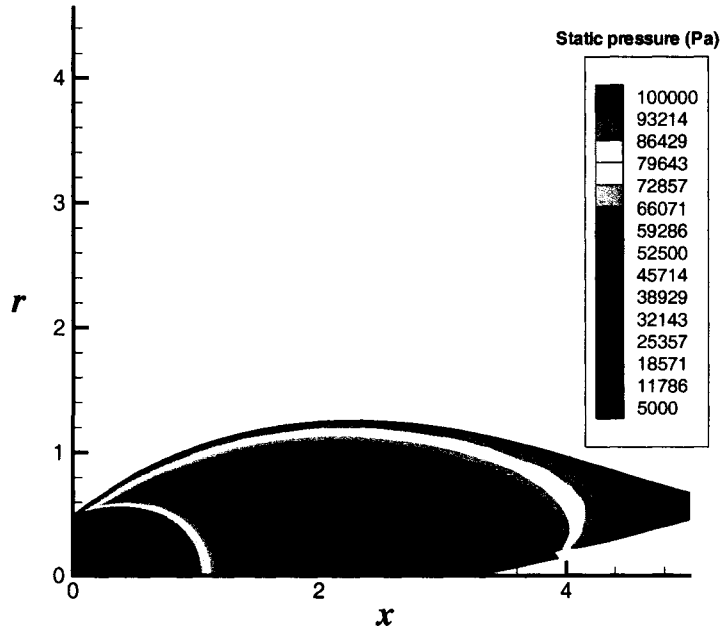

(b) MOC; NC = 89, PC = 11.

Figure 3.6. Static pressure contours; $M_e = 1$, $p_e/p_\infty = 10$, $p_e = 1$ MPa.

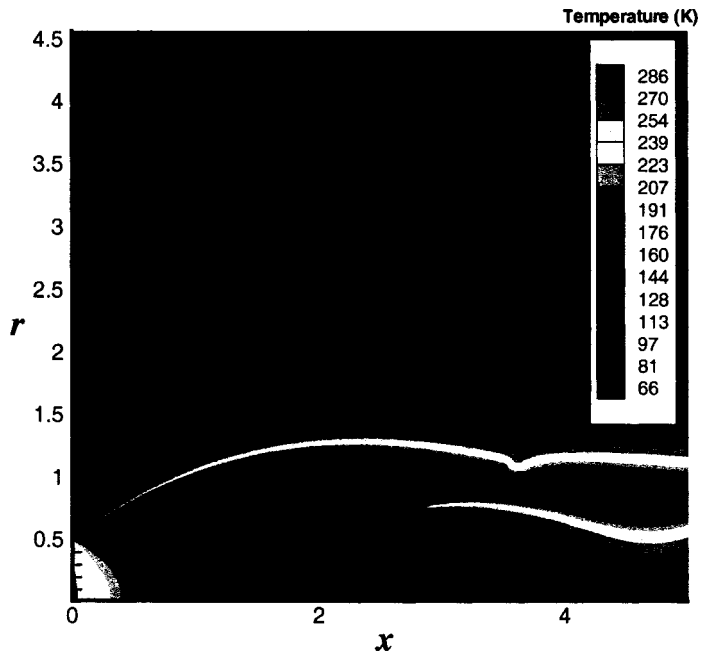

(a) CFD.

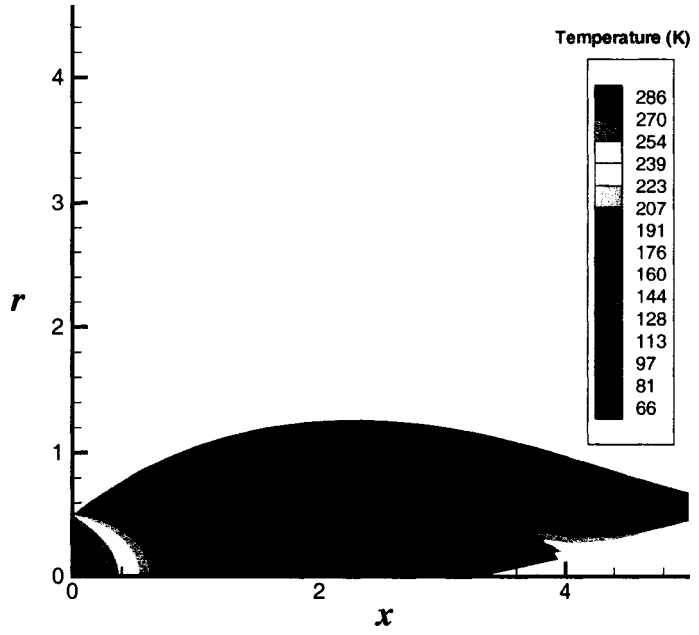

(b) MOC; NC = 89, PC = 11.

Figure 3.7. Static temperature contours; $M_e = 1$, $p_e/p_\infty = 10$, $p_e = 1$ MPa.

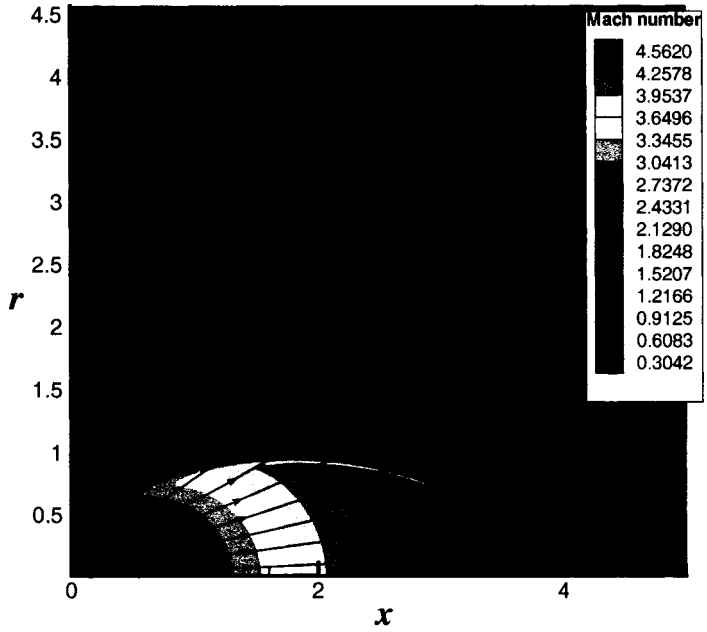

(a) CFD

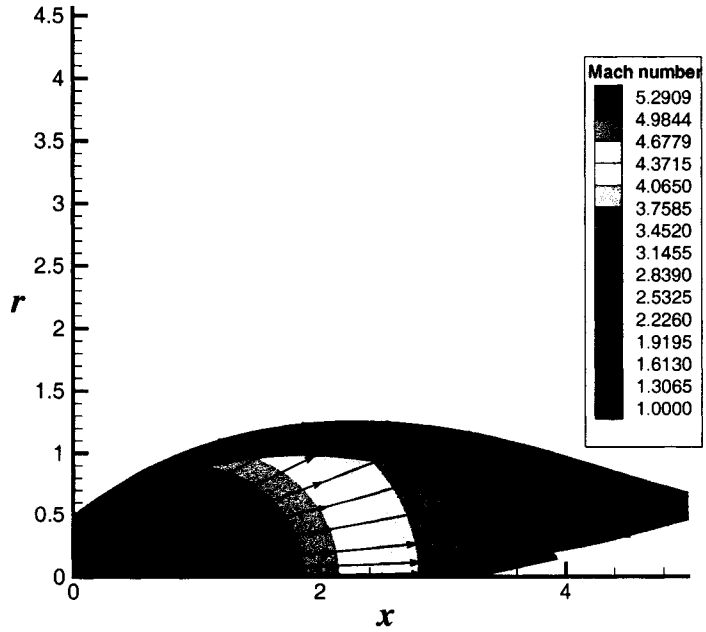

(b) MOC; NC = 89, PC = 11.

Figure 3.8. Streamline contours; $M_e = 1$, $p_e/p_\infty = 10$, $p_e = 1$ MPa.

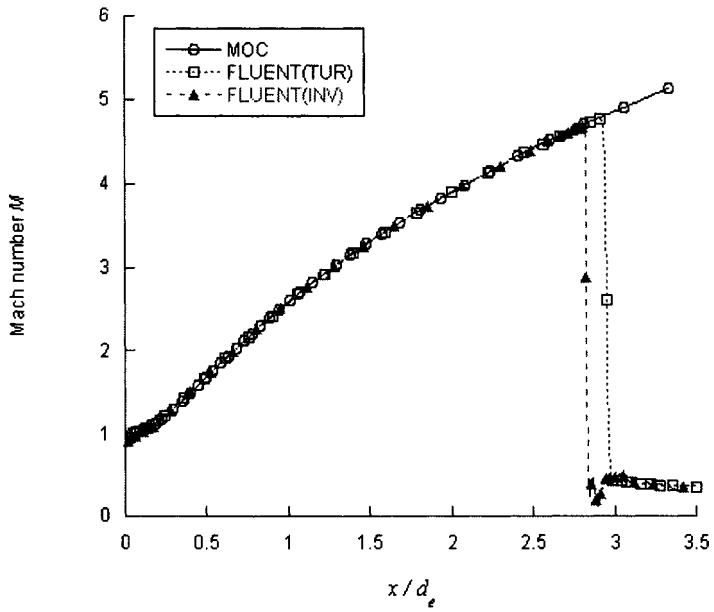

(a) the Mach number distribution along the jet axis.

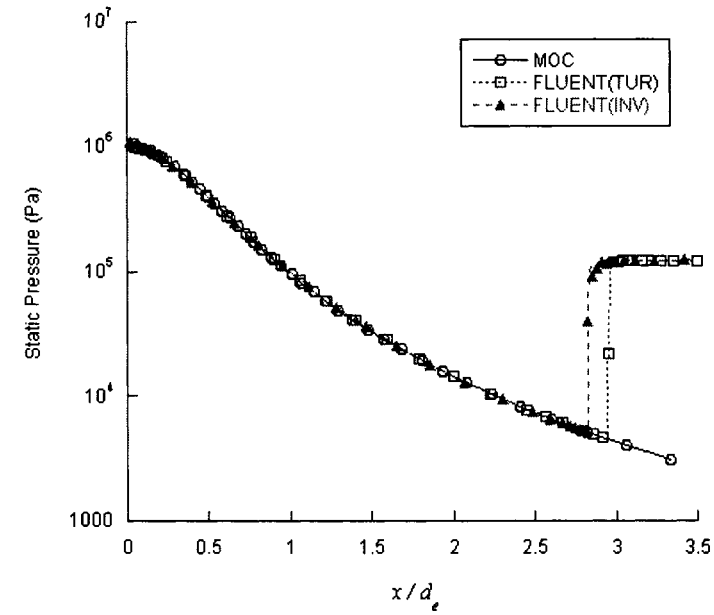

(b) Static pressure distribution along the jet axis.

Figure 3.9. Flow property distributions along the jet axis; $M_e = 1$, $p_e/p_\infty = 10$, $p_e = 1$ MPa.

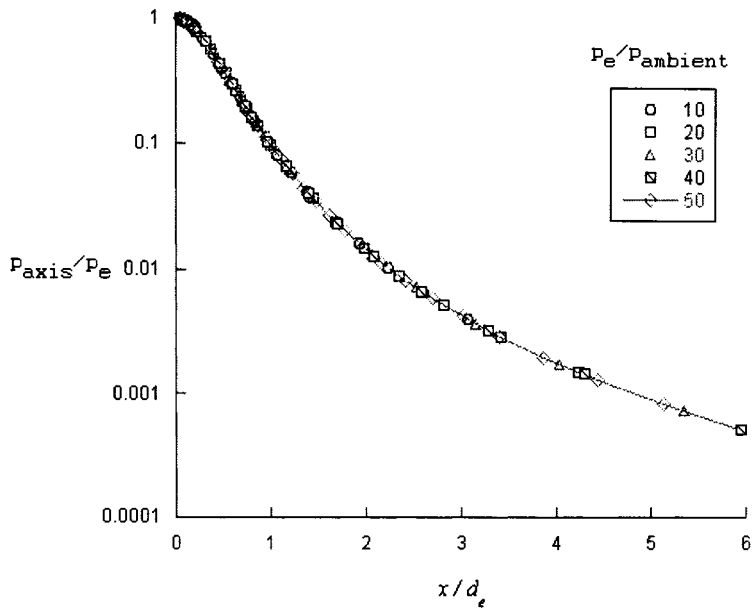

(a) Static pressure ratio distribution along the jet axis

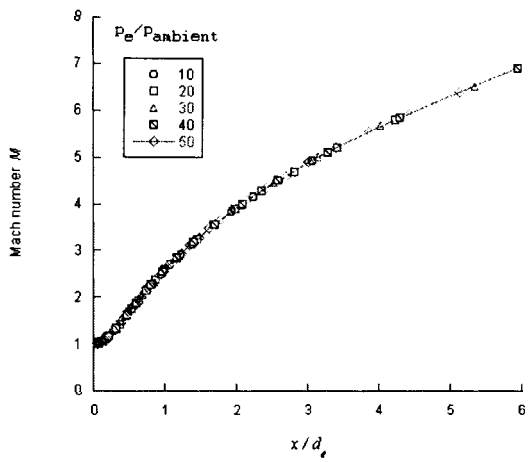

(b) Mach number distribution

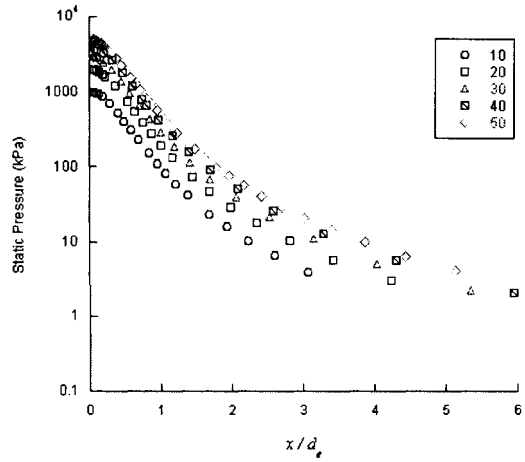

(c) Static pressure distribution

Figure 3.10. MOC results of the flow property distributions along the jet axis for various injection pressure ratios; $P_{ambient} = 0.1$ MPa, $M_e = 1$.

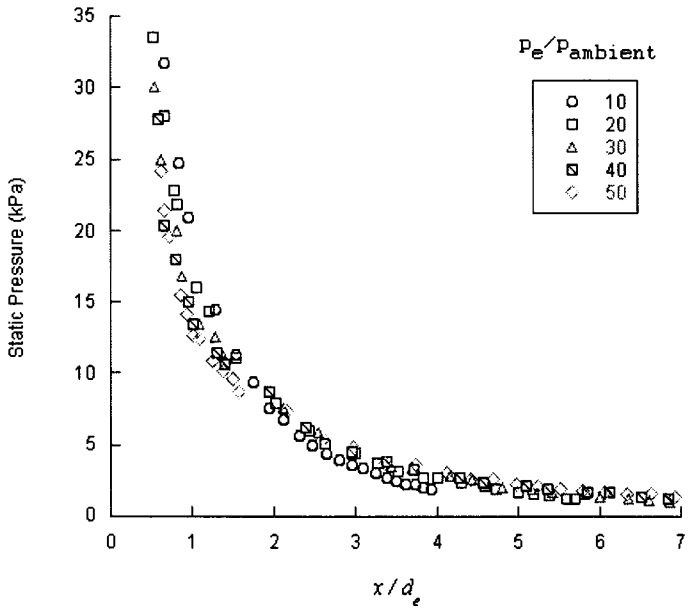

(a) Static pressure distribution before the incident shock

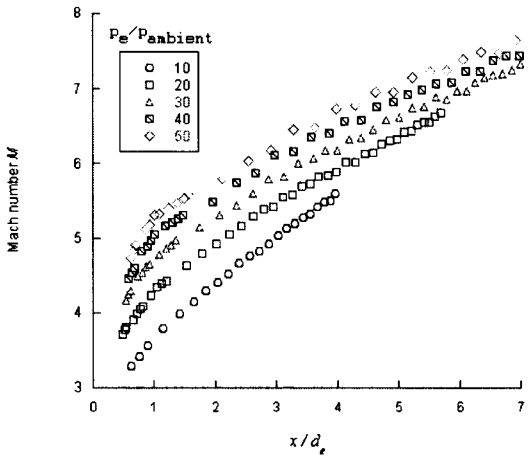

(b) Mach number distribution

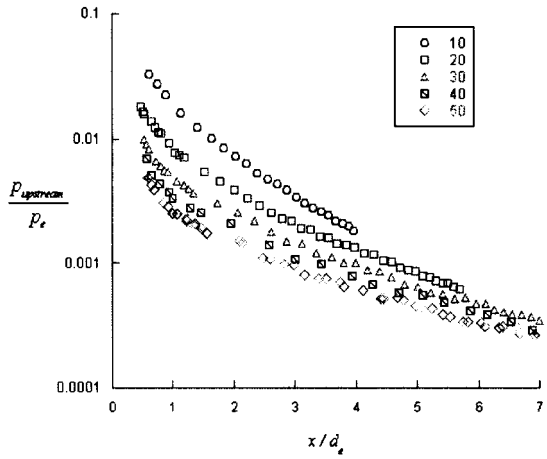

(c) Static pressure ratio distribution

Figure 3.11. MOC results of the flow property distributions before the incident shock wave for various injection pressure ratios; $P_{ambient} = 0.1$ MPa, $M_e = 1$.

because the nozzle-exit Mach number, M_e, is fixed at one. Since the Mach number at a given axial location on the axis remains constant regardless of p_e(Fig. 3.10 b), the pressure ratio, p_{axis}/p_0 at the axial location is constant regardless of p_e. Consequently, the pressure ratio, p_{axis}/p_e, at a given location on the axis is proved to be constant regardless of p_e by multiplication of p_{axis}/p_0 and p_0/p_e, as shown in Eq. 3.1.

$$\frac{p_{axis}}{p_e} = \frac{p_{axis}}{p_0}\frac{p_0}{p_e} = constant \tag{3.1}$$

The local static pressure, Mach number and local static pressure ratio upstream of the incident shock wave are plotted for five injection pressure ratios in Fig. 3.11. In Fig. 3.11 (b), the Mach number profile shifts upward as the injection pressure ratio increases. In contrast, in Fig. 3.11 (a), the upstream static pressures seem to be on the same line for various injection pressure ratios . This means that the static pressure upstream of an incident shock has a certain value depending on the axial distance from the nozzle exit, no matter what the injection pressure ratio is and this dependency can be expressed as

$$p_{upstream} \simeq fn\left(\frac{x}{d_e}\right) \tag{3.2}$$

Thus though at a given axial location in front of the incident shock, the pressure ratio, $p_{upstream}/p_e$, decreases (Fig. 3.11 c), the value of absolute pressure, $p_{upstream}$, (in kPa say) remain approximately the same. The rise in stagnation pressure, p_0 with increasing p_e/p_∞ almost exactly compensates for the drop in pressure ratio , $p_{upstream}/p_e$ at this location. This is in contrast to the situation on the axis that p_{axis}/p_e is the same with increasing stagnation pressure and thus the absolute pressure, p_{axis} at the axis increases.

$$\frac{p_{upstream}}{p_e}\frac{p_e}{p_0}p_0 = p_{upstream} = constant \tag{3.3}$$

3.4. Criterion for the Triple Point

As discussed in Section 3.3.1, it is necessary to decide the location of a triple point, from which a Mach disc starts, on the incident shock in the MOC computation. The MOC computation by itself will not predict this point. Only when the injection pressure is low enough, the incident shock can be reflected at the axis and the Mach disc will not occur in the jet flow and so the MOC correctly depicts the physical situation. The location of the Mach disc is related to the strength of an incident shock wave and a geometric restriction caused by the necessity of having flow parallel to the axis at the axis of symmetry.

It has been suggested that the strength of an incident shock can be characterized by the static pressure behind the incident shock and that a Mach disc occurs at the point where the downstream static pressure reaches a minimum (see Ref. [10]). However, since the upstream flow conditions also change along the shock, it is not clear at all to insist that only the downstream static pressure determines the Mach disc location. In addition, the static pressure varies in a relatively narrow range behind the incident shock, as the largest static pressure drop (90%) occurs at the nozzle exit (see Fig. 3.6 and 3.11).

The characteristic net in Fig. 3.13 shows the expansion and compression wave behavior and the formation and development of the incident shock wave clearly. Figure 3.14 shows the flow properties ahead of the incident shock wave for pressure ratio of 10. The points on the graph represent intersection points for the characteristic net with the incident shock. The upstream Mach number increases continuously and the local static pressure ahead of the incident shock decreases gradually in the downstream direction, ranging from 3.5% to 0.1% of the nozzle exit static pressure. The static pressure ahead of the incident shock is denoted by p_I.

Shock wave reflection has been studied both experimentally and numerically by many previous investigators and is well developed theoretically (see Section 2.2.3). However, there are essential differences between the previous research and the problem of interest in this dissertation.

The flow conditions described by the existing shock wave reflection models are described below (see Fig. 3.12).

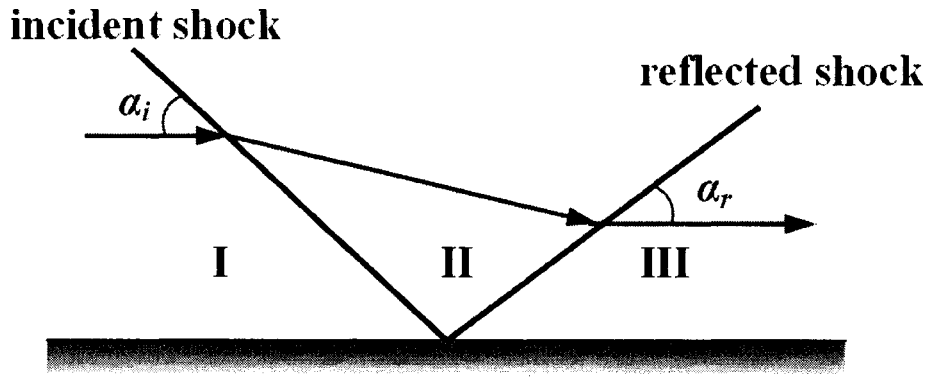

(a) regular reflection

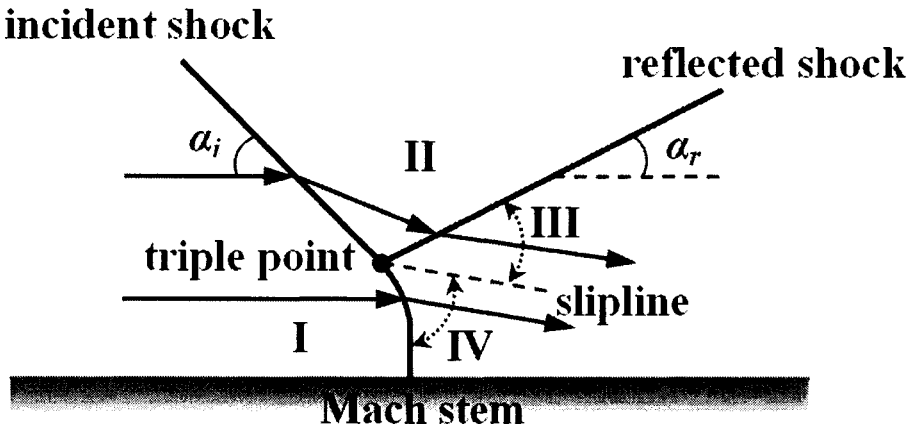

(b) Mach reflection

Figure 3.12. Schematic illustration of the wave configuration.

1. The flow is uniform before the incident shock.

2. The streamline is parallel to the axis of symmetry (wall) before the incident shock (zero angle of attack).

3. The flow is two dimensional.

However, the underexpanded axisymmetric jet has flow conditions described below (see Fig. 3.8 and 3.11).

1. The flow is totally nonuniform before the incident shock. Flow properties change continuously along the incident shock.

2. The streamline is not parallel to the axis of symmetry before the incident shock. Instead,

the flow approaches the incident shock with a finite angle of attack.

3. The flow has an axisymmetry.

In spite of these differences, many features of the existing shock-wave-reflection model can be applied properly to the incident shock wave analysis of the underexpanded axisymmetric jet for the following reasons.

1. Since the shock wave is a very thin region, it is reasonable to consider local values of flow properties such as flow direction, pressure, Mach number, and shock angle.

2. For the same reason, the flow downstream of an incident shock depends only on local flow deflection across the shock for given upstream conditons.

3. The theory developed for two dimensional flow can be applied locally to the axisymmetric flow, since the radial effect is negligible in a thin region, such as a shock wave.

Consequently, the shock polar concept discussed in Section 2.2.3 can be applied to the underexpanded axisymetric flow based on local considerations in the vicinities of the incident shock wave. Thus, it may be possible to apply the von Neumann and detachment criteria to the incident shock of the jet to predict the location of the triple point for a Mach disc in the jet. Shock polars in the pressure-flow angle plane (the (p, θ)-plane) for the incident shock are useful in the development of a criterion for the location of the triple point. Figure 3.13 shows the six representative points (denoted by A ~ F) on the incident shock and the shock polars for these points are shown in Fig. 3.15.

A shock polar in the (p, θ)-plane is the locus of all possible static pressures behind an oblique shock wave as a function of deflection angle for given upstrThe exact location of the triple point might be found using the negative five criterion discussed in connection with axially symmetric jets, but this was not done here.eam conditions. The shock polars plotted in Fig. 3.15 are with the static pressure coordinate nondimensionalized by the local upstream static pressure, p_I, and the flow angle coordinate measured relative to the local upstream flow direction. The initial point of the incident shock polar corresponds to the upstream flow properties ($p = p_I$, $\theta = 0°$). For shock polars plotted relative to the local upstream flow direction, the pressure axis is a vertical line at $\theta = 0°$ and is illustrated with a dotted line in Fig. 3.15. Note that a clockwise flow deflection angle is considered positive in the shock polar of this dissertation.

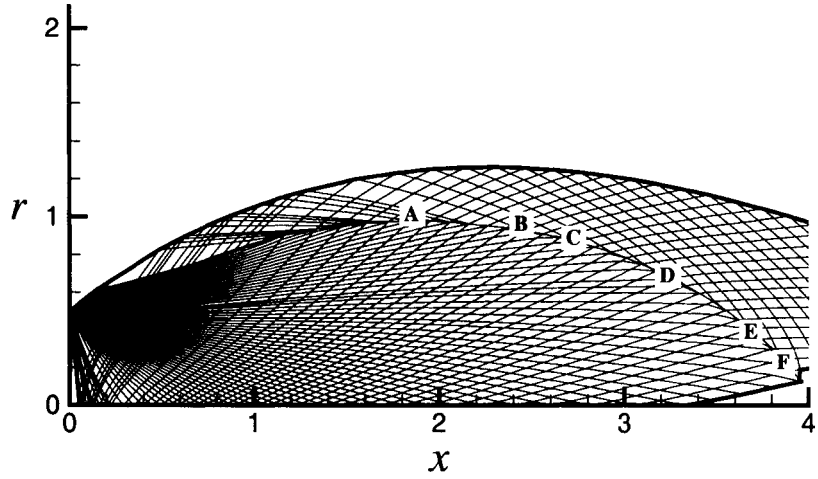

Figure 3.13. Characteristic net for the static pressure ratio of 10 with $M_e = 1$, $p_e = 1$ MPa.

The complete shock polar diagram is composed of an incident shock polar and a reflected shock polar as discussed in Section 2.2.3. The incident shock polar changes shape as the upstream static pressure decreases along the incident shock wave, and shock strength increases. As the incident shock strength increases, the reflected shock polar moves upward (since flow deflection increases across the shock), so the intersection point between the pressure axis ($\theta = 0°$) and the reflected shock polar also moves upward. At point B, the von Neumann criterion is satisfied and the detachment criterion is satisfied at point D. Detailed descriptions of each point are presented in Table 3.1. The region between points B and D is the dual solution domain, where both regular reflection and Mach reflection are possible. The regular reflection→Mach reflection transition can occur at point B or point D or some point in between. From the experimental data (Love and Grigsby, 1959) and the CFD results in Fig. 4.21 (a), the Mach disc is located between point B and D. That is, Mach disc is located in the dual solution domain for the incident shock wave.

Both von Neumann and detachment criteria are useful in defining the region containing a Mach disc but fail in predicting the exact position of the Mach disc (strictly speaking, the location of the triple point). Note that even in the classical uniform flow situation both regular reflection and Mach reflection are possible. For the incident shock wave problem, streamlines are not parallel to the axis of symmetry, nor is the flow uniform before the shock.

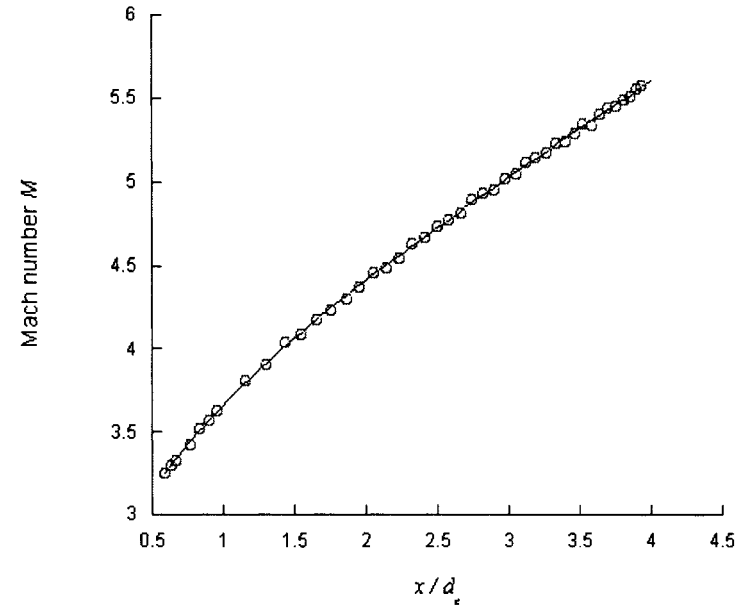

(a) Upstream Mach number distribution.

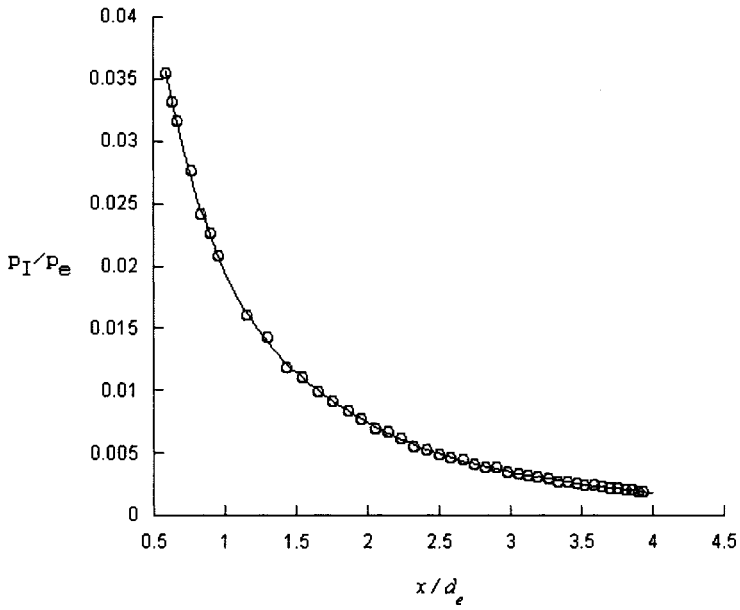

(b) Upstream pressure distribution.

Figure 3.14. Upstream flow property distribution along the incident shock; $M_e = 1$, $p_e/p_\infty = 10$, $p_e = 1$ MPa.

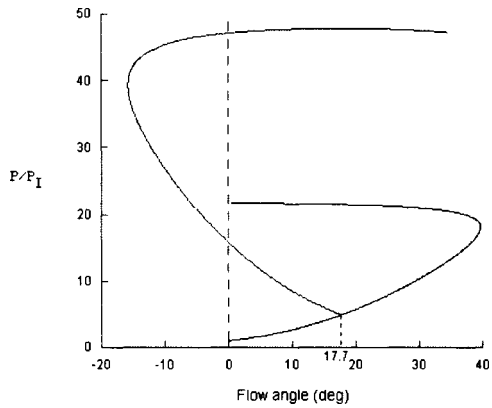

(a) at point A, $\alpha_i < \alpha_N$

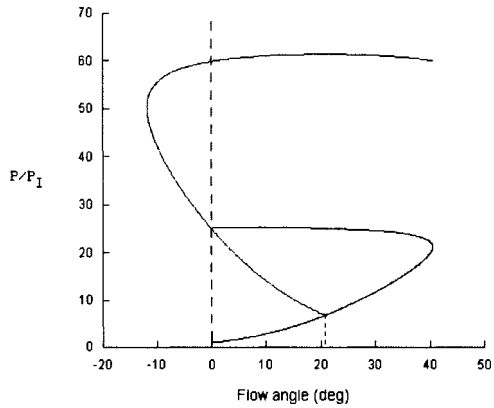

(b) at point B, $\alpha_i = \alpha_N$ (the von Neuamnn criterion)

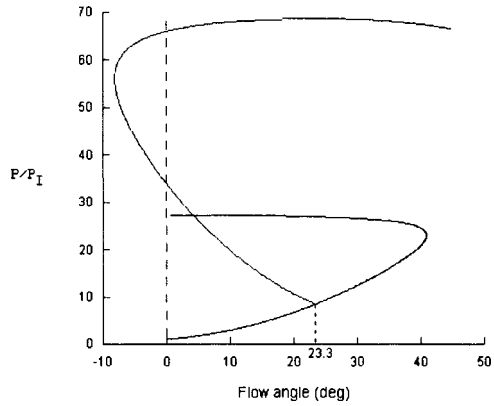

(c) at point C, $\alpha_N < \alpha_i < \alpha_D$

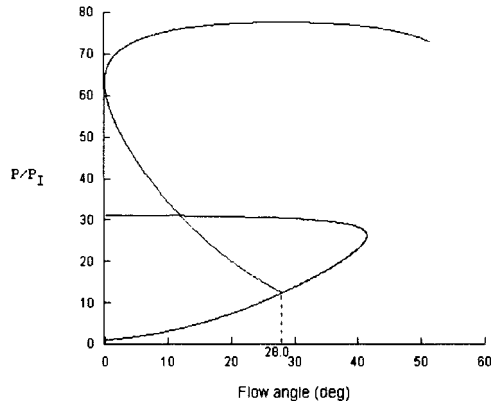

(d) at point D, $\alpha_i = \alpha_D$ (the detachment criterion)

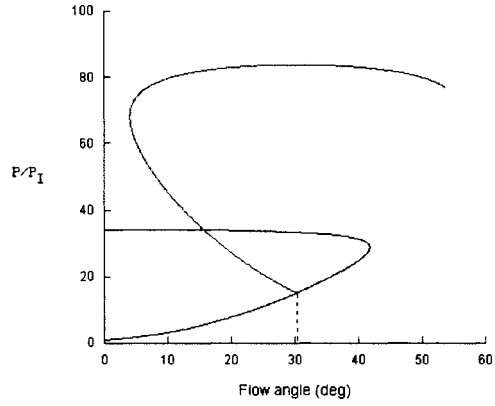

(e) at point E, $\alpha_i > \alpha_D$

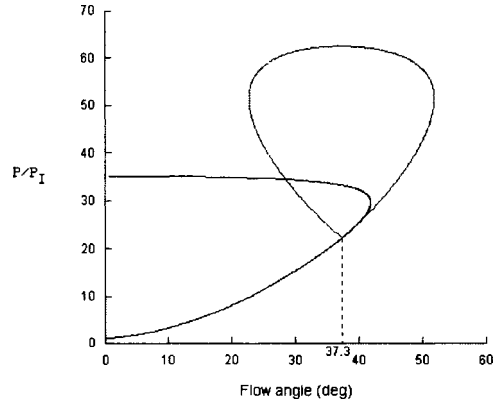

(f) at point F, $\alpha_i \gg \alpha_D$

Figure 3.15. Shock polars in the pressure-flow angle plane along the incident shock; flow angle is relative to the local upstream flow direction; $M_e = 1$, $p_e/p_\infty = 10$, $p_e = 1$ MPa; (a) $\alpha_i < \alpha_N$, (b) $\alpha_i = \alpha_N$, (c) $\alpha_N < \alpha_i < \alpha_D$, (d) $\alpha_i = \alpha_D$, (e) $\alpha_i > \alpha_D$, and (f) $\alpha_i \gg \alpha_D$.

Point	x/d_e	r/d_e	$M_{upstream}$	$\theta_{upstream}$	$\theta_{downstream}$	$\Delta\theta$	Note
A	1.87	0.981	4.32	27.69°	10.00°	17.69°	$\alpha_i < \alpha_N$
B	2.43	0.936	4.67	21.64°	0.85°	20.79°	von Neumann criterion, $\alpha_i = \alpha_N$
C	2.74	0.873	4.86	18.32°	−5.00°	23.32°	negative five criterion, $\theta = -5°$
D	3.29	0.661	5.18	11.89°	−16.10°	27.99°	detachment criterion, $\alpha_i = \alpha_D$
E	3.69	0.409	5.43	6.85°	−23.41°	30.26°	$\alpha_i > \alpha_D$
F	3.85	0.254	5.50	4.33°	−32.99°	37.32°	$\alpha_i \gg \alpha_D$

Table 3.1. Upstream flow properties and locations on the incident shock wave; $M_e = 1$, $p_e/p_\infty = 10$, $p_e = 1$ MPa.

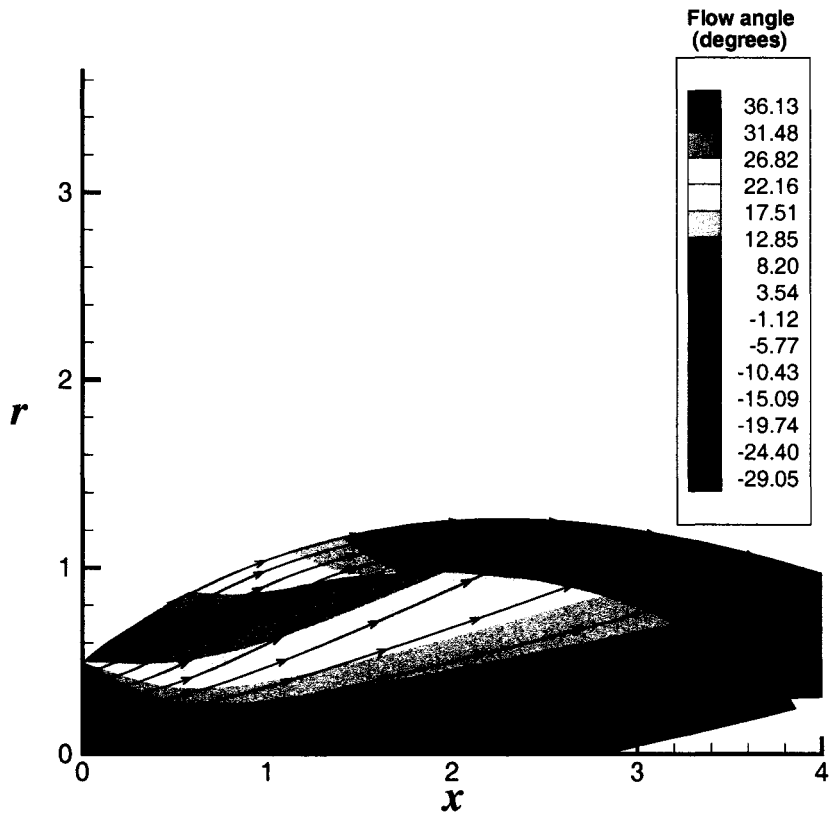

Figure 3.16. Flow angle contour and streamlines; $M_e = 1$, $p_e/p_\infty = 10$, $p_e = 1$ MPa.

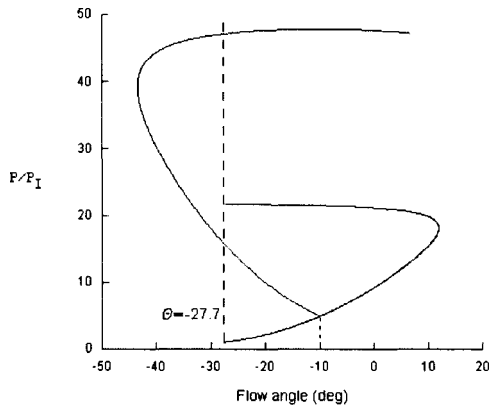

(a) at point A, $\alpha_i < \alpha_N$

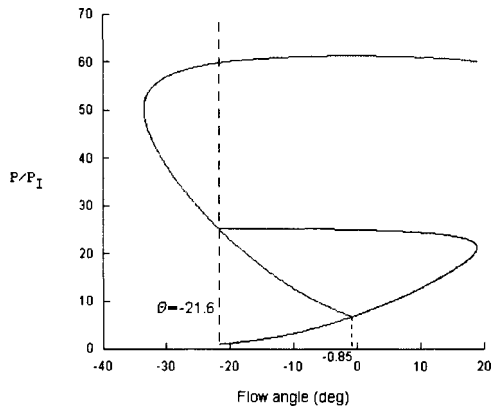

(b) at point B, $\alpha_i = \alpha_N$ (the von Neumann criterion)

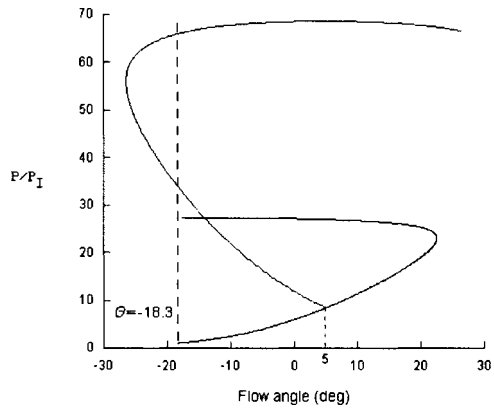

(c) at point C, $\alpha_N < \alpha_i < \alpha_D$

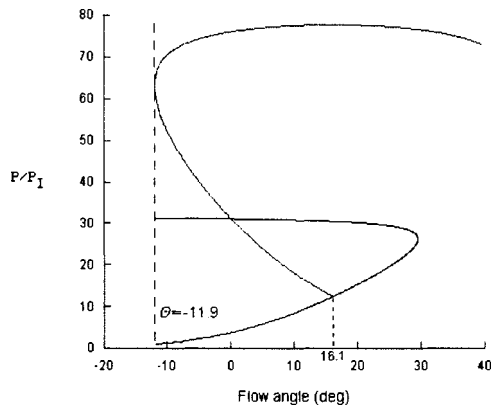

(d) at point D, $\alpha_i = \alpha_D$ (the detachment criterion)

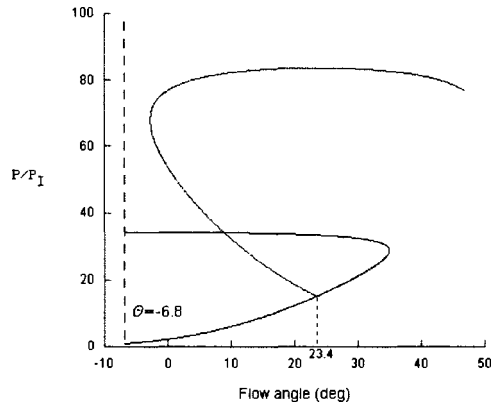

(e) at point E, $\alpha_i > \alpha_D$

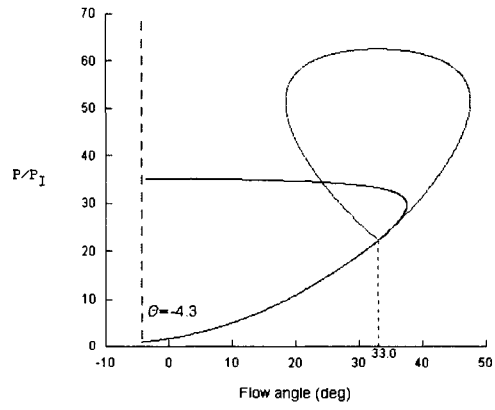

(f) at point F, $\alpha_i \gg \alpha_D$

Figure 3.17. Shock polars in the pressure-flow angle plane along the incident shock; flow angle is relative to the horizontal (axis of symmetry) ; $M_e = 1$, $p_e/p_\infty = 10$, $p_e = 1$ MPa; (a) $\alpha_i < \alpha_N$, (b) $\alpha_i = \alpha_N$, (c) $\alpha_N < \alpha_i < \alpha_D$, (d) $\alpha_i = \alpha_D$, (e) $\alpha_i > \alpha_D$, and (f) $\alpha_i \gg \alpha_D$.

The existing criteria were made for the flow parallel to the axis of symmetry. The streamlines are illustrated in Fig. 3.16 and it shows that the flow angle changes from 36° to 0° before the incident shock. The discrepancy between the streamline and the axis of symmetry affects the flow behavior and shock reflection process. Therefore, we need a new criterion which overcomes the discrepancy of the geometric restriction (the nonuniform flow unparallel to the axis of symmetry) and situates a Mach disc inside the axisymmetric underexpanded jet.

Shock polars at points A - F are redrawn on the basis of the axis of symmetry in Fig. 3.17. The flow angle is measured from the fixed standard line, the axis of symmetry. Since the flow angle decreases before the incident shock, the actual pressure axis shifts to the right. The flow angle behind the incident shock varies from 20° to −29° in Fig. 3.16. Combining all the effects and variables, one can conclude that the flow angle behind the incident shock is the important parameter to indicate the geometric restriction level and to determine the location of the Mach disc. By comparison with experimental data, we found out that a triple point is situated at the point of the flow angle downstream of an incident shock, $\theta_{downstream} = -5°$. For convenience, we have named this criterion as the "negative five" criterion. The evaluation of the "negative five" criterion will be presented in next section.

3.5. Discussion

The "negative five" criterion is that a triple point is located at the point on the incident shock wave, where the flow angle downstream of the incident shock is negative five degrees, and Mach disc is developed from this point. The negative five criterion is evaluated for the nozzle-exit-to-ambient static pressure ratios ranging from 2 to 50. The MOC computation was performed for two nozzle exit Mach numbers ($M_e = 1$ or 1.5) with 150 set of characteristic lines; NC varies from 55~80 and PC varies from 5 to 10. The axial distance and diameter of a triple point are averaged for each pressure ratio and nondimensionalized by the nozzle exit diameter. The results are drawn with a solid line and compared with experimental data and CFD results in Figures 3.18 and 3.19. The negative five criterion predictions show a good agreement with experiments in axial distance of a triple point for both nozzle exit Mach numbers. However, there are discrepancies between the negative five

criterion predictions and experiments in Mach disc diameter at the high pressure ratios. On the other hand, CFD results agree well with the negative five criterion prediction in Mach disc diameter for $M_e = 1$. Actually, the experimental data of Mach disc diameter are not enough to determine the relation with the injection pressure ratio.

The expressions of the axial location of a triple point are derived as a function of the injection pressure ratios from the negative five criterion graphs in Fig. 3.18.

For $M_e = 1$,

$$\frac{x_{tr}}{d_e} = 0.81601 \left(\frac{p_e}{p_\infty} \right)^{0.5226} \tag{3.4}$$

For $M_e = 1.5$,

$$\frac{x_{tr}}{d_e} = 1.2185 \left(\frac{p_e}{p_\infty} \right)^{0.49659} \tag{3.5}$$

Crist *et al.* (1966) suggested the approximate expression for the Mach disc location.

$$\frac{p_0}{p_\infty} \simeq 2.4 \left(\frac{x_M}{d_e} \right)^2 \tag{3.6}$$

If we convert the stagnation pressure into the static pressure in this equation using $p_0/p = (1 + (\gamma - 1) M^2/2)^{\gamma/(\gamma-1)}$,

$$\frac{x_M}{d_e} = \sqrt{\frac{1}{2.4} \left(1 + \frac{(\gamma - 1) M_e^2}{2} \right)^{\gamma/(\gamma-1)}} \left(\frac{p_e}{p_\infty} \right)^{0.5} \tag{3.7}$$

By substituting the value of 1 and 1.5 to M_e for the gas of $\gamma = 1.4$, the Crist relation produces following relations.

For $M_e = 1.0$,

$$\frac{x_M}{d_e} = 0.88810 \left(\frac{p_e}{p_\infty} \right)^{0.5} \tag{3.8}$$

For $M_e = 1.5$,

$$\frac{x_M}{d_e} = 1.23677 \left(\frac{p_e}{p_\infty} \right)^{0.5} \tag{3.9}$$

Expansion chamber pressure (Pa)	420	100	50	28	18
Static pressure ratio	92.02	386.5	772.9	1380.3	2147.2
Crist *et al.* Eq. (3.8)	2.66	5.47	7.73	10.33	12.88
QGD	2.58	4.93	7.75	9.16	13.79
QGDR	2.74	5.24	7.90	10.80	13.93
Experiment	2.7	6.1	8.5	11.6	15.25
The negative five criterion, Eq. (3.4)	2.71	5.74	8.25	11.17	14.08

Table 3.2. Validation of the negative five criterion by comparison with experiments and numerical results; the axial distance of Mach disc is measured from the nozzle exit plane in mm and compared for each injection pressure ratio; $p_0 = 73200$ Pa, $p_e = 38650$ Pa, $M_e = 1.01$, $T_0 = 295$ K, $d_e = 0.313$ mm.

The Equation (3.4) can be validated by comparison with the experimental data of Graur *et al.* [33]. Graur *et al.* measured densities and rotational temperatures in hypersonic axisymmetric jet of N_2 based on diagnostics by high-sensitivity Raman spectroscopy and performed the numerical calculations based on the quasi-gasdynamic (QGD) approach, and its generalization (QGDR) for the breakdown of rotational-transitional equilibrium. The stagnation pressure of the prechamber was 73200 Pa and the static pressure of the expansion chamber was set to 420, 100, 50, 28, and 18 Pa. The nozzle exit diameter is 0.313 mm and chamber temperature is 295 K and Mach number at the nozzle exit was 1.01. The results are compared in Table 3.2. The negative five criterion predictions are closer to the experimental results than any other method for all pressure ratios. Even though Eq. (3.4) is derived from the pressure ratio range of 2 to 50, the negative five criterion produces the most accurate predictions of the Mach disc location for very high pressure ratios up to 2147. The discrepancies of the Mach disc location between the negative five criterion and experiments are caused by the fact that the negative five criterion predicts the axial distance of a triple point, x_{tr} not the axial distance to Mach disc at the axis, x_M(see Fig. 3.1).

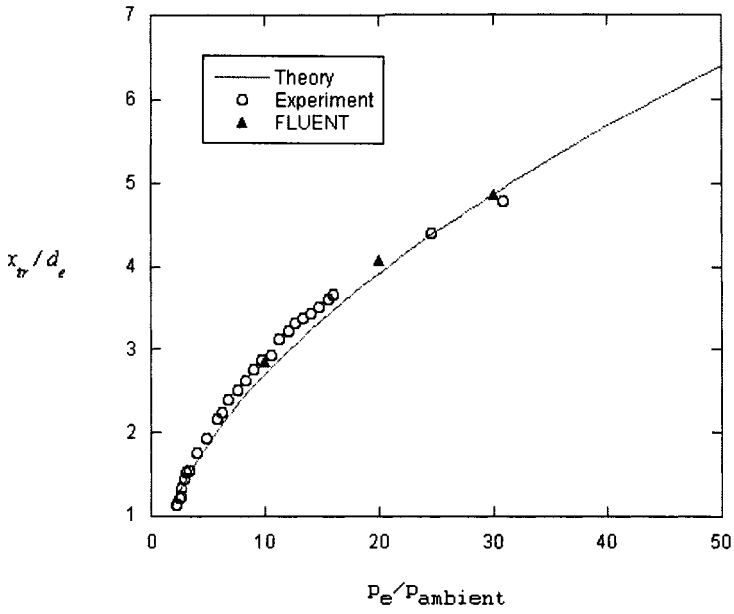

(a) $M_e = 1.0$

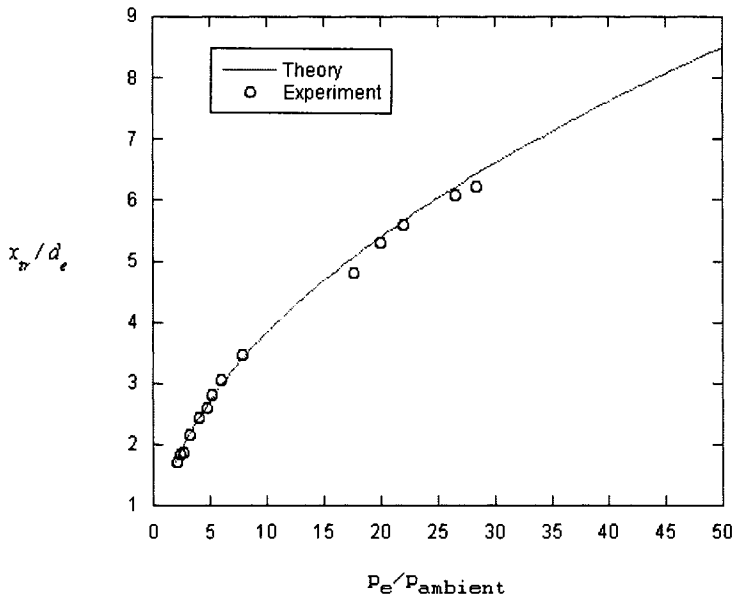

(b) $M_e = 1.5$

Figure 3.18. Nomdimensional axial distance of a triple point for the various nozzle exit to ambient pressure ratios; $p_{ambient} = 0.1$ MPa.

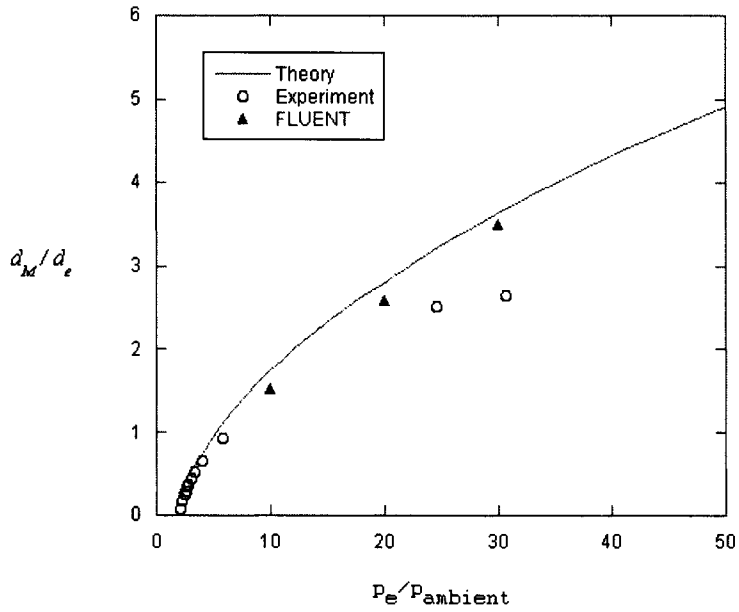

(a) $M_e = 1.0$

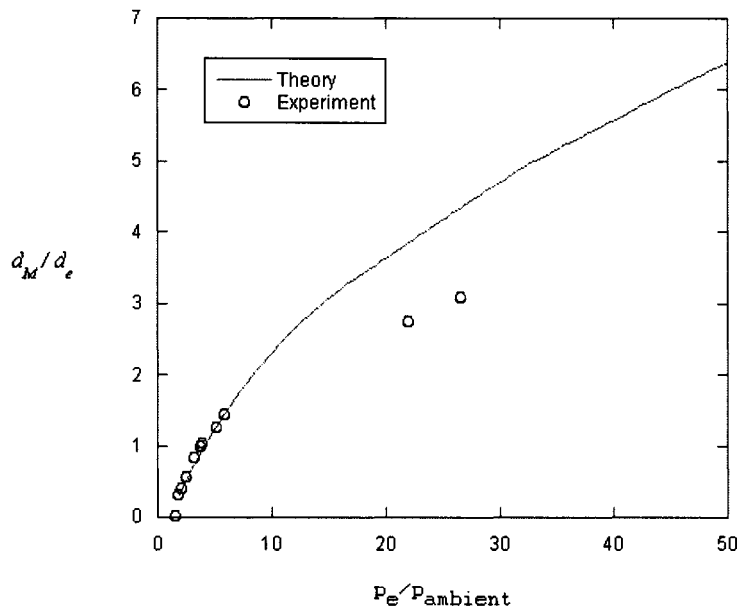

(b) $M_e = 1.5$

Figure 3.19. Nomdimensional diameter of a Mach disc for the various nozzle exit to ambient pressure ratios; $p_{ambient} = 0.1$ MPa.

Chapter 4

Underexpanded Annular Jet Analysis

4.1. Introduction

When fuel is injected from a shrouded valve at high pressure, a nearly annular jet is produced at the injection system. The annular jet has seldom been studied both numerically and experimentally in spite of its frequent appearance in many engineering applications, such as plug nozzle injection, annular propulsive systems and high pressure valve injection. Figure 4.1 shows experimental results for the annular jet issuing from a truncated plug nozzle (see detail in Ref. [13]). Although there have been some attempts to calculate the plug nozzle flow using the method of characteristics (MOC), the MOC has been applied only to simple regions of the annular jet flow. The method of characteristics has not been applied to the entire flowfield of an annular jet, so the details of the flow structure in an annular jet are not clearly understood. The objective of this chapter is to study the flowfield issuing from an annulus and apply both the method of characteristics and CFD to the jet flow with annular geometry.

Schematics of an annular jet are pictured in Fig. 4.2. The annulus is composed of two circles: the outer circle and the inner circle. The radius of outer circle is called r_{outer} and the radius of inner circle r_{inner} as shown in Fig. 4.2 (c). The difference between r_{outer} and r_{inner} is denoted by Δr.

$$\Delta r = r_{outer} - r_{inner} \tag{4.1}$$

The radius of the annulus is defined as

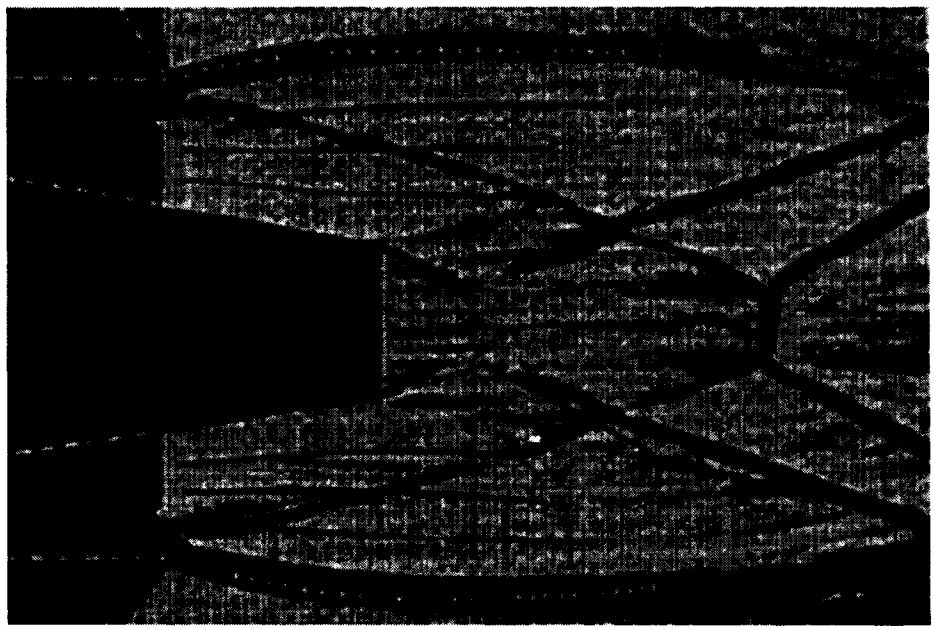

Figure 4.1. Experimental flow-fields for an annular jet issuing from the truncated plug nozzle with $A_{exit}/A_{throat} = 1.555$, $L/L_{max} = 0.480$ and $p_0/p_\infty = 7.353$ (from Ref. [13]).

$$r_{annulus} = \frac{r_{inner} + r_{outer}}{2} \tag{4.2}$$

In the MOC calculations, the radius of annulus, $r_{annulus}$, is varied from 10 units to 50 units and the nozzle-exit-to-ambient static pressure ratio, p_e/p_∞, is also changed from 10 to 20. The ambient (outer region) static pressure, p_∞, and the static pressure of the inner region, p_{inner}, are fixed to 0.1 MPa at $x = 0.0$ and the radius difference, Δr, remains constant of 2 units in all cases. In the plots r and x are given in terms of this same unit.

4.2. MOC Analysis of Annular Jet

The main feature of annular jet is that, unlike the axisymmetric jet, the axis of symmetry of an annular jet is not coincident with the center of the annular jet. The center of the jet in this case is the local value of $r_{annulus}$. Therefore, the MOC must be applied to the entire flowfield of the annular jet, while only half of the jet has to be considered in the MOC analysis of an axisymmetric jet. The overall view of the characteristic net is drawn for a static pressure ratio of 10 and an annulus radius of 40 units in Fig. 4.3. The x- axis is

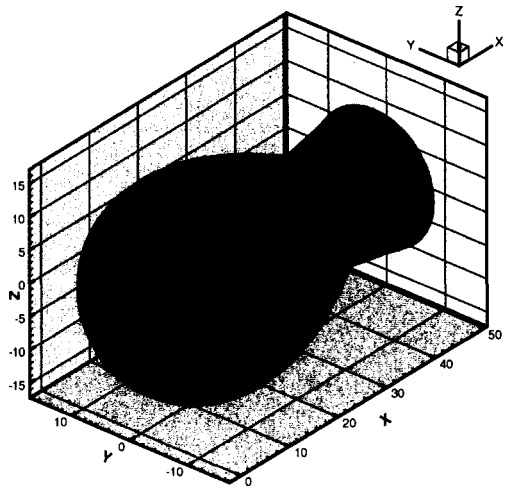

(a) Three-dimensional plot of entire annular jet.

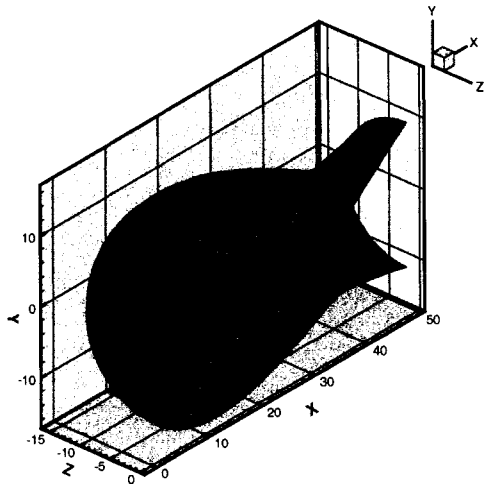

(b) A cross sectional view of an annular jet.

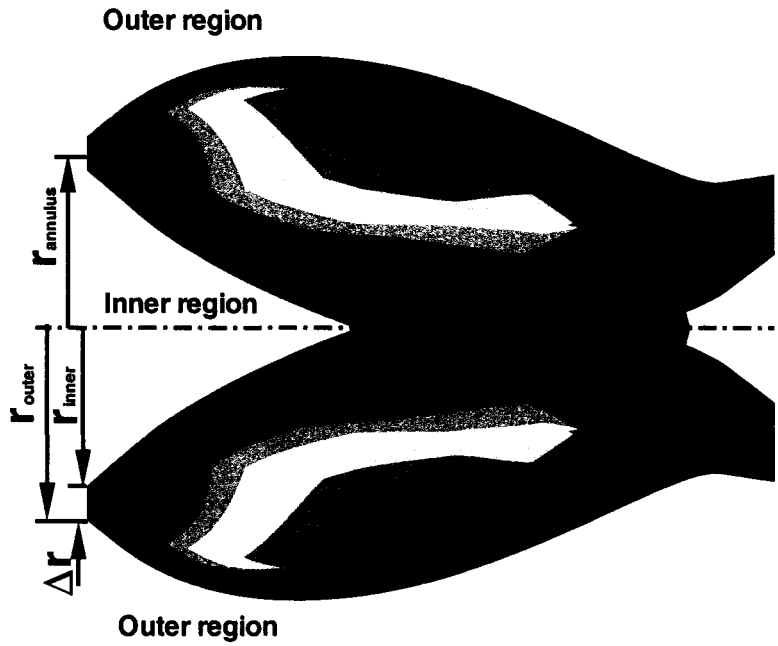

(c) Cross section of an annular jet.

Figure 4.2. Schematics of an annular jet; $r_{annulus} = 10$ units, $\Delta r = 2$ units and $p_{exit}/p_{\infty} = 10$.

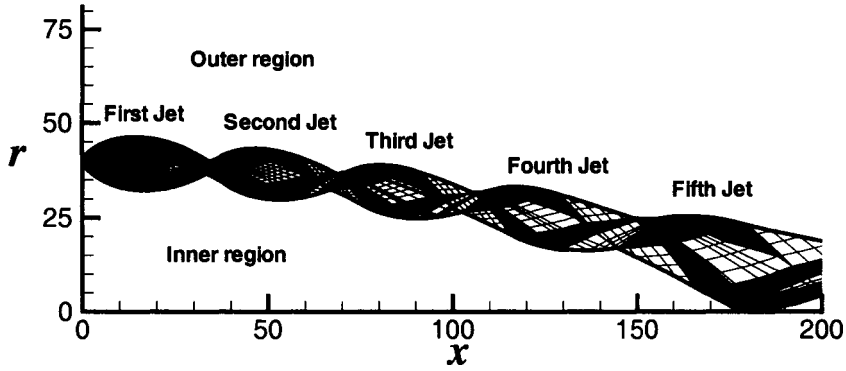

Figure 4.3. The characteristic net of annular nozzle flow; $r_{annulus} = 40$ units, $\Delta r = 2$ units and $p_{exit}/p_\infty = 10$.

the axis of symmetry. Since annular jet has symmetry with respect to the x- axis, only the upper half of the annular jet is drawn. Even though the static pressure is the same in outer and inner regions in this calculation, the jet bends toward the x- axis because of the impact of decreasing radius on mass, momentum, and energy conservation. Note that a two dimensional jet issuing from a slot would not bend toward the axis. Since there is less space near the axis, the jet is enlarged as approaches the axis. A Mach disc occurs at the intersection between the x- axis and the fifth jet boundary and does not occur in the core flows of the previous four jets.

The flow structure of the annular jet is asymmetric to the center of the jet. Therefore, it is necessary to distinguish the outer and inner incident shock waves in each jet structure. The outer incident shock wave is defined as the incident shock wave which is formed and strengthened by the compression waves reflected at the outer jet boundary. Similarly, the inner incident shock wave is defined as the incident shock wave which is formed and strengthened by the compression waves reflected at the inner jet boundary.

As shown in Fig. 4.4, the jet flow issuing from the annular nozzle expands more towards the inner region than outer region because of the effect of decreased radius on the flow. The compression waves reflected at the inner jet boundary spread out more than the compression waves reflected at the outer jet boundary, so the inner incident shock is formed further

	Mach number				
Jet	First	Second	Third	Forth	Fifth
Outer boundary	2.567	2.428	2.362	2.333	2.314
Inner boundary	2.567	2.415	2.305	2.230	2.175
	Stagnation pressure (MPa)				
Jet	First	Second	Third	Forth	Fifth
Outer boundary	1.89514	1.52619	1.37735	1.31717	1.27866
Inner boundary	1.89514	1.49674	1.26062	1.12268	1.02874

Table 4.1. Flow properties at jet boundary; $r_{annulus} = 40$ units, $\Delta r = 2$ units and $p_{exit}/p_{\infty} = 10$.

downstream than the outer incident shock. Also, the inner incident shock wave is weaker than the outer incident shock wave.

Figure 4.5 shows the intersection between the inner and outer incident shock waves. Unlike the axisymmetric nozzle flow, a Mach disc does not occur in the core flow of annular jet because the flow behind the reflected shock does not need to be parallel to the axis of symmetry as in axisymmetric nozzle flow. After the shock intersection, the outer incident shock-1 becomes the outer incident shock-2 and the inner incident shock-1 becomes the inner incident shock-2. Since the outer incident shock-1 is stronger than the inner incident shock-1, the outer incident shock-2 is stronger than the inner incident shock-2. In Fig. 4.5 (b), points A, B, C, D and D' are located at the shock intersection but have different local flow properties. The flow properties at point B are determined by the outer incident shock angle-1 and upstream flow properties at point A and the flow properties at point C are determined by the inner incident shock angle-1 and upstream flow properties at point A, using the oblique shock relations in Section 2.2.1. The shock angles of outer incident shock-2 and inner incident shock-2 and flow properties at points D and D' are determined by an iterative process until the flow properties at points D and D' satisfy the following conditions across the slipline in Fig. 4.5 (b).

$$p_D = p_{D'} \tag{4.3}$$

$$\theta_D = \theta_{D'} \tag{4.4}$$

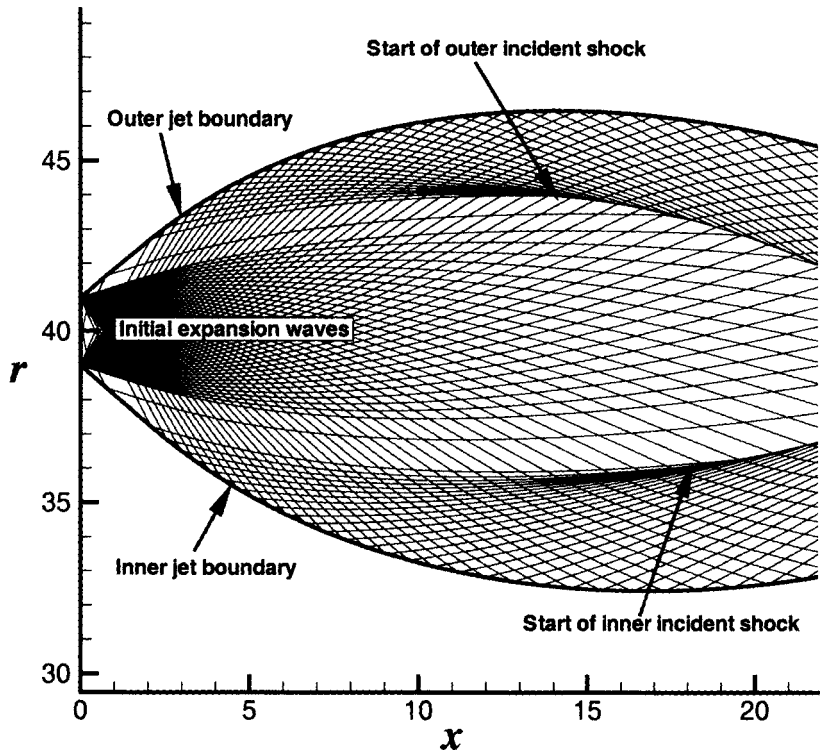

Figure 4.4. Initial expansion waves and the formation of the incident shock waves; $r_{annulus} = 40$ units, $\Delta r = 2$ units and $p_{exit}/p_{\infty} = 10$.

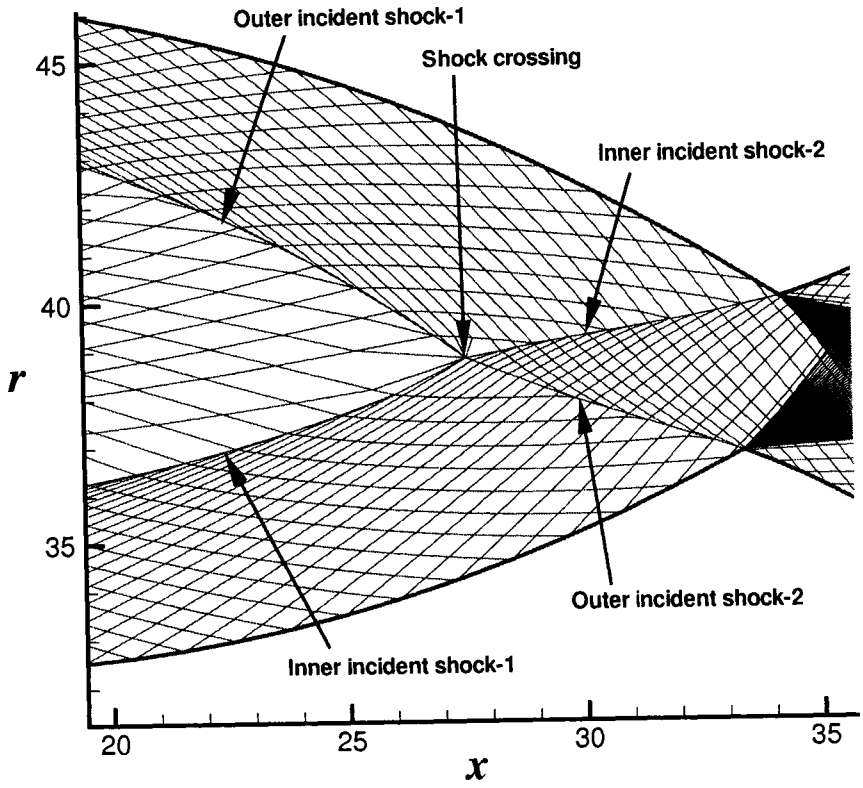

(a) Characteristic net.

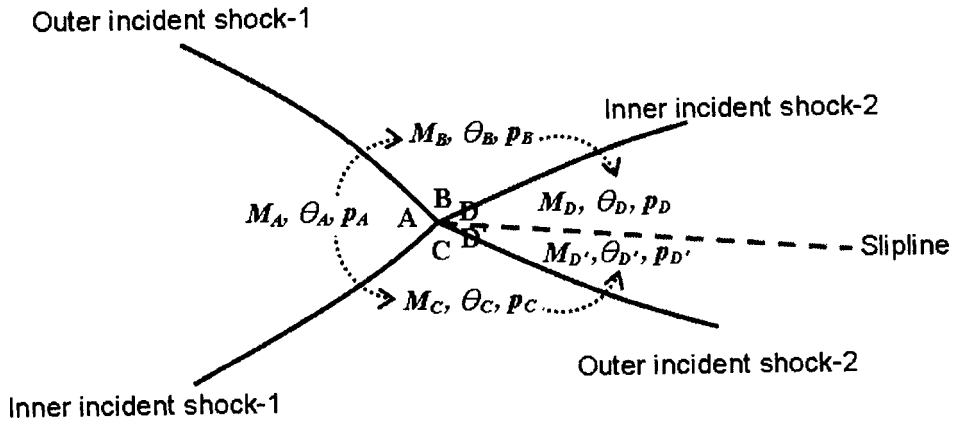

(b) Schmatic of shock crossing.

Figure 4.5. Incident shock wave crossing in the characteristic net of annular jet; $r_{annulus} = 40$ units, $\Delta r = 2$ units and $p_{exit}/p_\infty = 10$.

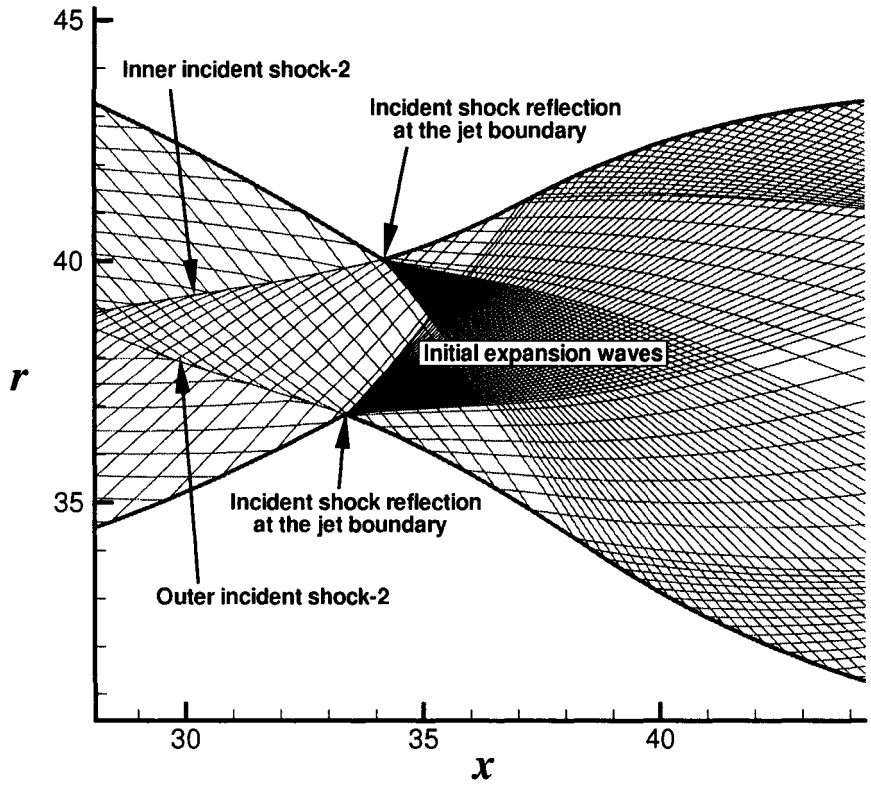

(a) Characteristic net.

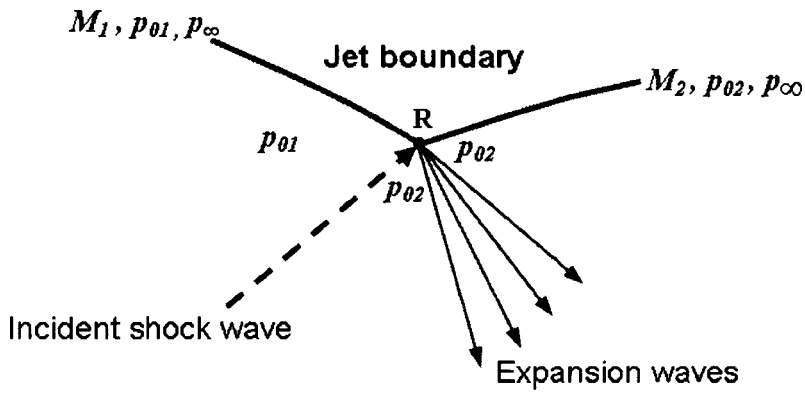

(b) Schematic of shock reflection at jet boundary.

Figure 4.6. Incident shock wave reflection at jet boundary; $r_{annulus} = 40$ units, $\Delta r = 2$ units and $p_{exit}/p_\infty = 10$.

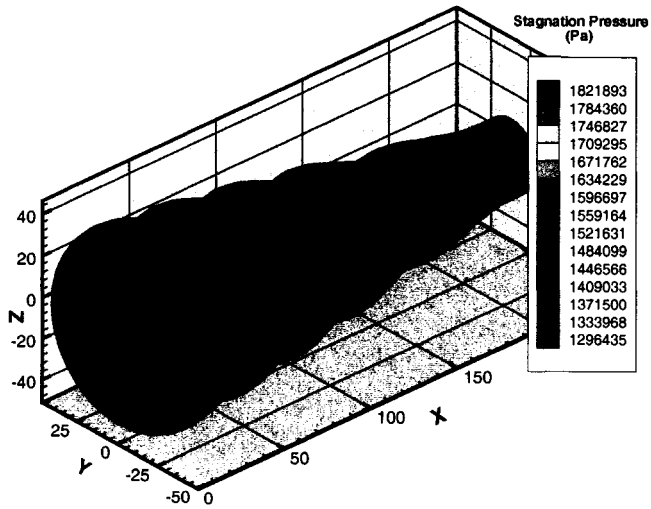

(a) Stagnation pressure contour.

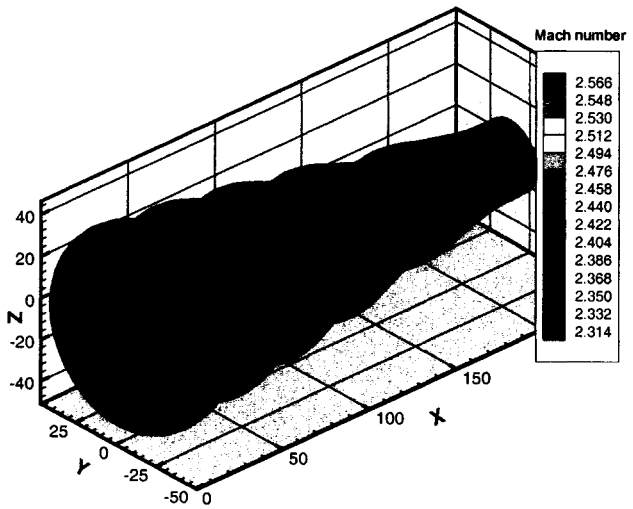

(b) Mach number contour.

Figure 4.7. Flow properties at the jet boundary; $r_{annulus} = 40$ units, $\Delta r = 2$ units and $p_{exit}/p_{\infty} = 10$.

Incident shock waves are reflected as an expansion fans at the jet boundary, as shown in Fig. 4.6. When an incident shock encounters the jet boundary, the jet boundary conditions change. Static pressure at the jet boundary remains same but other properties vary across the incident shock wave. In Fig. 4.6 (b), the stagnation pressure decreases from p_{01} to p_{02} across the incident shock wave and remains constant at p_{02} through the expansion fan to the jet boundary. Since the static pressure at the jet boundary is constant at p_∞, the jet boundary Mach number behind the incident shock wave, M_2, is calculated from following equation:

$$M_2 = \sqrt{\frac{2}{\gamma - 1}\left(\left(\frac{p_{02}}{p_\infty}\right)^{(\gamma-1)/\gamma} - 1\right)} \tag{4.5}$$

Since the outer incident shock-2 is stronger than the inner incident shock-2 in Fig. 4.6 (a), the inner jet boundary Mach number and stagnation pressure are lower than the outer jet boundary Mach number and stagnation pressure after the intersection point with the incident shock wave. The Mach number and stagnation pressure at the jet boundary are plotted in Fig. 4.7 and presented in Table 4.1.

4.3. Comparison of MOC and CFD Predictions for an Annular Jet

4.3.1. Case of $p_{exit}/p_\infty = 10$, $r_{annulus} = 10$ units

The CFD computations were conducted to validate the MOC results of annular jet flow. A coupled implicit solver was used in the CFD computations. Figure 4.10 shows the Mach number contours for $r_{annulus} = 10$ units and $p_{exit}/p_\infty = 10$. The corresponding MOC net is shown in Fig. 4.8. Mach number contours are plotted with the same scale in Fig. 4.10. Figure 4.10 (a) is the CFD result using an invisicd model and Figure 4.10 (b) is the CFD result using the Sparlart-Allmaras turbulence model (one-equation model). In the inviscid model, the first Mach disc takes place in the core flow of the jet and the second Mach disc occurs at $x = 30$ on the x- axis. However, in turbulent flow, Mach disc does not occur in the core flow of the jet but takes place at $x = 26$ on the x- axis. Except for the Mach disc in

the core flow, the jet configurations of both models are very similar to each other initially. Since turbulence should weaken the incident shock, it is reasonable to expect that the Mach disc would occur further downstream in the turbulent model than in the inviscid model. However, the reason for the discrepancy in the existence of Mach disc in the core flow is not known.

The MOC prediction for the same p_{exit}/p_{∞} and $r_{annulus}$ is pictured in Fig. 4.10 (c). The flow structure can be seen clearly in the characteristic net in Fig. 4.8. As in the turbulent CFD result, the Mach disc does not take place in the core flow of the jet. As discussed earlier, the inner incident shock wave is formed downstream of the outer incident shock wave. Shock polar in the (p, θ)- plane is applied to the incident shock of the annular jet flow in Fig. 4.9. The flow change across the outer incident shock satisfies the von Neumann criterion at point A and the detachment criterion at point C. Point B is located at dual solution domain. The upstream flow conditions are summarized in Table 4.2. The upstream Mach number is higher at point B than at point A because the flow is accelerated at the core flow of the jet. However the upstream Mach number at points C is lower than the upstream Mach number at point B because point C is beyond the core flow region. In spite of the decrease of the upstream Mach number, the incident shock strength is increased at point C. (The flow Mach number normal to the shock is larger.) Even thought the upstream Mach number at point D is much lower than the upstream Mach number at point C, the incident shock strength is again increased at point D. This is because the flow angle deflection, $\Delta\theta$ increases in the downstream direction and, for the smaller upstream Mach number, the increased flow angle deflection cause the relatively more augmentaton of the incident shock strength.

When the inner jet boundary meets the axis, an oblique shock is generated at the intersection point to adjust the flow direction to be parallel to the axis. Eventually, a Mach disc occurs between the x- axis and the outer incident shock wave near $x = 35$ because the outer incident shock angle at the axis is greater than the maximum allowable shock angle for the given Mach number at the axis.

In the MOC results, the inner jet boundary meets the x- axis at $x = 15.6$ while the inner jet boundary meets the x- axis at $x = 18$ in CFD results. CFD computations predict a

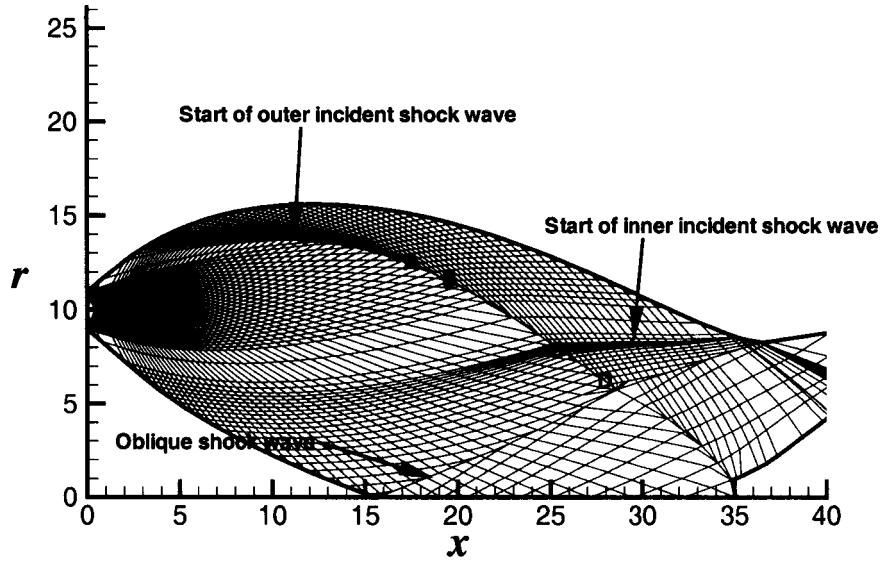

Figure 4.8. Characteristic net; $r_{annulus} = 10$ units and $p_{exit}/p_\infty = 10$.

Point	x	r	$M_{upstream}$	$\theta_{upstream}$	$\theta_{downstream}$	$\Delta\theta$	Note
A	17.37	12.48	4.71	10.95°	−9.96°	20.91°	von Neumann criterion, $\alpha_i = \alpha_N$
B	19.72	11.47	4.76	7.12°	−15.00°	22.12°	$\alpha_N < \alpha_i < \alpha_D$
C	25.23	8.11	4.27	3.97°	−22.34°	26.31°	detachment criterion, $\alpha_i = \alpha_D$
D	27.93	6.26	3.77	5.95°	−20.43°	26.38°	$\alpha_i > \alpha_D$

Table 4.2. Upstream flow properties and locations on the incident shock wave of the annular jet for $M_{exit} = 1$, $p_{exit}/p_\infty = 10$, $p_{exit} = 1$ MPa, $r_{annulus} = 10$ units;.

subsonic recirculation zone near $x = 5$ in the inner region. This cannot be considered using the MOC.

4.3.2. Case of $p_{exit}/p_\infty = 10$, $r_{annulus} = 30$ units

The characteristic net for $p_{exit}/p_\infty = 10$, $r_{annulus} = 30$ units is shown in Fig. 4.11. The points A, B, and C are on the outer incident shock and the points D and E are on the inner incident shock wave. The upstream flow conditions are described in Table 4.3 and shock polars are shown in Fig. 4.12. For the outer incident shock, the von Neumann criterion is satisfied at point A and the detachment criterion is satisfied at point B. However, for the inner incident shock, as shown in Fig. 4.12 (d), the shock strength never reaches the von

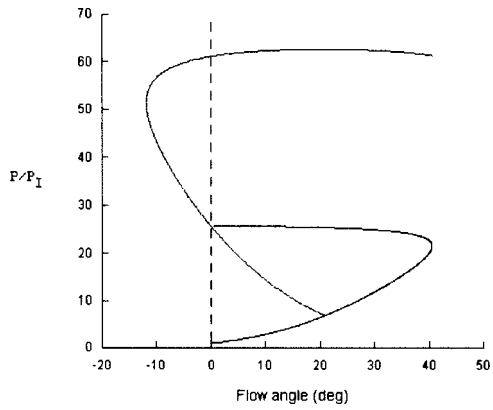

(a) at point A, $\alpha_i = \alpha_N$

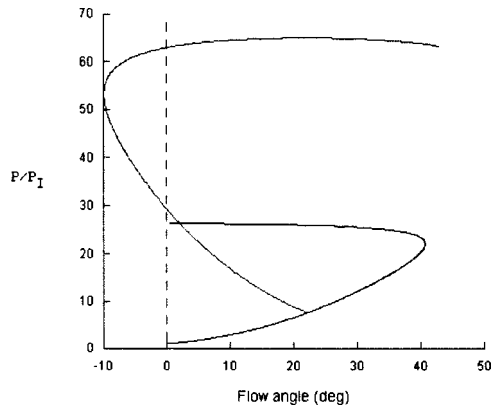

(b) at point B, $\alpha_N < \alpha_i < \alpha_D$

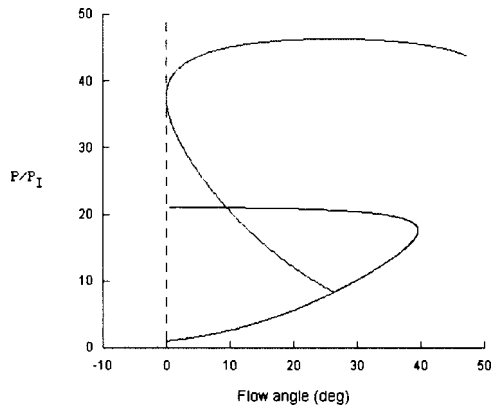

(c) at point C, $\alpha_i = \alpha_D$

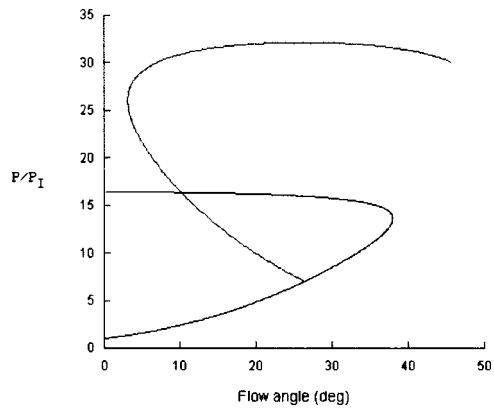

(d) at point D, $\alpha_i > \alpha_D$

Figure 4.9. Shock polars in the pressure-flow angle plane along the incident shock for the annular jet for $M_{exit} = 1$, $p_{exit}/p_\infty = 10$, $p_{exit} = 1$ MPa, $r_{annulus} = 10$ units; flow angle is relative to the local upstream flow direction; (a) $\alpha_i = \alpha_N$, the von Neumann criterion, (b) $\alpha_N < \alpha_i < \alpha_D$, (c) $\alpha_i = \alpha_D$, the detachment criterion, and (d) $\alpha_i > \alpha_D$.

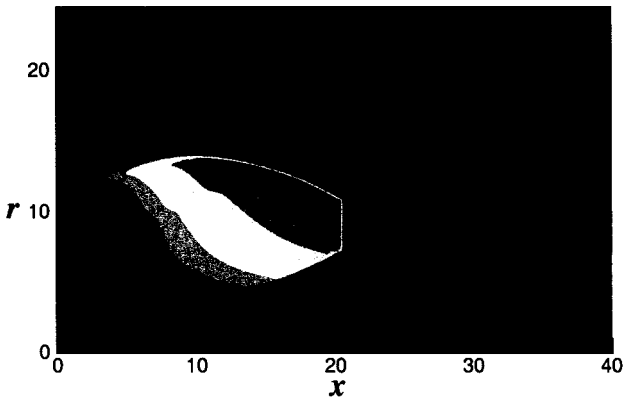

(a) CFD result using inviscid model.

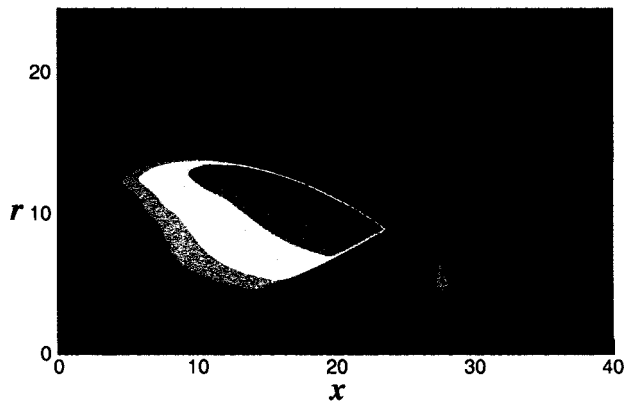

(b) CFD result using one-equation turbulence model.

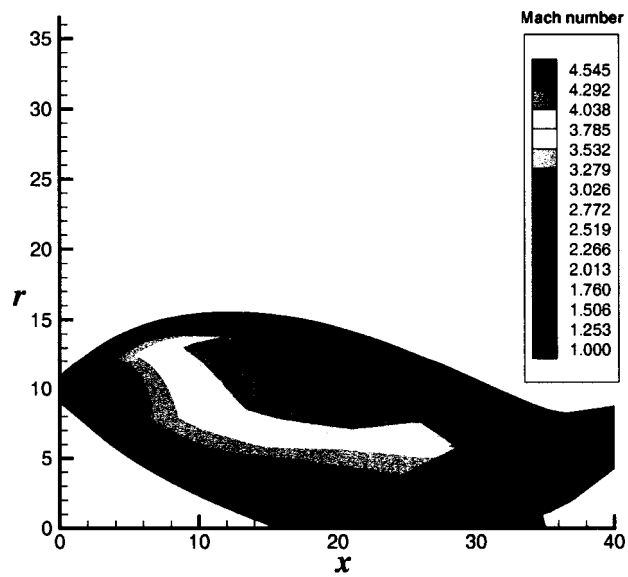

(c) MOC result.

Figure 4.10. Mach number contours plotted with the same scale; $r_{annulus} = 10$ units and $p_{exit}/p_{\infty} = 10$; (a) CFD with invisid model, (b) CFD with one-equation turbulence model, and (c) MOC result.

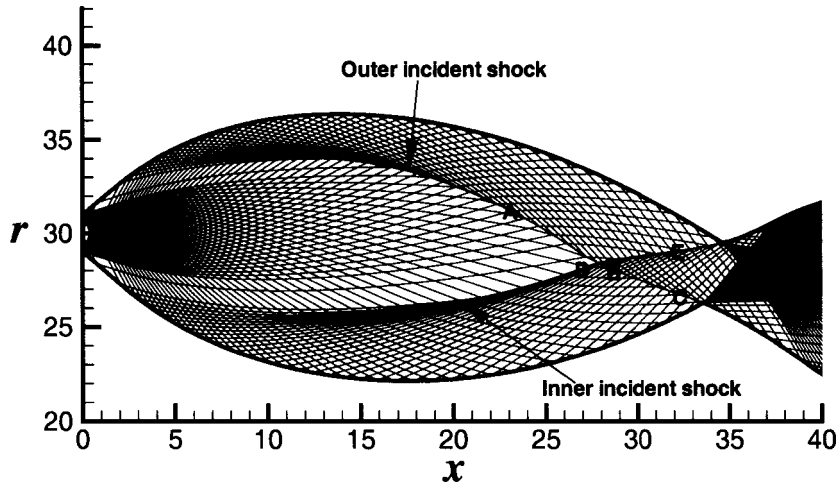

Figure 4.11. Characteristic net; $r_{annulus} = 30$ units and $p_{exit}/p_{\infty} = 10$.

Neumann criterion. The shock polars at the points C and E, which are on the same axial position, show that the outer incident shock is much stronger than the inner incident shock.

Figure 4.13 shows the Mach number contours for $r_{annulus} = 30$ units and $p_{exit}/p_{\infty} = 10$. The Sparlart-Allmaras turbulence model was utilized for the CFD computation. In both CFD and MOC, a Mach disc does not occur until the jet encounters the x- axis and repetitive jet configurations are shown. The annular jet bends more to the axis in the CFD result than in the MOC result. The third repetitive jet structure meets the axis in the CFD prediction while the fourth repetitive jet structure meets the axis in the MOC calculation. In Fig. 4.13 (b), the flow angle at the intersection between the x- axis and jet boundary is greater than the maximum deflection angle allowed for the given jet boundary Mach number, so a Mach type reflection takes place at this point instead of an oblique shock.

4.3.3. Case of $p_{exit}/p_{\infty} = 20$, $r_{annulus} = 30$ units

The characteristic net for is shown in Fig. 4.14. The points A and B are on the outer incident shock wave and the point C is on the inner incident shock wave. The upstream flow conditions are described in Table 4.4 and shock polars are shown in Fig. 4.15. At point A, the von Neumann criterion is satisfied and the detachment criterion is satisfied at point

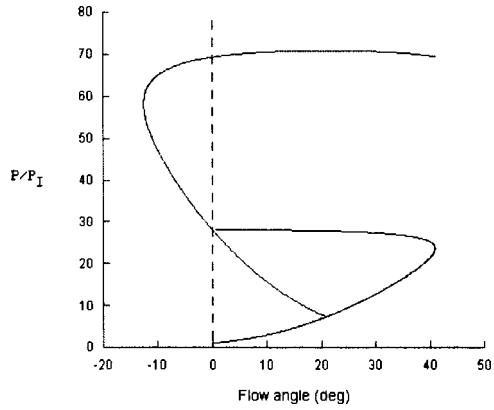

(a) at point A, $\alpha_i = \alpha_N$

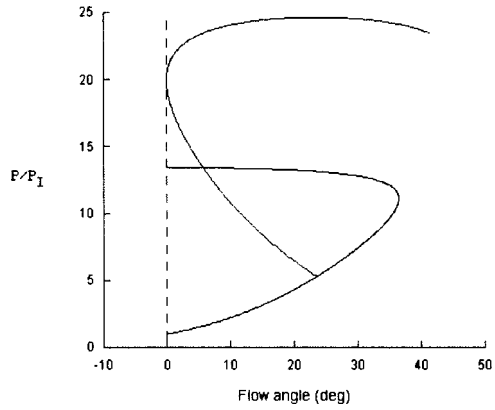

(b) at point B, $\alpha_i = \alpha_D$

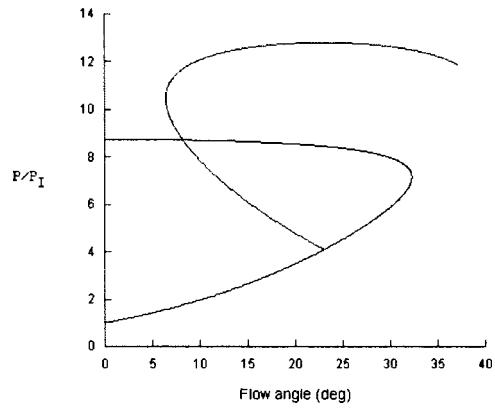

(c) at point C, $\alpha_i > \alpha_D$

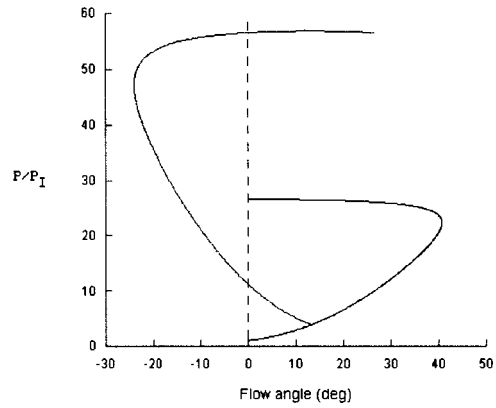

(d) at point D, $\alpha_i < \alpha_N$

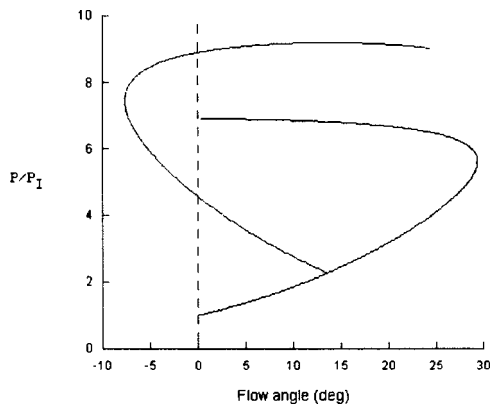

(e) at point E, $\alpha_i < \alpha_N$

Figure 4.12. Shock polars in the pressure-flow angle plane along the incident shock for the annular jet for $M_{exit} = 1$, $p_{exit}/p_\infty = 10$, $p_{exit} = 1$ MPa, $r_{annulus} = 30$ units; flow angle is relative to the local upstream flow direction; (a) $\alpha_i = \alpha_N$, the von Neumann criterion, (b) $\alpha_i = \alpha_D$, the detachment criterion, (c) $\alpha_i > \alpha_D$, (d) $\alpha_i < \alpha_N$, and (e) $\alpha_i < \alpha_N$.

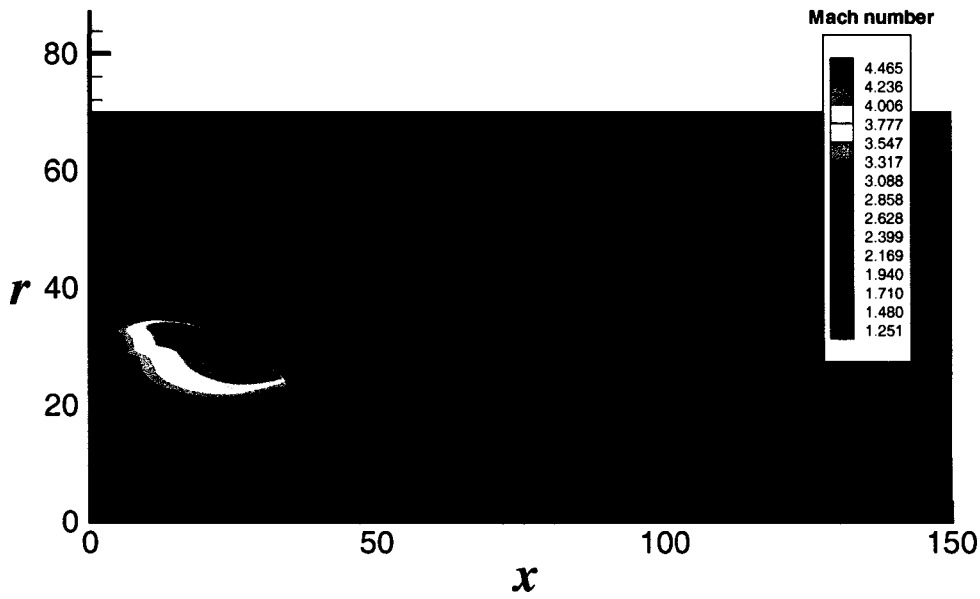

(a) CFD.

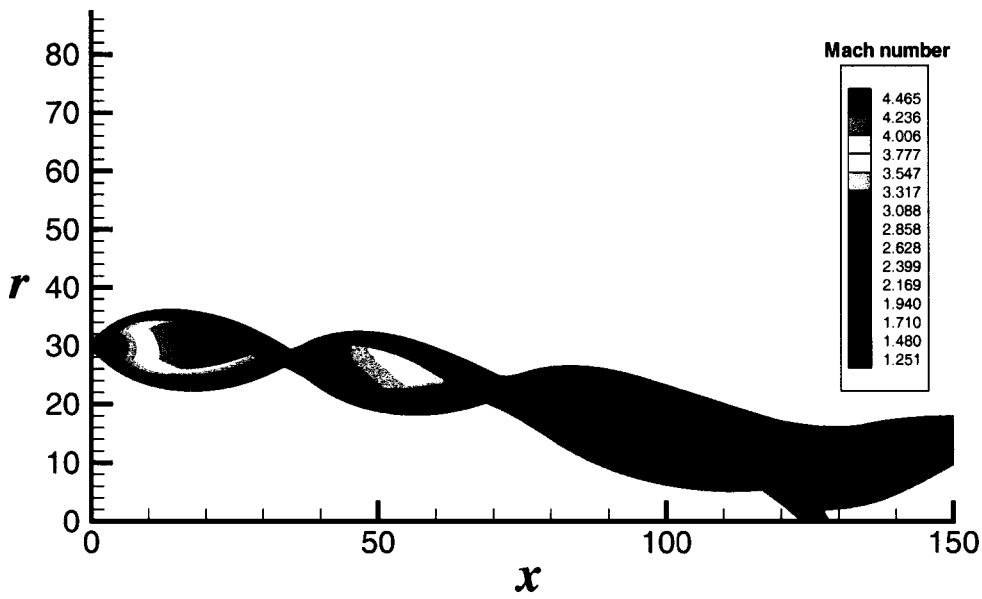

(b) MOC.

Figure 4.13. Mach number contours; $r_{annulus}$ = 30 units and p_{exit}/p_{∞} = 10; (a) CFD with one-equation turbulence model and (b) MOC result.

Point	x	r	$M_{upstream}$	$\theta_{upstream}$	$\theta_{downstream}$	$\Delta\theta$	Note
A	23.60	30.92	4.92	3.56°	−17.31°	20.87°	von Neumann criterion, $\alpha_i = \alpha_N$
B	28.41	28.15	3.41	14.90°	−8.62°	23.52°	detachment criterion, $\alpha_i = \alpha_D$
C	32.08	26.77	2.76	24.71°	1.70°	26.01°	$\alpha_i > \alpha_D$
D	27.06	28.15	4.79	−2.14°	11.00°	13.14°	$\alpha_i < \alpha_N$
E	32.13	29.06	2.46	−25.78°	−12.18°	13.60°	$\alpha_i < \alpha_N$

Table 4.3. Upstream flow properties and locations on the incident shock wave of the annular jet for $M_{exit} = 1$, $p_{exit}/p_\infty = 10$, $p_{exit} = 1$ MPa, $r_{annulus} = 30$ units;.

Point	x	r	$M_{upstream}$	$\theta_{upstream}$	$\theta_{downstream}$	$\Delta\theta$	Note
A	29.52	38.45	5.57	18.16°	−2.57°	20.73°	von Neumann criterion, $\alpha_i = \alpha_N$
B	57.58	23.36	5.82	−4.46°	−33.29°	28.83°	detachment criterion, $\alpha_i = \alpha_D$
C	59.58	20.72	5.50	−6.58°	−2.52°	9.10°	$\alpha_i < \alpha_N$

Table 4.4. Upstream flow properties and locations on the incident shock wave of the annular jet for $M_{exit} = 1$, $p_{exit}/p_\infty = 20$, $p_{exit} = 2$ MPa, $r_{annulus} = 30$ units;.

B. The inner incident shock never reaches the von Neumann criterion as shown in Fig. 4.15 (c).

Figure 4.16 shows the Mach number contours for $r_{annulus} = 30$ units and $p_{exit}/p_\infty = 20$. Again, the Sparlart-Allmaras turbulence model was employed for the CFD computation. A Mach disc occurs in the core flow of the annular jet in the CFD result while no Mach disc occurs in the core flow in the MOC prediction. The flow pattern after the Mach disc is totally different for the CFD and MOC results, as would be expected. Experimental data to determine which prediction is realistic are not available. The triple point on the outer incident shock wave of CFD result is at point D in the MOC result in Fig. 4.14, which is located at the region between the von Neumann and detachment criteria. At point D, the upstream Mach number of the CFD result, 5.61, shows a good agreement with the upstream Mach number of the MOC result, 5.81.

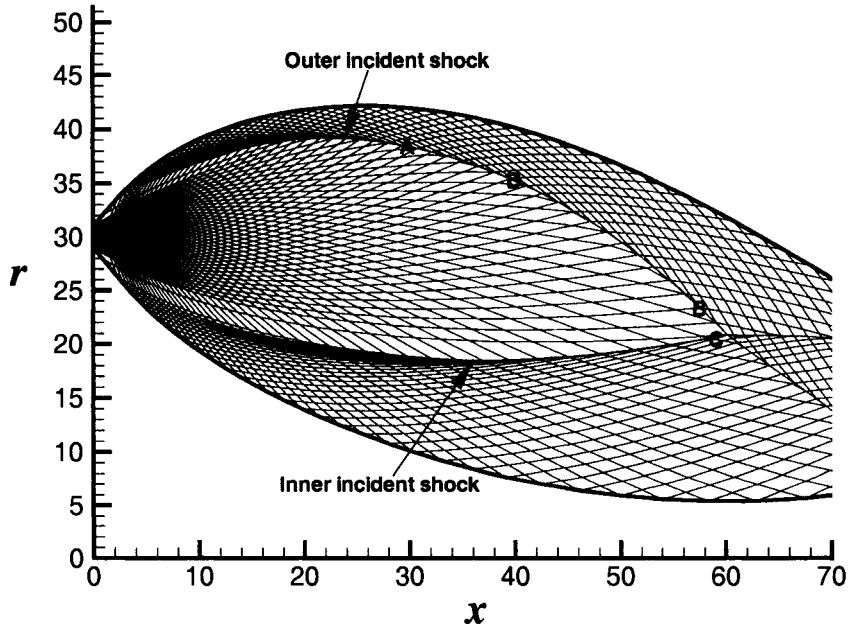

Figure 4.14. Characteristic net; $r_{annulus} = 30$ units and $p_{exit}/p_{\infty} = 20$.

4.4. Additional MOC Predictions

4.4.1. Effect of Pressure Ratio and Annular Radius

Mach number contours of the injection pressure ratio, $p_{exit}/p_{\infty} = 10$ are plotted for various radii of annulus in Fig. 4.17. A Mach disc does not occur in the core flow of the jet issuing from the annular nozzles for any of the annular radii considered when the static pressure ratio is 10, but occurs only at the intersection of the axis of symmetry and the jet. Near the axis of symmetry, as r goes to zero, the radial effect dominates the flow, the jet size is enlarged, and the asymmetry of the jet relative to the jet center is shown distinctively. Three dimensional Mach number contours are presented in Fig. 4.18 in order to illustrate the jet structure more clearly.

Mach number contours for the injection pressure ratio, $p_{exit}/p_{\infty} = 20$ are pictured for various radii of the annulus in Fig. 4.19. In this case, as was true for $p_{exit}/p_{\infty} = 10$, Mach discs are not generated in the core flow of the jet issuing from the annular nozzles but occur only at the intersection of the axis of symmetry and the jet.

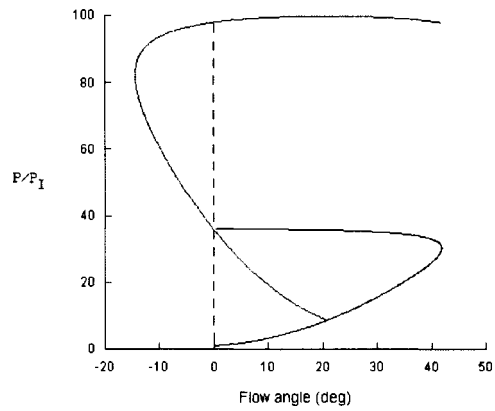

(a) at point

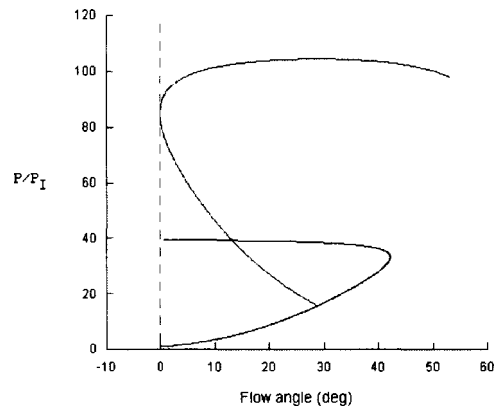

B, $\alpha_i = \alpha_D$

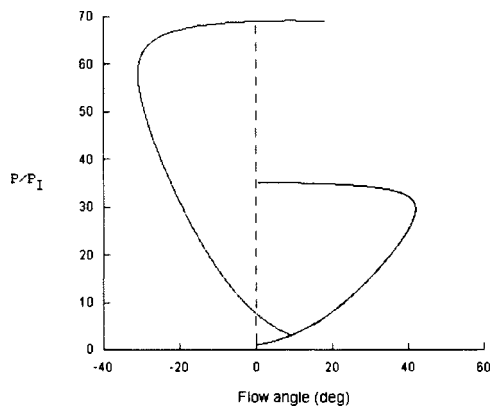

(c) at point C, $\alpha_i < \alpha_N$

Figure 4.15. Shock polars in the pressure-flow angle plane along the incident shock for the annular jet for $M_{exit} = 1$, $p_{exit}/p_\infty = 20$, $p_{exit} = 2$ MPa, $r_{annulus} = 30$ units; flow angle is relative to the local upstream flow direction; (a) $\alpha_i = \alpha_N$, the von Neumann criterion, (b) $\alpha_i = \alpha_D$, the detachment criterion, and (c) $\alpha_i < \alpha_N$.

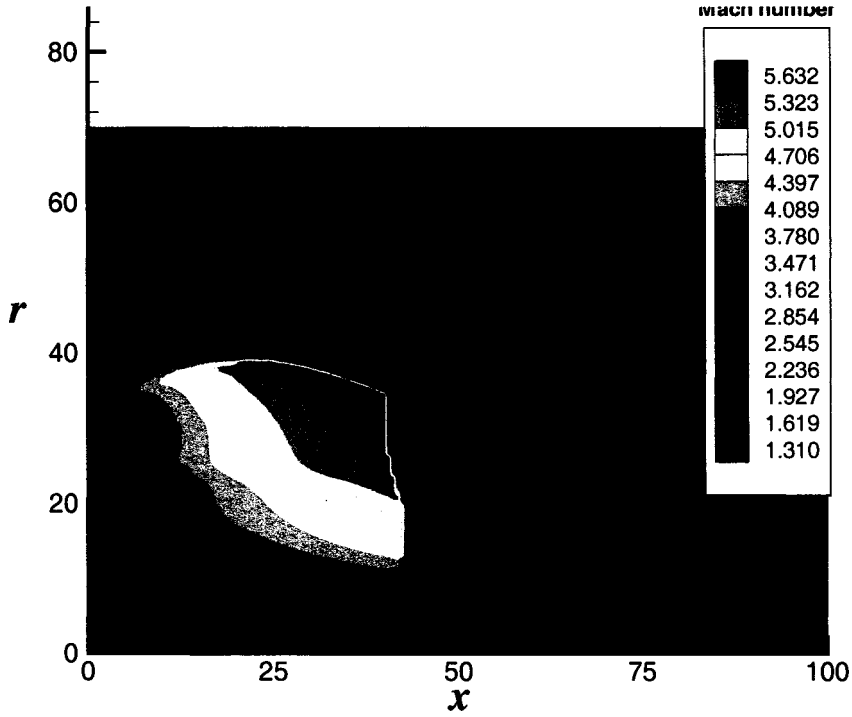

(a) CFD.

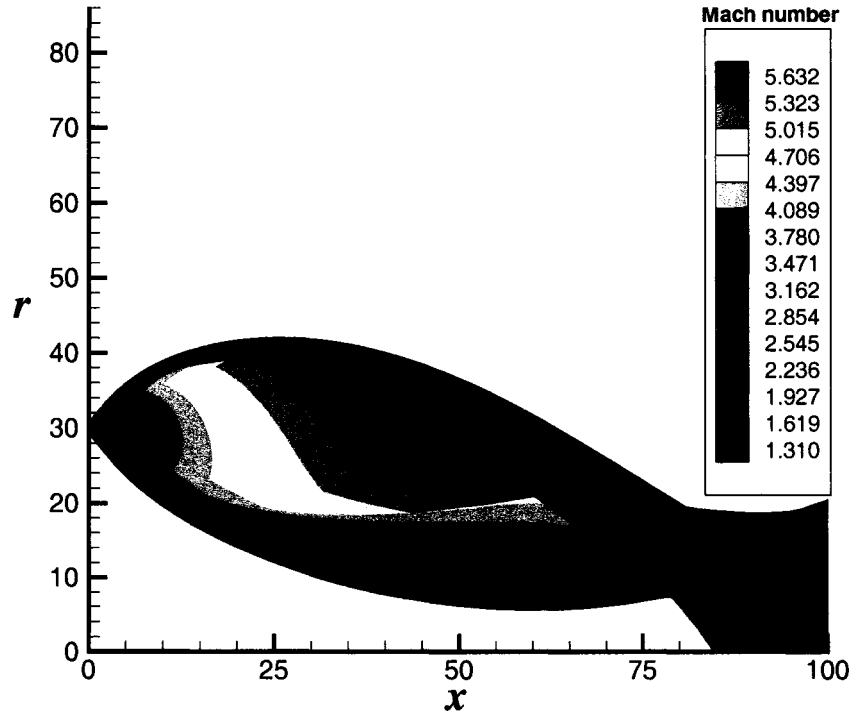

(b) MOC.

Figure 4.16. Mach number contours; $r_{annulus}$ = 30 units and p_{exit}/p_{∞} = 20; (a) CFD with one-equation turbulence model and (b) MOC result.

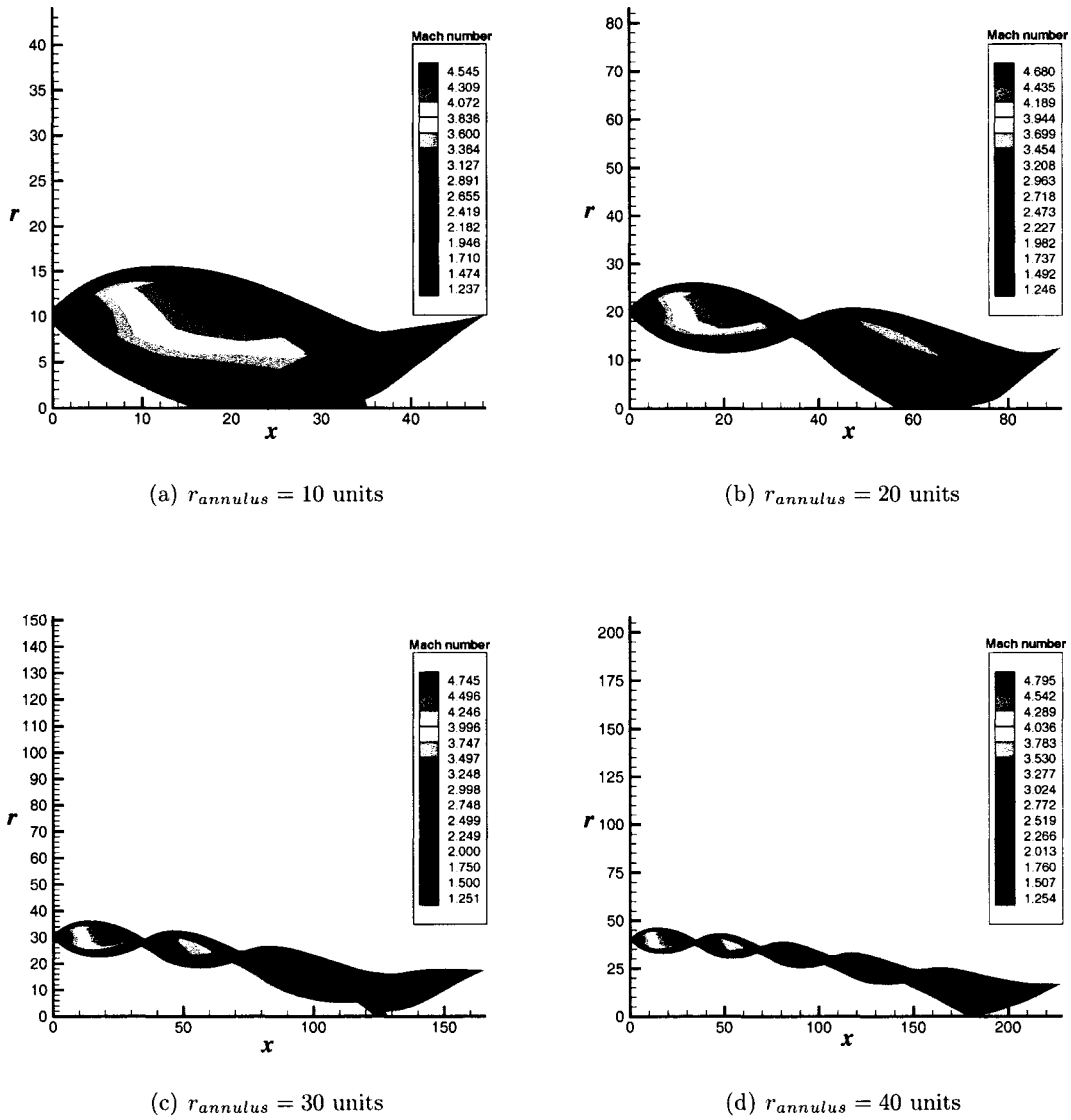

(a) $r_{annulus} = 10$ units

(b) $r_{annulus} = 20$ units

(c) $r_{annulus} = 30$ units

(d) $r_{annulus} = 40$ units

Figure 4.17. Mach number contours for $p_{exit}/p_{\infty} = 10$; (a) $r_{annulus} = 10$ units, (b) $r_{annulus} = 20$ units, (c) $r_{annulus} = 30$ units, and (d) $r_{annulus} = 40$ units.

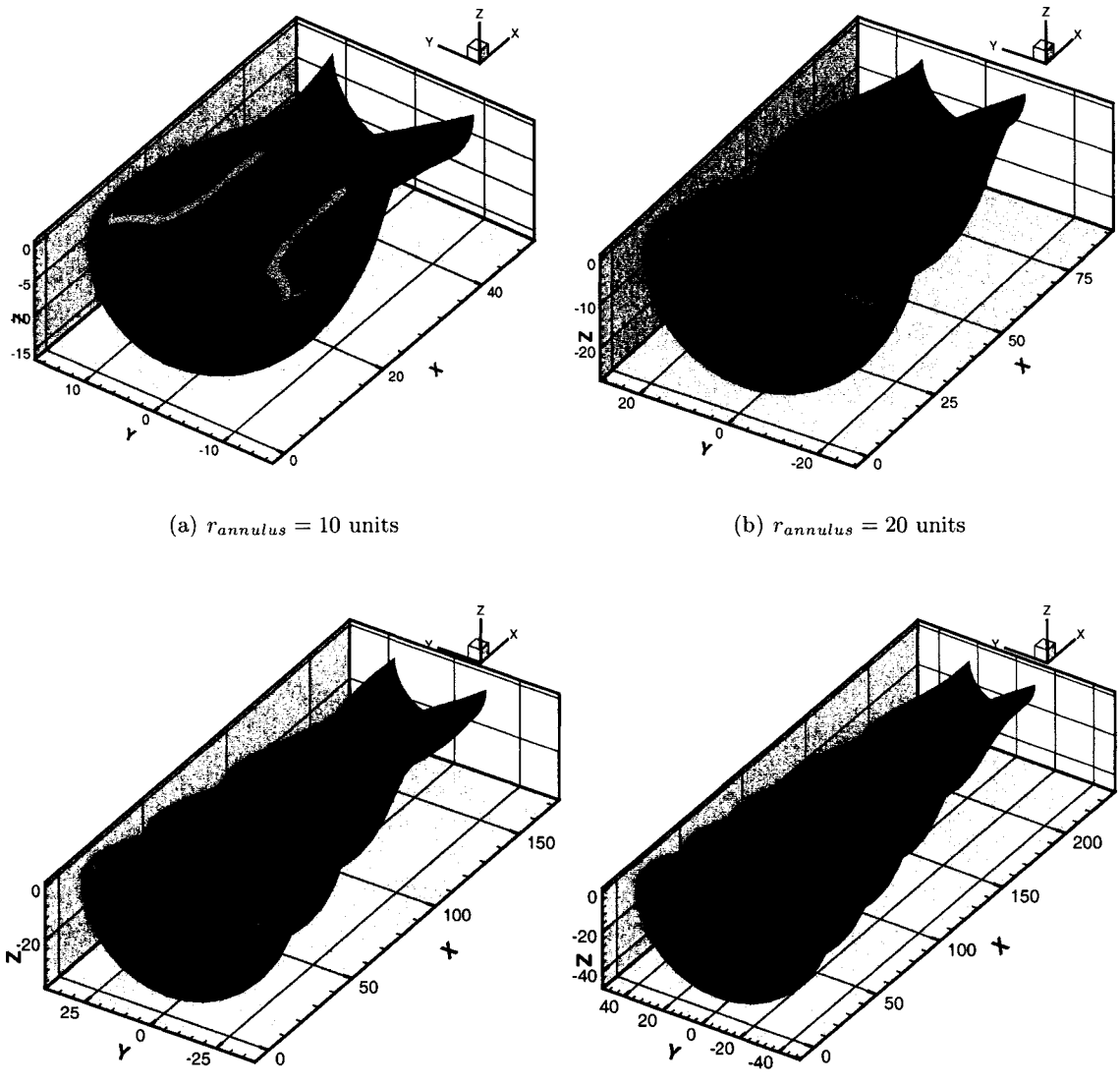

(a) $r_{annulus} = 10$ units

(b) $r_{annulus} = 20$ units

(c) $r_{annulus} = 30$ units

(d) $r_{annulus} = 40$ units

Figure 4.18. Three dimensional Mach number contours for $p_{exit}/p_{\infty} = 10$; (a) $r_{annulus} = 10$ units, (b) $r_{annulus} = 20$ units, (c) $r_{annulus} = 30$ units, and (d) $r_{annulus} = 40$ units.

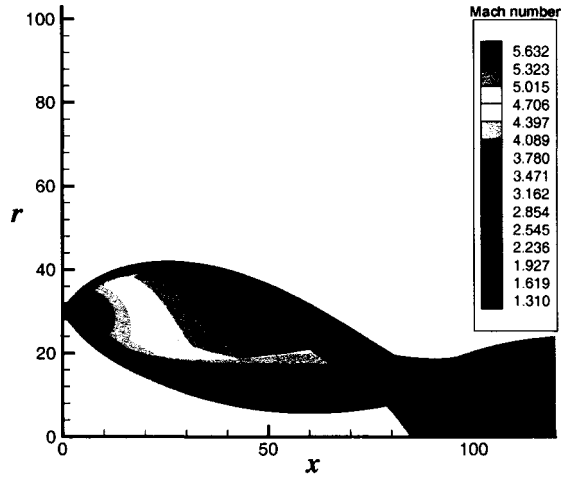

(a) $r_{annulus} = 20$ units

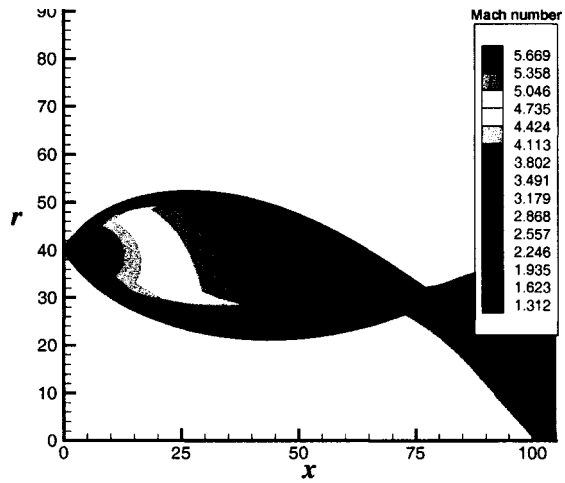

(b) $r_{annulus} = 30$ units

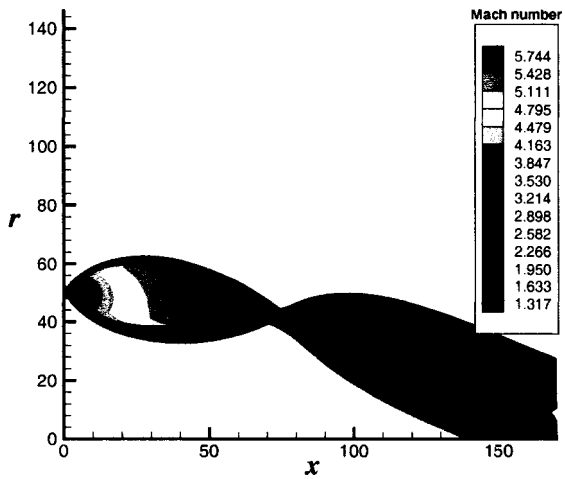

(c) $r_{annulus} = 40$ units

Figure 4.19. Mach number contours for $p_{exit}/p_{\infty} = 20$; (a) $r_{annulus} = 30$ units, (b) $r_{annulus} = 40$ units, and (c) $r_{annulus} = 50$ units.

4.4.2. MOC Predictions for Three Different Gases

Figures 4.20, 4.21 present the jet configurations of various gases computed by the MOC. The gases considered in this section are acetone, methane, and nitrogen. The specific heat ratios of acetone, methane, and nitrogen are approximately 1.1, 1.3, and 1.4, respectively. The nozzle-exit-to-ambient static pressure ratio is 10 and the radius of annulus is 30 units for all gases in these comparisons.

As the specific heat ratio of the gas becomes smaller, the jet configuration becomes thicker and the jet meets the axis earlier. Also, the flow expands more at the core region of the gas jet for larger specific heat ratio. In Fig. 4.21, the maximum Mach numbers of acetone, methane, and nitrogen are 3.637, 4.507, and 4.995, respectively. For all gases, no Mach disc is generated in the core flow of the jet.

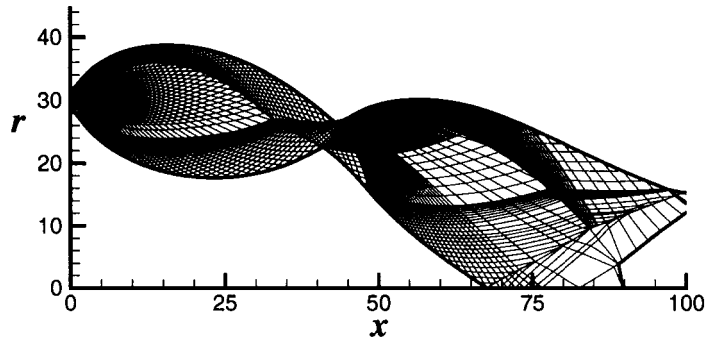

(a) Acetone, $\gamma = 1.1$

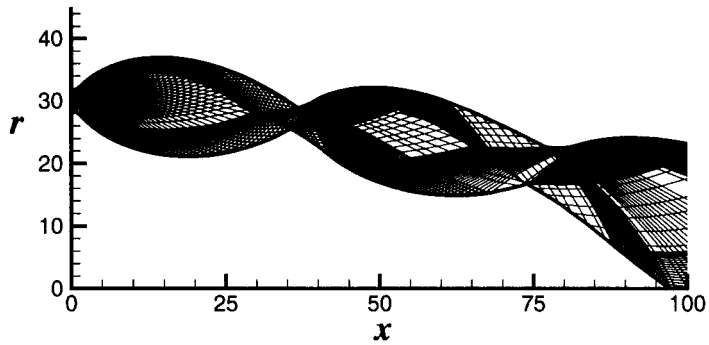

(b) Methane, $\gamma = 1.3$

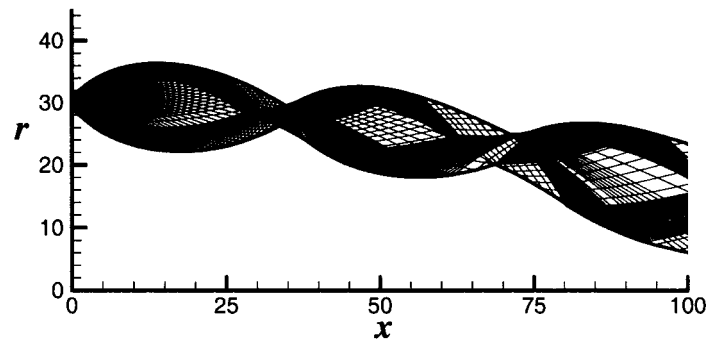

(c) Nitrogen, $\gamma = 1.4$

Figure 4.20. Characteristic net; $r_{annulus} = 30$ units and $p_{exit}/p_{\infty} = 10$; (a) Acetone, $\gamma = 1.1$, (b) Methane, $\gamma = 1.3$, and (c) Nitrogen, $\gamma = 1.4$.

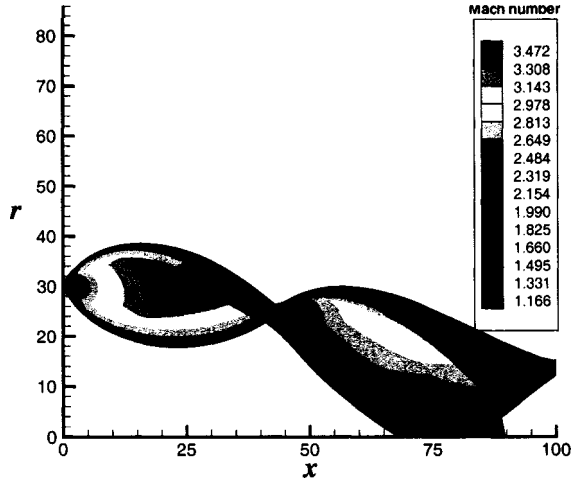

(a) Acetone, $\gamma = 1.1$

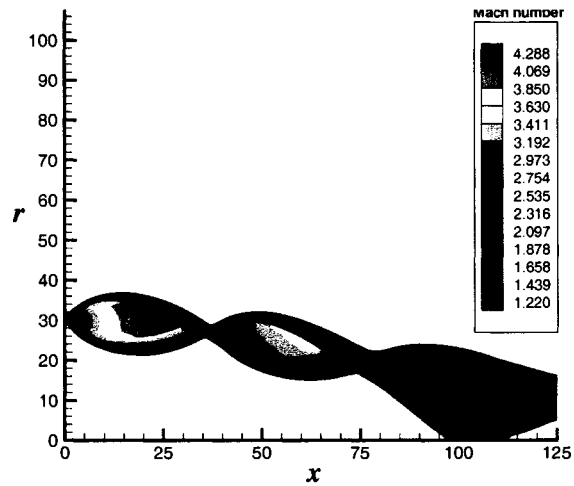

(b) Methane, $\gamma = 1.3$

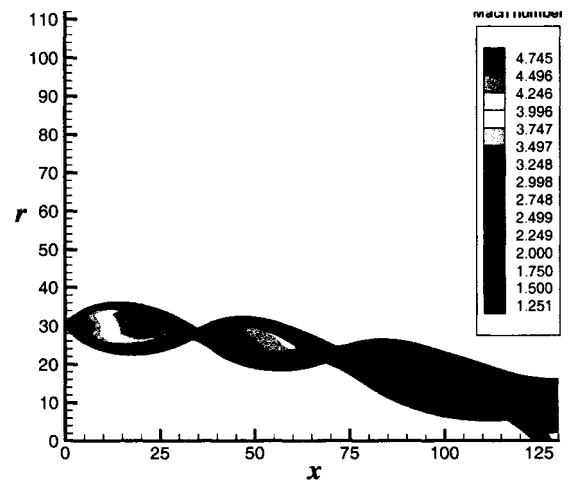

(c) Nitrogen, $\gamma = 1.4$

Figure 4.21. Mach number contours; $r_{annulus} = 30$ units and $p_{exit}/p_{\infty} = 10$; (a) Acetone, $\gamma = 1.1$, (b) Methane, $\gamma = 1.3$, and (c) Nitrogen, $\gamma = 1.4$.

Chapter 5

Nozzle Design and Validation

5.1. Design Consideration

The performance of large bore natural gas engines can be enhanced if the injected fuel is well mixed with the air inside the cylinder. Because of this, it is important to know the factors for improving mixing. The factors affecting mixing are injection pressure, actuation mechanism, valve lift profile, nozzle design, piston shape, scavenging system design, and compression ratio. We are working on more fully understanding the significance of the poppet valve, the nozzle and the shape of the piston top in controlling the mixing of the injection fuel with the air in the cylinder.

When fuel is injected at high pressure (3.0 MPa) in a natural gas engine using a poppet valve, the resulting fuel jet can have significantly more momentum and kinetic energy than in conventional low pressure (0.3 MPa) injection system. It is hypothesized that the impact of the high pressure jet with the piston top creates both large scale mixing and vigorous small scale turbulent structures. As a consequence, the fuel-air mixing inside the cylinder of large bore engines may be enhanced. For high pressure injection, shrouds have been employed around the poppet valve to direct the jet into the center of the cylinder and onto the piston surface. However, these shrouds cause a significant loss of stagnation pressure because they are not carefully designed to accelerate the flow to the supersonic velocities isentropically. Both oblique shock waves and flow separation may occur, resulting in substantial flow losses.

The objective of this work was to replace the simple shroud with an efficient fuel injection nozzle designed to improve performance and reduce flow losses. It is imperative to design

such a nozzle carefully to maximize the kinetic energy and momentum of the injected fuel, to minimize the stagnation pressure loss, and to maintain the required mass flow rate. To attain these objectives, some of the considerable available experience from aerospace nozzle design was applied. Three types of nozzles were designed: a convergent-divergent nozzle, a conical nozzle, and an Aerospike (external expansion plug) nozzle. The divergent sections of the convergent-divergent nozzle and Aerospike nozzle were designed using the method of characteristics. The divergent section of the conical nozzle was designed for three different spreading half angles (15°, 30°, and 45°) using the assumption of simple one dimensional compressible flow.

Computational Fluid Dynamics (CFD) was utilized as an evaluation tool. Designs were modeled using CFD to evaluate critical jet parameters and to determine if any shock wave or recirculation zones occurred. The designs were compared against the nominal industrial Hoerbiger design with the poppet retainer geometry.

5.2. Fuel Valve Nozzle Design

Two existing valve designs for high pressure injection were considered in this work. The first was a simple poppet valve with a straight shroud (parallel to the jet axis) added. The second design was similar except that the shroud converged toward the axis. The intent of this second design was to prevent the accidental incursion of the poppet into the cylinder. We will refer to this as the poppet with retainer. Three types of nozzles were newly designed for comparison with the two existing shrouds: a convergent-divergent nozzle, a conical nozzle and an Aerospike (external expansion plug) nozzle.

5.2.1. Nominal Nozzle DesignsStreamlines and Mach number contour of straight shrouded nozzle.

When fuel is injected at low pressure without a shroud, the fuel jet around the poppet valve collapses downstream of the poppet valve. For high pressure injection without a shroud, the fuel jet does not collapse, but flows along the cylinder wall, producing poor mixing with air in the cylinder. To attain satisfactory mixing for high pressure injection, shrouds must

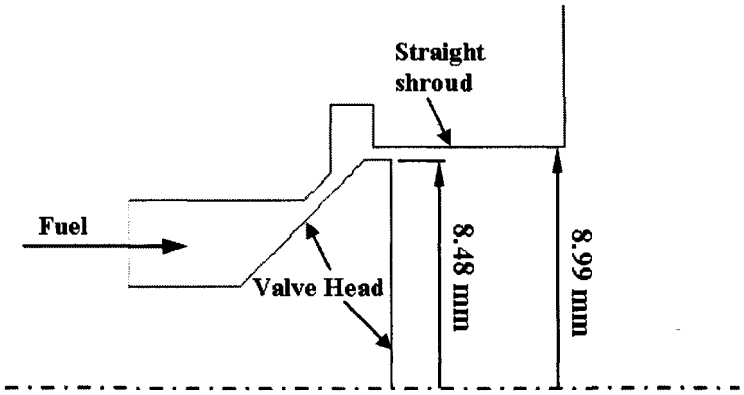

Figure 5.1. Straight shrouded nozzle.

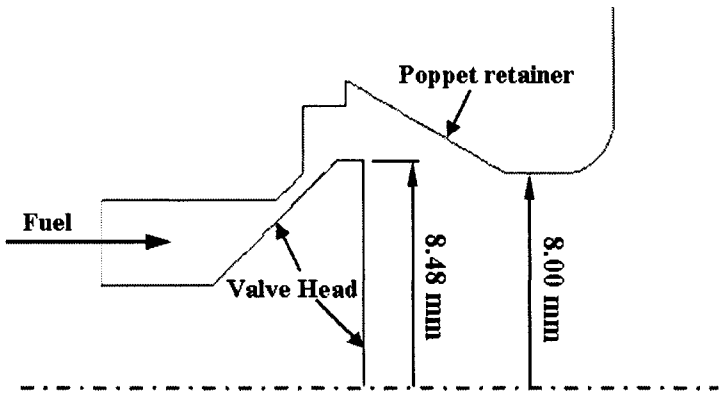

Figure 5.2. Shrouded nozzle with poppet retainer.

be employed around the poppet valve to direct the fuel jet into the center of the cylinder. The Hoerbiger company designed two types of nozzles. One is the straight shrouded nozzle and the other is the shrouded nozzle with poppet retainer. Figure 5.1 shows the straight shrouded nozzle. In Fig. 5.2, the poppet retainer was devised to prevent a broken valve head from entering the cylinder and causing damage to the engine. Theses designs are used as a bench mark for comparison of new designs.

5.2.2. Aerospike Nozzle

Figure 5.3 shows the Aerospike nozzle configuration. The centerbody curvature of the Aerospike nozzle was designed using the method of characteristics so that the minimal

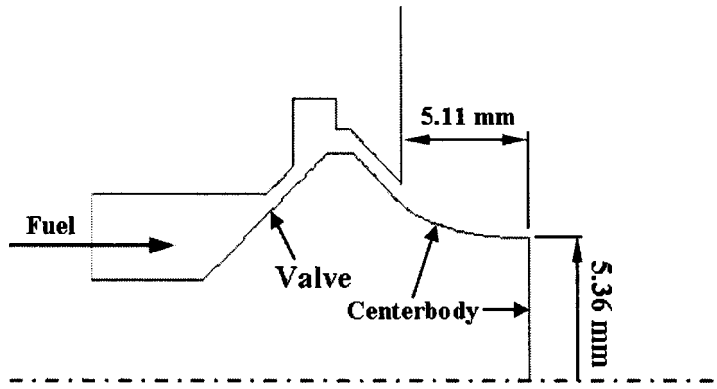

Figure 5.3. Aerospike nozzle.

reflection of the expansion waves emanating from the lip would occur. The most ideal shape of the centerbody is a pointed spike shape, which allows the issuing gases expand through an isentropic process. In so doing, the nozzle efficiency is maximized and no energy is lost from turbulent mixing in the flow. However, the pointed spike tends to be prohibitively long and heavy. The length of a spike nozzle centerbody can be reduced by replacing the pointed spike with a flat base, which is known as a truncated spike. Theoretical studies have shown that the truncation of the pointed spike results in very little performance loss. Since the Aerospike nozzle has an altitude (pressure) compensation capability for rocket propulsion, the Aerospike nozzle is also believed to operate efficiently in off-design conditions of an engine cylinder.

5.2.3. Convergent-divergent Nozzle

The convergent section and throat region define the subsonic and transonic flow inside the nozzle. The convergent section was designed to minimize the stagnation pressure loss in the subsonic region and to avoid flow separation near the throat region. A gradual decrease of area is preferred for this purpose, however, the total length of the nozzle is restricted by the distance between the tip of the poppet valve and the piston top.

The geometry of a nozzle throat is completely defined by specifying the value of the dimensional ratio ρ_t/y_t (nozzle throat upstream radius of curvature/nozzle throat radius). The sonic line location approaches the geometrical throat as the value of the ratio ρ_t/y_t

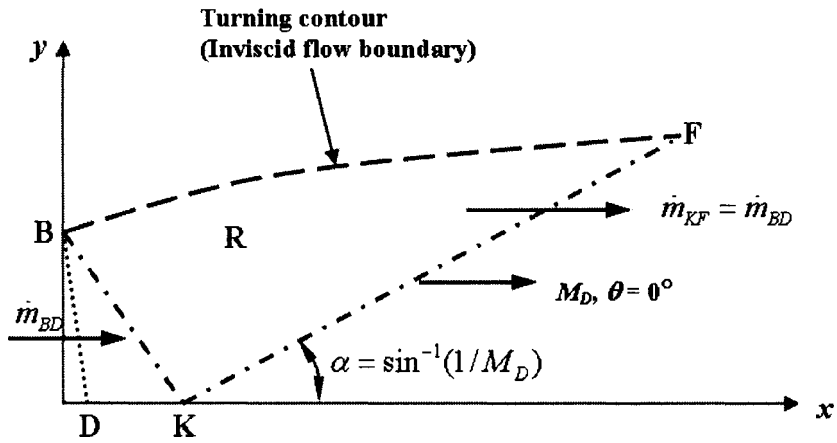

Figure 5.4. Determination of the turning contour of a nozzle.

increases. The velocity profiles for the larger values of ρ_t/y_t tend to approach that of a one-dimensional flow. The sonic lines for values of ρ_t/y_t, approximately, are highly distorted, indicating that the corresponding flows deviate significantly from one-dimensional flow. For values of $\rho_t/y_t > 2$, the flow tends to approach a uniform flow.

The divergent section of the nozzle was designed using the axi-symmetric method of characteristics. It is necessary that the exit flow field from the nozzle be a parallel uniform flow with $M = M_D$ and $\theta = 0°$. In that region, all of the characteristics must be straight lines at the angle $\alpha_D = \arcsin(1/M_D)$, as illustrated in Fig. 5.4. Thus, a straight characteristic making the angle α_D with the x- axis is extended from point K into the downstream flow field to the point F; the mass flow rate crossing line KF must equal the known mass flow rate crossing the initial-value line BD. Figure 5.4 illustrates schematically the resulting conditions. The remaining problem is that of determining the flow field inside of the turning region R, and the required shape for the turning contour of the wall, denoted by BF. This is an initial-value problem, with data specified on two characteristics of opposite families. Each new wall point is located by performing a mass balance along the corresponding characteristic from the initial point on line KF; the procedure is repeated at successive points along line KF until the entire turning contour BF has been determined. The designed convergent-divergent nozzle contour is shown in Fig. 5.8.

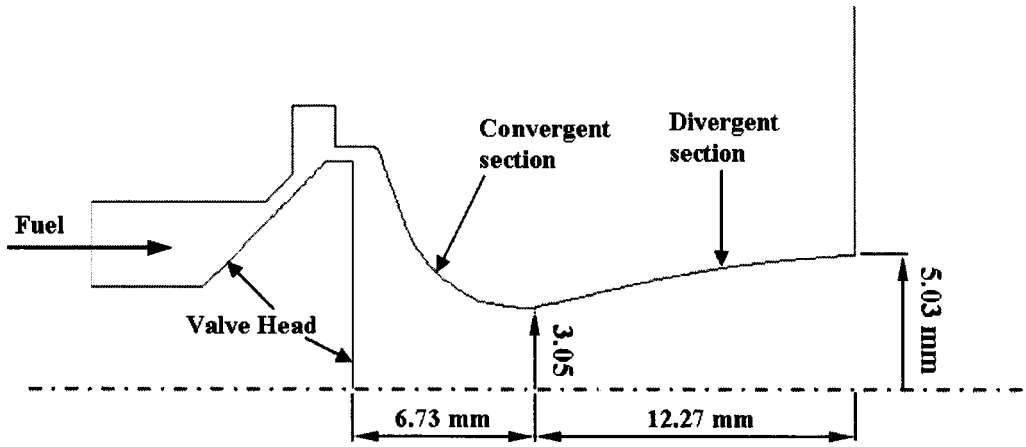

Figure 5.5. Convergent-divergent nozzle.

5.2.4. Conical Nozzle

The design of the convergent section and throat region of a conical nozzle is similar to that of a convergent-divergent nozzle. The design of the divergent sections of the conical nozzles were based on the assumption of simple one dimensional compressible flow. The two parameters considered in the design of the divergent section of conical nozzles are the spreading half angle of divergent wall and the area ratio of the throat area to the planar nozzle exit area. The area ratio is determined by the pressure ratio. The first conical nozzle was designed with a 15° half angle as its divergent section. Conical nozzles with half angles of 30° and 45° degrees in the divergent section were also designed to compare the mixing performance. Figure 5.6 shows a conical nozzle with 15° spreading half angle.

5.3. Fuel Valve Nozzle Evaluation

5.3.1. Computations

The injection pressure and cylinder pressure is varying during the fuel injection because of the piston motion and valve events. The fuel is injected into cylinder pressure of 0.12 MPa at 3.1 MPa at the start of injection (SOI) and into cylinder pressure of 0.17 MPa at 2.9 MPa at the end of injection (EOI). The on-design injection pressure and cylinder pressure

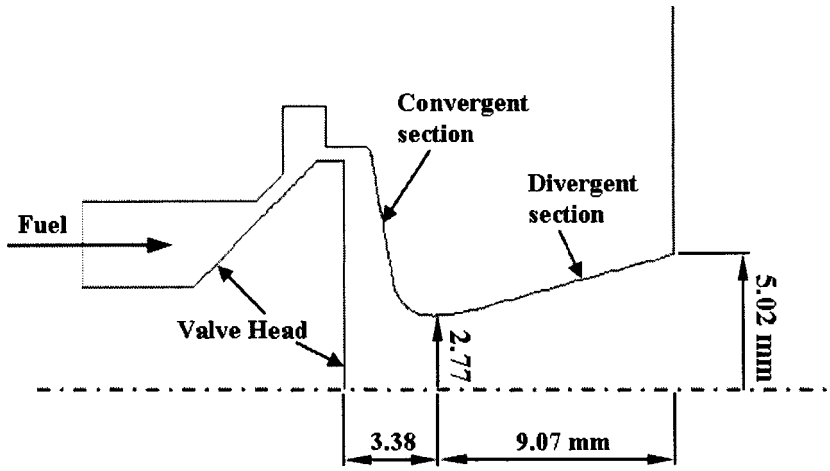

Figure 5.6. Conical nozzle with a spreading half angle of 15°.

were chosen as 3.0 MPa and 0.14 MPa respectively. The computations were done for the following three boundary conditions: On-design condition, SOI, EOI.

The standard $k-\varepsilon$ model was used for the viscous model and the SIMPLE algorithm was used for pressure-velocity coupling. The second order discretization scheme was used for the pressure and density and the power law was used for the other properties. The steady state solutions for each nozzle were obtained in the case for the open cylinder. The grid for the convergent-divergent nozzle is shown in Fig. 5.7.

5.3.2. Stagnation Pressure, Sonic Surface, and Mass Flow Rate

The ratio of the injection stagnation pressure to the back pressure (the pressure in the cylinder) and the exit Mach number are important elements for nozzle design. Usually the stagnation pressure loss in subsonic region is not considered for nozzle design because it is believed that the flow is nearly isentropic through the nozzle. However, for the fuel valve nozzle a complicated flow is formed as fuel passes through the valve. The injection stagnation pressure is decreased by up to 30 % in this process and this loss must be considered in designing the nozzle.

It is important to know the correct mass flow rate required for the fuel valve nozzle. The mass flow rate is determined by the sonic surface area, the fuel density at sonic surface and

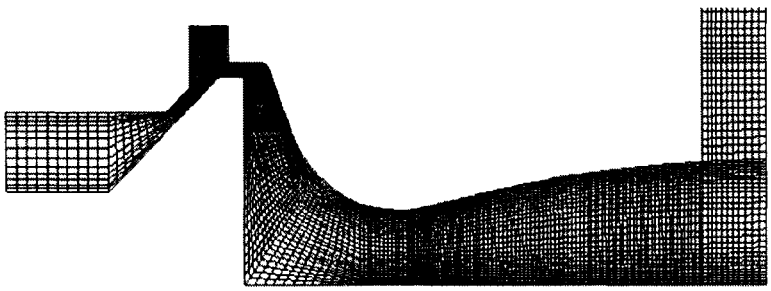

(a) Grid near the nozzle exit.

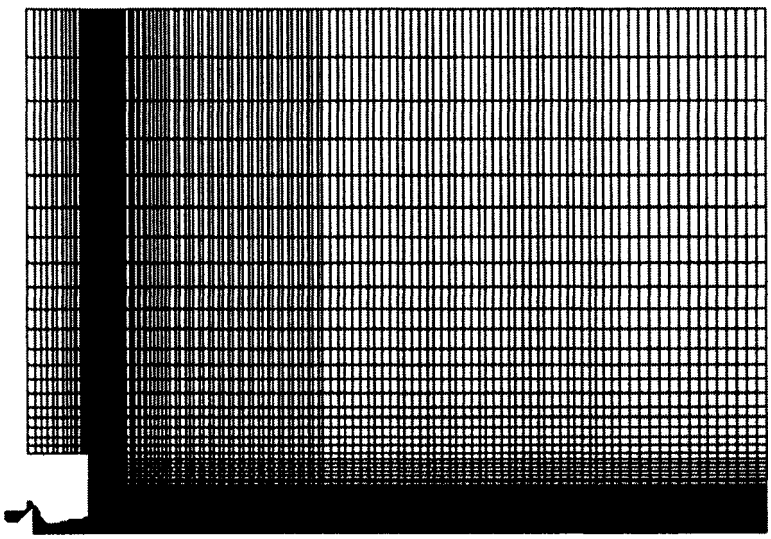

(b) Overall view of the grid.

Figure 5.7. Grid for the convergent-divergent nozzle.

sonic speed. If we assume the fuel, methane, behaves as ideal gas that has specific heat ratio of 1.3, the sonic speed is the function of stagnation temperature and the fuel density at the sonic surface is the function of stagnation temperature and stagnation pressure. Because the stagnation temperature is almost constant overall region, the sonic speed is constant and the fuel density at the sonic surface is a function of stagnation pressure only. These relations are shown in Equations (5.1) to (5.3). The mass flow rate is, therefore, decided by the sonic surface area and the stagnation pressure at sonic surface when the stagnation temperature is fixed.

$$\rho^* = \rho_0 \left(\frac{2}{\gamma+1}\right)^{1/(\gamma-1)} = \frac{p_0}{T_0}\frac{MW}{R_u}\left(\frac{2}{\gamma+1}\right)^{1/(\gamma-1)} \tag{5.1}$$

$$a^* = a_0\sqrt{\frac{2}{\gamma+1}} = \sqrt{\gamma\frac{R_u}{MW}T_0}\sqrt{\frac{2}{\gamma+1}} \tag{5.2}$$

$$\dot{m} = \rho^* a^* A_{sonic} = \frac{p_0}{T_0}\sqrt{\frac{\gamma MW}{R_u}}\left(\frac{2}{\gamma+1}\right)^{(\gamma+1)/2(\gamma-1)} A_{sonic} \tag{5.3}$$

Choking does not always occur where the geometric passage area becomes smallest because the stagnation pressure decreases as the gas flows downstream. In order to explain this phenomenon the convergent-divergent nozzle is considered in Fig. 5.8. Section 1 is the minimum passage area region and Section 2 is the nozzle throat region. If flow is choked at both sections, the mass flow rate of the both sections is governed by the Eq. 5.3. From the Eq. 5.3, we know that the mass flow rate is proportional to the product of the local stagnation pressure and sonic surface area when the stagnation temperature is constant (Eq. 5.4). The mass flow rates of both section are equal to each other (Eq. 5.5). Therefore, the area ratio could be expressed as the local stagnation pressure ratio in Eq. (5.7).

$$\dot{m}\ p_0 A^* \tag{5.4}$$

$$\dot{m}_1 = \dot{m}_2 \tag{5.5}$$

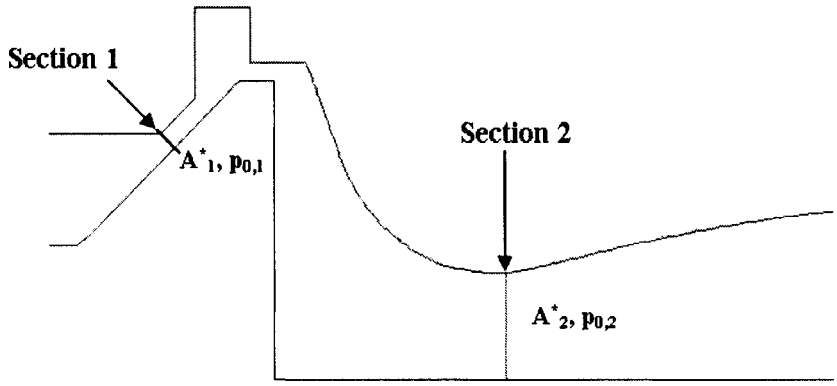

Figure 5.8. Convergent-divergent nozzle.

$$p_{0,1}A_1^* = p_{0,2}A_2^* \tag{5.6}$$

$$\frac{A_1^*}{A_2^*} = \frac{p_{0,1}}{p_{0,2}} \tag{5.7}$$

Because the stagnation pressure at Section 1 is larger than the stagnation pressure at Section 2, the sonic surface area of Section 2 is greater than the sonic surface area of Section 1. If we increase the nozzle throat area, choking occurs only at Section 1 and if we decrease the nozzle throat area, choking occurs only at Section 2.

For the convergent-divergent nozzle, it is necessary to make the throat area bigger than the upstream minimum passage area to compensate for the stagnation pressure loss and eventually to get the required mass flow rate. The convergent section of the nozzle should be designed to minimize the stagnation pressure loss and to avoid flow separation near the throat. If the flow is separated in the vicinity of the throat, the flow passage area, which is sonic surface area, decreases and the mass flow rate decreases.

The sonic surface and stagnation pressure of each nozzle are shown in Fig. 5.9. The shrouded nozzle with poppet retainer has the highest stagnation pressure because choking

occurs further upstream than for the other nozzles. This nozzle also has the largest mass flow rate.

5.3.3. Comparison Parameters for the Nozzle Performance

The nozzles were designed to minimize the stagnation pressure loss and to maximize the axial momentum and kinetic energy of the jet. The axial momentum and kinetic energy of the jet were considered as the comparison of the nozzle performance. After the jet is fully expanded, the axial momentum is nearly constant because no additional force acts on the jet. However, the kinetic energy decreases continuously as the jet travels downstream due to mixing and viscous dissipation. Because the mass flow rate of each nozzle is different, the axial momentum and kinetic energy are divided by the fuel mass to get the parameters independent of the mass flow rate. The comparison parameters are defined in Eqs. (5.8) and (5.9).

average axial momentum per unit fuel mass

$$\overline{V}_x = \frac{\int_0^{edge} V_x d\dot{m}}{\dot{m}_{fuel}} \tag{5.8}$$

average kinetic energy per unit fuel mass

$$\overline{\left(\frac{V^2}{2}\right)} = \frac{\int_0^{edge} (V^2/2)\, d\dot{m}}{\dot{m}_{fuel}} \tag{5.9}$$

The axial momentum and kinetic energy were integrated at every inch from the cylinder upper wall, as shown in Fig. 5.10.

5.3.4. Straight Shrouded Nozzle

The Mach number and streamline contours for the straight shrouded nozzle are presented in Fig. 5.11. The sonic surface is located between the rim of the valve head and the shroud. The geometric minimum area for the valve is located upstream of this point, at the valve seat. Significant stagnation pressure losses occur between the seat and the sonic surface. Downstream of the sonic surface, the jet becomes supersonic as the jet expands. In Fig. 5.11, the increase in the cross sectional area of the stream tube defining the jet is

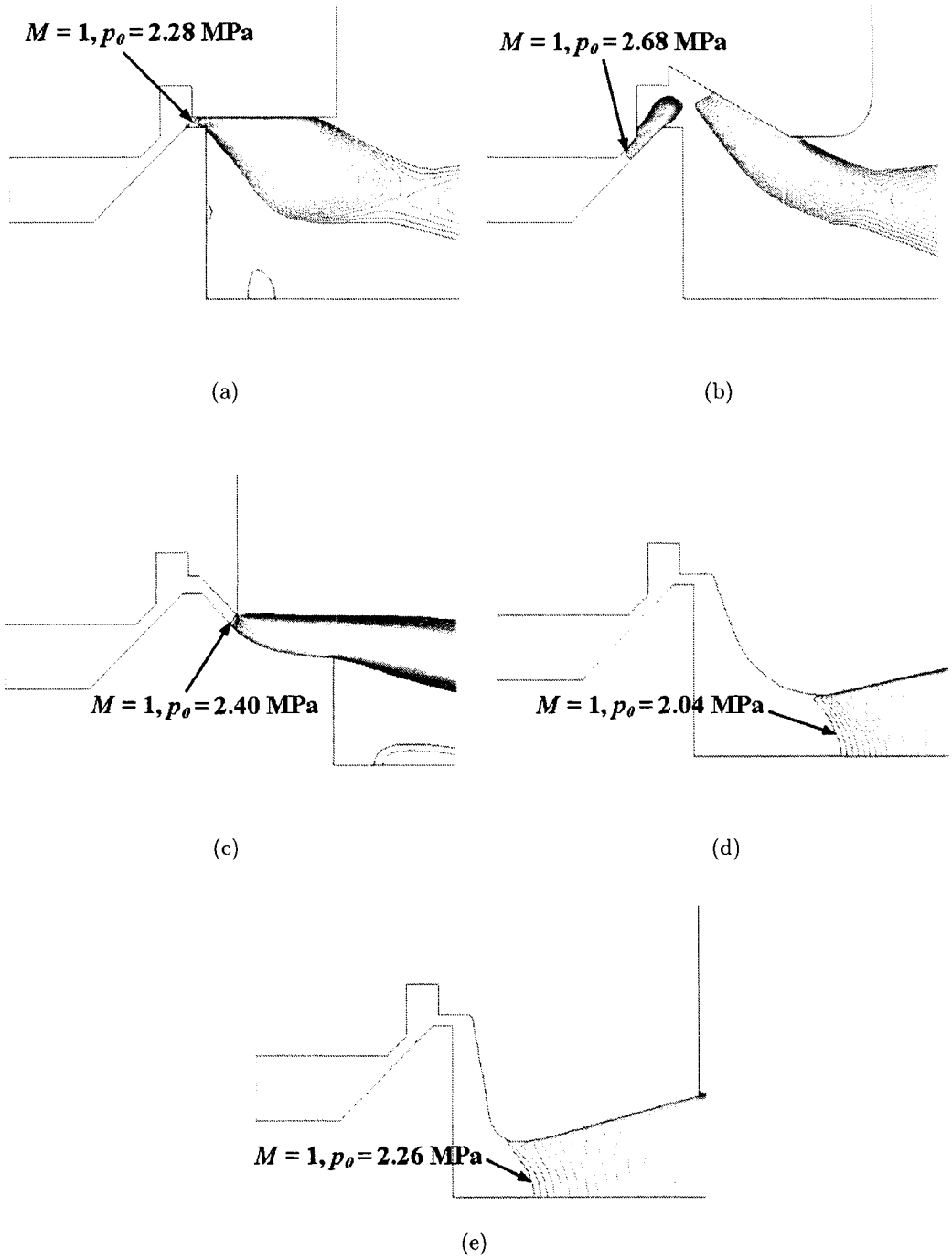

Figure 5.9. Mach number contours, showing the region where the flow is choked; (a) straight shrouded nozzle, (b) shrouded nozzle with poppet retainer, (c) aerospike nozzle, (d) convergent-divergent nozzle, and (e) conical nozzle.

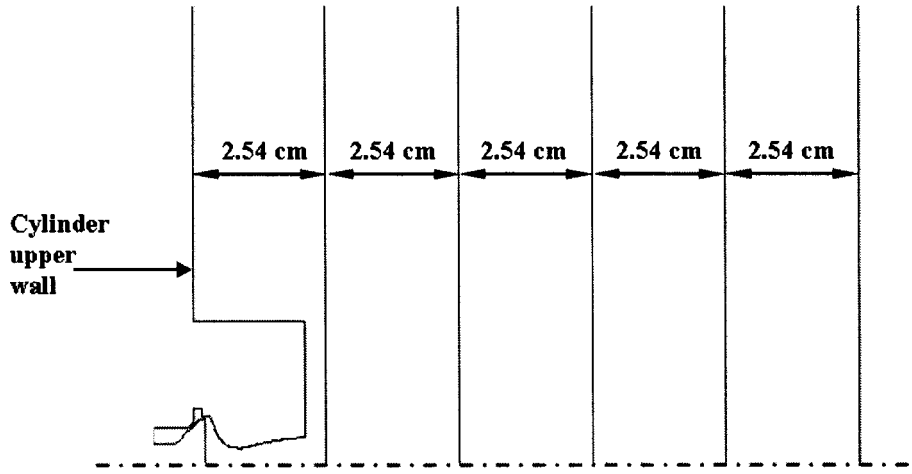

Figure 5.10. Locations of the integration of the axial momentum and kinetic energy.

apparent. This expansion and the associated decrease in static pressure continue until, in Region A in Fig. 5.11, the pressure is less than the cylinder pressure. That is, the jet is overexpanded . The required re-compression to cylinder pressure is effected through a shock structure that extends into the body of the jet from a separation point located on the shroud wall. Continuous compression waves also extend from the lower boundary of the jet. The compression occurring between points B and C eventually leads to a core flow in the jet at a nearly uniform pressure that is higher than the cylinder pressure. A consequent narrowing of the stream tube downstream of C can also be identified. At this point in the expansion process the jet has an annular rather than circular cross section. During this expansion and re-compression process there are gradual losses of the stagnation pressure by mixing in the compression region and significant losses across the shock wave.

5.3.5. Shrouded Nozzle with Poppet Retainer

The Mach number and streamline contours of the shrouded nozzle with poppet retainer are shown in Fig. 5.12. The flow is choked at the minimum geometric area in the valve seat region and accelerates downstream to form a supersonic jet as the flow area increases. The supersonic flow region terminates in a strong shock caused by the sudden change in flow direction required by the poppet retainer wall. After the shock, the flow becomes subsonic

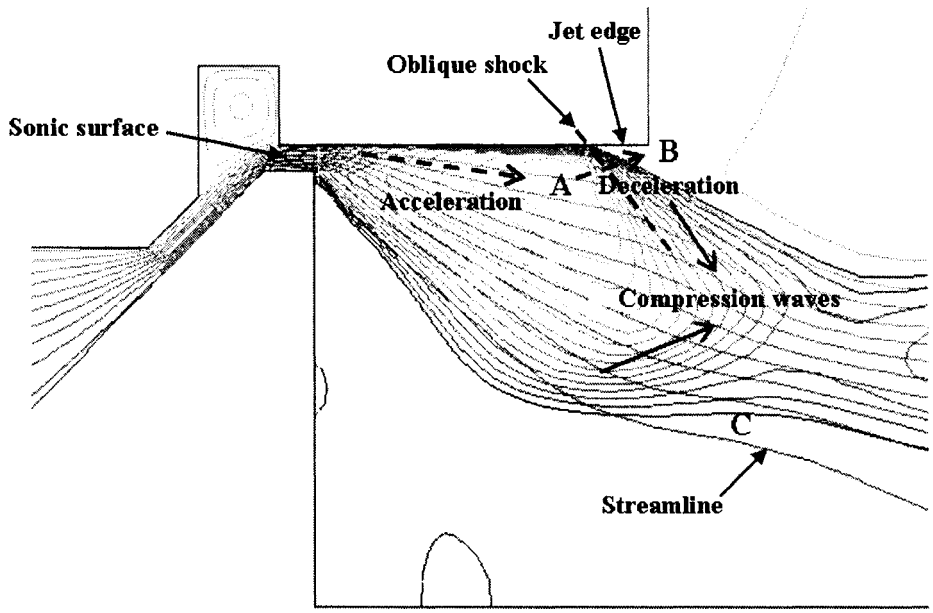

Figure 5.11. Streamline and Mach number contour of straight shrouded nozzle flow.

and bends toward the axis following the poppet retainer wall. This causes a decrease in the streamtube flow area and the subsonic jet accelerates until it passes through a second sonic surface. The flow then becomes supersonic again and accelerates as the streamtube area increases. The flow is accelerated around the corner A in Fig. 5.12 through an expansion fan emanating from the corner. As a result the jet along the wall is seriously overexpanded, a shock wave forms at the wall in order to compress the gas to cylinder pressure, and the flow separates from the wall. Compression waves from the lower jet boundary also occur and aid in producing a downstream core flow that is underexpanded. Once again the jet cross section leaving the valve is essentially annular. The complicated flow through this valve includes two shocks, a non-uniform jet structure and strong velocity gradients inside the jet. Together, these cause the largest losses in stagnation pressure of all the valves considered.

5.3.6. Aerospike Nozzle

The Mach number contours of the Aerospike nozzle is shown in Fig. 5.13. In this external expansion nozzle an expansion fan emanates from the upper lip of the cylinder wall and propagates toward the axis. The flow in the passage upstream of the lip is subsonic

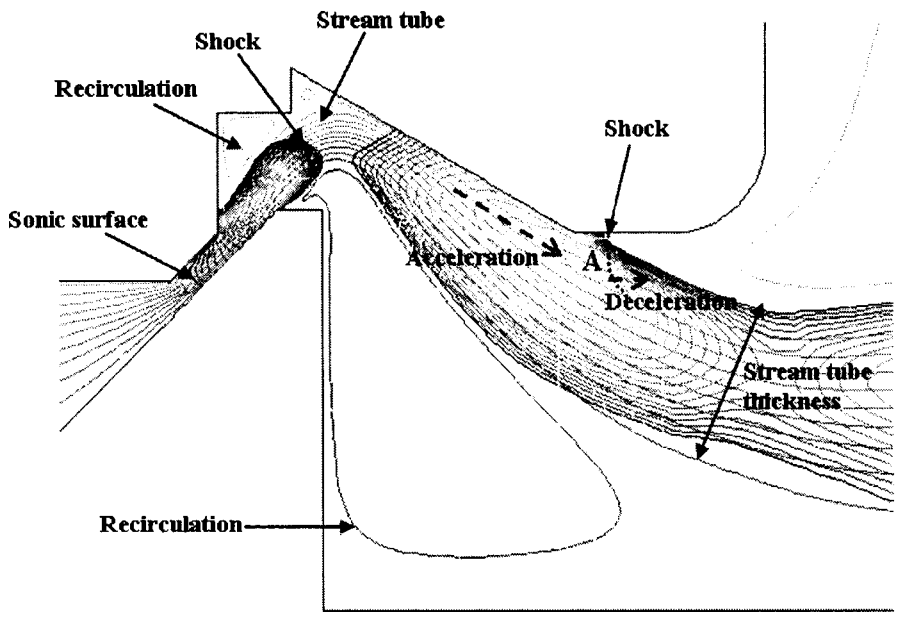

Figure 5.12. Streamline and Mach number contour of shrouded nozzle flow with poppet retainer.

and the sonic surface of the jet is approximately perpendicular to the center body of the valve at the lip location. The center body curvature downstream of the sonic surface was designed using the method of characteristics so that minimal reflection of the waves from the lip would occur. In Fig. 5.13 the core region of the jet after the initial fan can be seen to be of essentially uniform pressure and Mach number as a result of this design. Because of the plug that terminates the center body and the base recirculation flow that exists downstream of the plug, a second, much weaker, expansion fan is established at the corner of the plug and propagates downstream into the jet. As a result of the second fan the jet flow is accelerated somewhat into Region A and subsequently decelerated because of the reflection of the expansion waves as compression waves from the upper boundary of the jet. For the Aerospike design no shocks occur and the core region is quite uniform. As a consequence, stagnation pressure losses are substantially smaller than was the case for the shrouded valves. As was true for both of those designs, however, the jet for the Aerospike has an annular character. Subsequent radial expansion of the jet to the axis degrades the performance relative to the remaining valve designs (conical and convergent-divergent), which produce

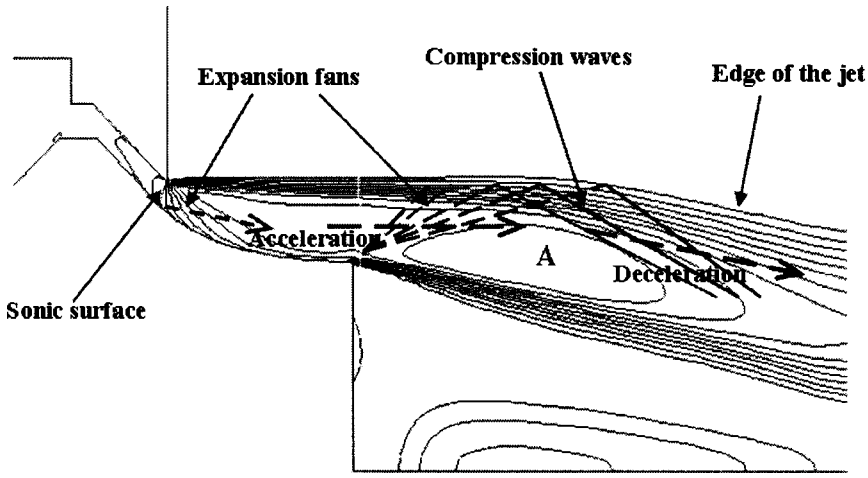

Figure 5.13. Mach number contour of Aerospike nozzle flow.

jets of circular cross section. Redesign of the Aerospike to reduce the radius of the central plug could improve its performance considerably.

5.3.7. Convergent-Divergent Nozzle

The streamline and Mach number contours of the convergent-divergent nozzle design are shown in Fig. 5.14. After the flow is choked at the throat, the flow expands continuously because the divergent nozzle shape was obtained from application of the method of characteristics. Also, the flow at the nozzle exit is essentially one-dimensional and of circular cross section. In addition the nozzle exit pressure matches closely the cylinder pressure. The boundary layer does not separate in the throat region because of careful choices for the throat radius of curvature and the convergent nozzle slope that were guided by CFD computations. Steeper convergent profiles and smaller radii of curvature result in significant separation at the throat and reduced performance. Still, with this design, a recirculation region at the base of the valve occurs and causes a stagnation pressure loss. The stagnation pressure at the sonic surface is actually predicted to be about 10 % lower for the convergent-divergent nozzle than it is for the simple conical design. Tapering the valve in the downstream direction might reduce this loss.

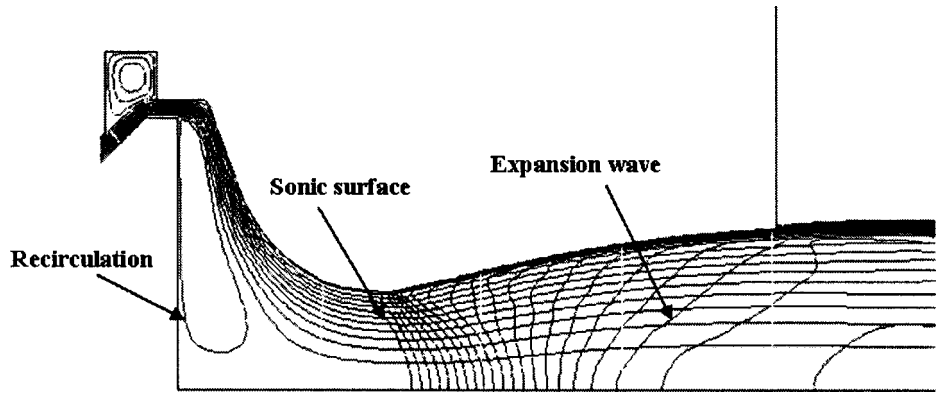

Figure 5.14. Streamlines and Mach number contours of convergent-divergent nozzle flow.

5.3.8. Conical Nozzle

Mach number contours for the conical nozzles are shown in Fig. 5.15. Expansion waves emanate from the nozzle exit and are reflected at the axis . These reflected expansion waves are, in turn, reflected as compression waves from the jet boundary. The compression waves intersect the axis and are reflected as compression waves in the 15° conical nozzle. However, in the 45° conical nozzle the compression waves coalesce to form a curved incident shock. The intensity of the incident shock increases in the downstream as it is intercepted by more compression waves. The shock curves toward the axis and eventually becomes a normal shock or Mach disk. In Fig. 5.15 (a), for the 15° nozzle, the flow is accelerated to Region A and then decelerated to Region B but maintains supersonic speed. In Fig. 5.15 (b), for the 45° nozzle, the flow is severely overexpanded in region A, a normal shock occurs and the flow becomes subsonic after the normal shock. For the conical nozzle designs considered here, a normal shock occurs for both the 30° and 45° spread angles. Figure 5.16 indicates that in terms of jet momentum the 15° conical nozzle shows the best performance among the conical nozzles.

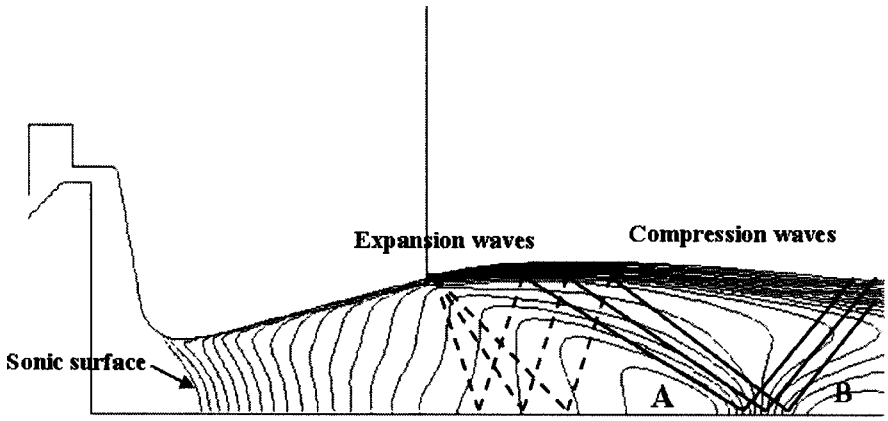

(a)

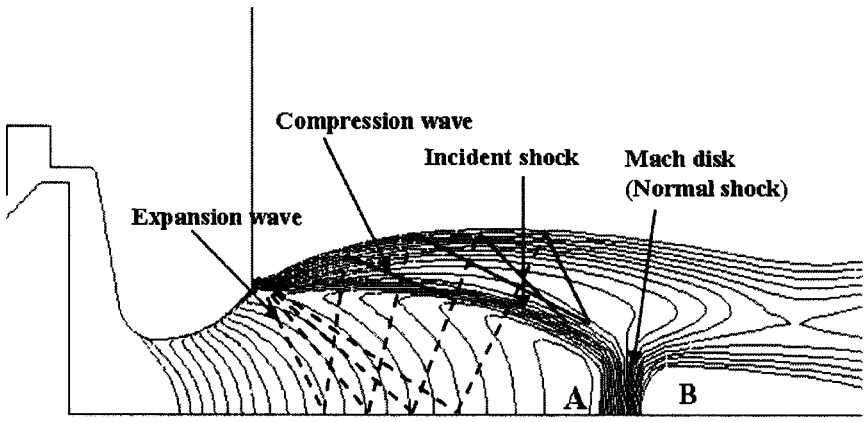

(b)

Figure 5.15. Mach number contours of conical nozzle flows; (a) 15° conical nozzle and (b) 45° conical nozzle.

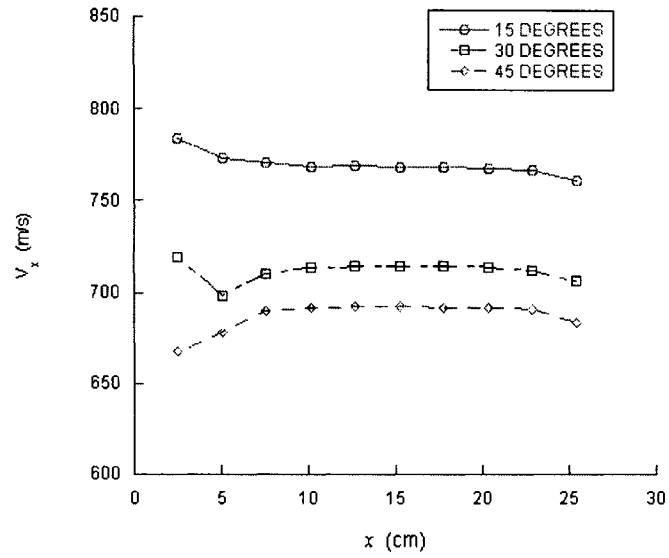

(a) Average axial momentum per unit fuel mass.

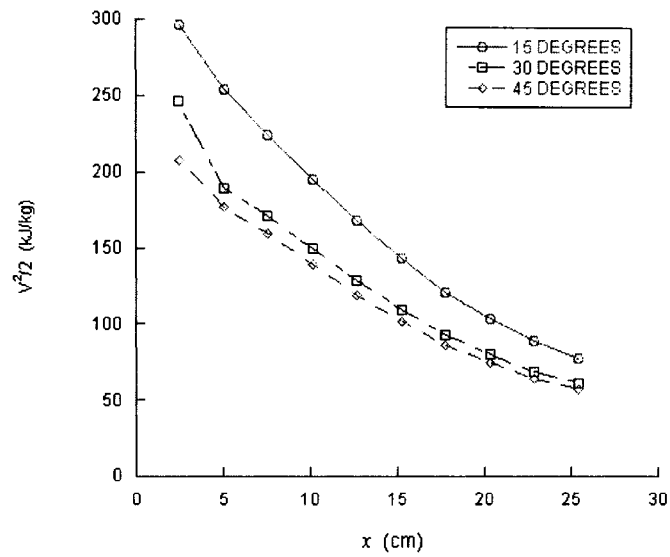

(b) Average kinetic energy per unit fuel mass.

Figure 5.16. Average parameters per unit fuel mass of three conical nozzle flows; $p_0 = 3.0$ MPa, $p_{cylinder} = 0.14$ MPa.

5.4. Comparison of the Nozzle Performance

The average axial momentum per unit fuel mass of each nozzle is shown for three different conditions in Fig. 5.17. Figure 5.17 (a) is for the design condition and Figure 5.17 (b) and (c) are for SOI and EOI respectively. The general character of all the curves is quite similar. After an initial period during which the pressure in the jet adjusts to the cylinder pressure, the mean axial momentum becomes approximately constant. This is to be expected since, once the jet pressure matches the cylinder pressure, there is no net force on the jet. It is to be remembered that the parameter being plotted is the jet axial momentum divided by the fuel mass flow, which is a constant and does not include entrained air. Thus, the average momentum per unit fuel mass is not the same as the average axial velocity. The average axial velocity decreases while the average momentum remains constant. The convergent-divergent nozzle, the conical nozzle and the shrouded valves all are initially overexpanded to some extent. Because of this, the pressure increases and the mean momentum decreases until the pressure in the jet matches the cylinder pressure. The Aerospike nozzle, on the other hand, is significantly underexpanded initially, due to the existence of the plug, and acceleration occurs until the pressures match. The value of the mean jet momentum once pressure becomes equal to the cylinder pressure is directly proportional to the mean stagnation pressure at the point where pressure equalization occurs. Thus, this mean momentum value is a direct measure of nozzle performance in terms of stagnation pressure losses, or, equivalently, entropy generation in a given valve-nozzle combination. Higher values imply better performance. For design and off-design conditions, the convergent-divergent nozzle shows the best performance, though the conical nozzle is nearly as good. The average axial momentum for the convergent-divergent nozzle is about 24 % higher than the straight shrouded valve under all conditions. The performance of the valve with retainer is even worse than the straight shrouded valve. For all nozzles mean momentum values are shifted upward about 3 % for the SOI condition relative to design and down about 3 % at EOI. Thus, all configurations are closer to being designed correctly for the SOI pressure condition rather than the nominal design condition. Computational results for the average axial momentum

Operating condition	On-design		SOI		EOI	
Comparing parameter	$\overline{V_x}$ (m/s)	%	$\overline{V_x}$ (m/s)	%	$\overline{V_x}$ (m/s)	%
Convgent-divergent nozzle	776	24.5	792	23.3	755	25.2
15° conical nozzle	768	23.3	788	22.7	745	23.5
Aerospike nozzle	737	18.3	755	17.6	716	18.7
Shrouded nozzle (bench mark)	623	0	642	0	603	0
Shrouded nozzle w/poppet retainer	607	-2.6	631	-1.7	579	-4.0

Table 5.1. Average axial momentum per unit fuel mass.

per unit fuel mass are summarized in Table 5.1, with performance evaluated relative to the straight shrouded valve.

The average kinetic energy per unit fuel mass for each nozzle is plotted in Fig. 5.18. Because of mixing with the air in the cylinder and also viscous dissipation, jet kinetic energy decreases continuously in the downstream direction, at least once the jet pressure matches the cylinder pressure. For the Aerospike nozzle sufficient acceleration occurs that the kinetic energy initially remains constant or even increases slightly until complete expansion occurs. For the other designs overexpansion ensures that the kinetic energy will always decrease The convergent-divergent nozzle has the highest kinetic energy, the conical nozzle is the next and the Aerospike is the third for average kinetic energy per unit fuel mass. The straight shrouded nozzle and shrouded nozzle with poppet retainer have a nearly identical jet kinetic energy that is substantially lower than the other designs. Initially the convergent-divergent nozzle has about 60 % more kinetic energy than the shrouded valves. This increases to about 85 % more kinetic energy at 20 cm downstream. It is clear that the three new nozzle designs all provide significantly higher performance than existing valves with shrouds.

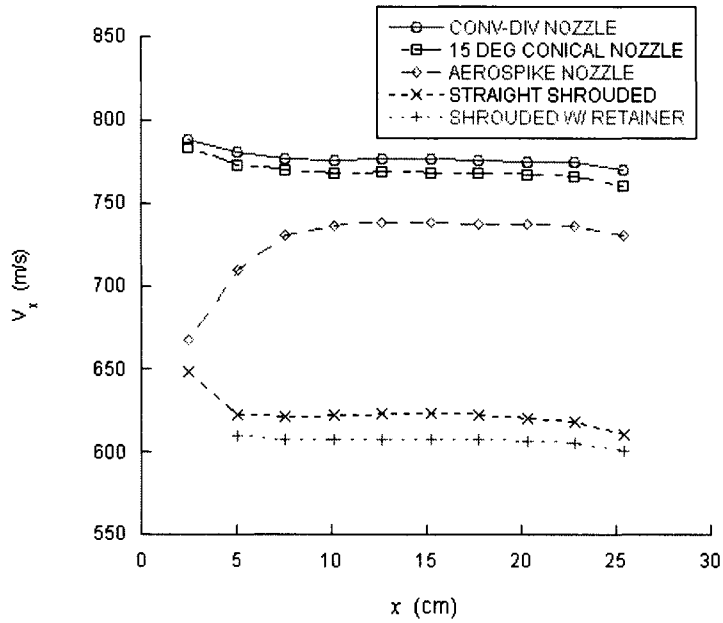

(a) On-design condition.

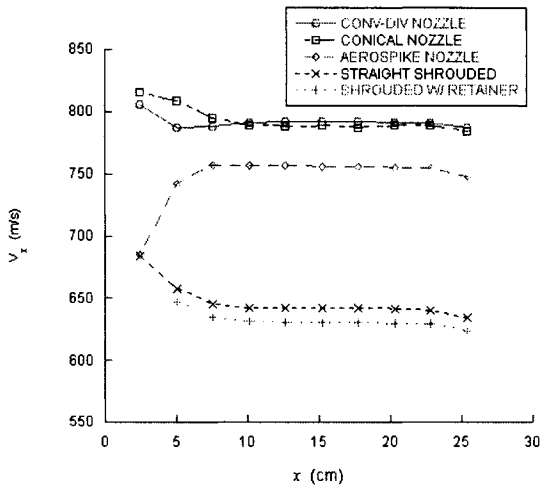

(b) Start of injection.

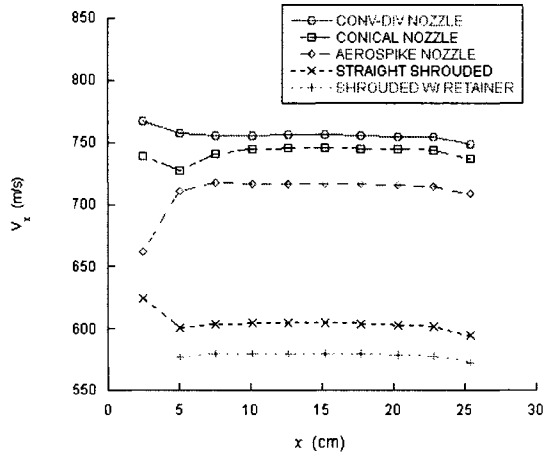

(c) End of injection.

Figure 5.17. Average axial momentum per unit fuel mass; (a) on-design condition, p_0 = 3.0 MPa, $p_{cylinder}$ = 0.14 MPa, (b) SOI, p_0 = 3.1 MPa, $p_{cylinder}$ = 0.12 MPa, and (c) EOI, $p_0$2.9 MPa, $p_{cylinder}$ = 0.17 MPa.

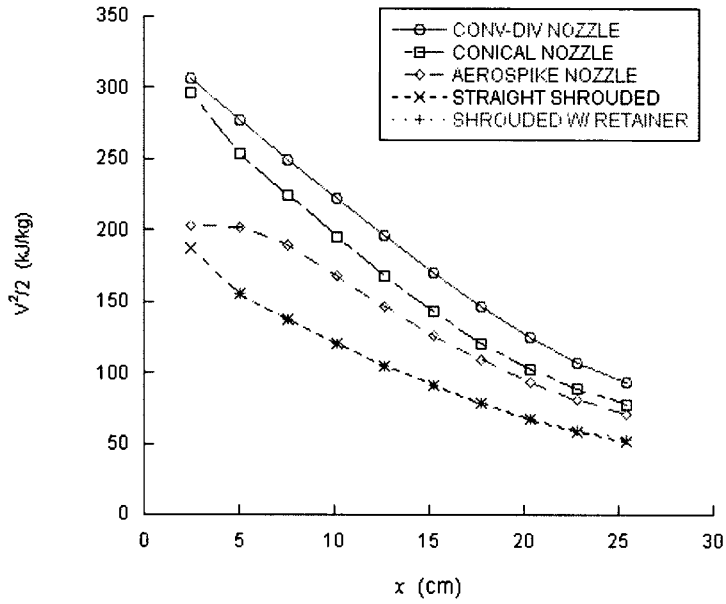

(a) On-design condition.

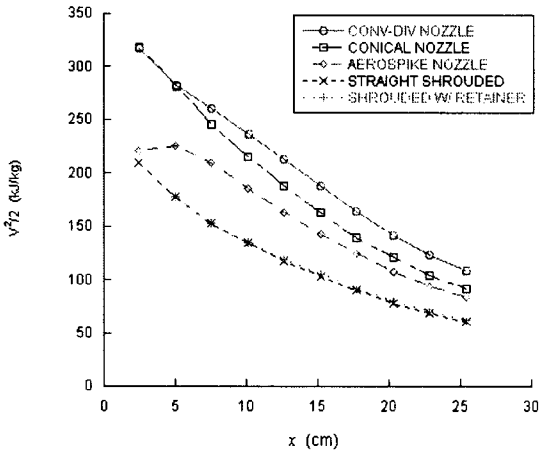

(b) Start of injection.

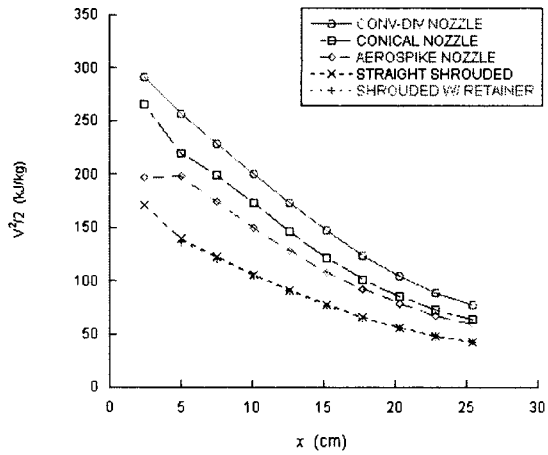

(c) End of injection.

Figure 5.18. Average kinetic energy per unit fuel mass; (a) on-design condition, p_0 = 3.0 MPa, $p_{cylinder}$ = 0.14 MPa, (b) SOI, p_0 = 3.1 MPa, $p_{cylinder}$ = 0.12 MPa, and (c) EOI, $p_0$2.9 MPa, $p_{cylinder}$ = 0.17 MPa.

Chapter 6

Conclusions

Underexpanded jet flows with axisymmetry and annular geometry were investigated using the method of characteristics (MOC) and shock-polar mapping with the assumption of inviscid rotational flow and calorically perfect gas with $\gamma = 1.4$. A consistent process for dealing with the coalescence of compression characteristic lines during the MOC computation was developed. The MOC predictions are compared to CFD calculations and show a good agreement with the CFD upstream of locations where Mach discs occur.

In MOC results, the incident shock wave was clearly shown and not smeared. By applying a shock polar analysis in the (p, θ)-plane to the incident shock wave of an axisymmetric jet, it was shown that a Mach disc occurred in the region between the von Neumann point and the detachment point on the incident shock in the jet flow. More specifically, it is predicted that a Mach disc is likely to occur at the point where the flow angle behind the incident shock becomes $-5°$ relative to the axis in an underexpanded axisymmetric jet flow for the injection pressure ratios of 2 - 50. As a result, this minus 5 degree condition is suggested as a new criterion for locating a Mach disc in axisymmetric underexpanded jets. A correlation between the injection pressure ratio and the triple point location was derived using this new criterion. This correlation was validated by comparing with the experimental data of Graur *et al.*[33] and predicts the Mach disc location quite accurately for pressure ratios up to 2147.

The static pressure ahead of the incident shock wave plotted as a function of axial distance was found to fall on the same curve for nozzle-exit-to-ambient-pressure ratios of 2 - 50. Thus, in this pressure range, the static pressure upstream of the incident shock can be expressed as a function of only the axial distance from the nozzle exit.

The MOC computations of the jet flow with annular geometry were conducted for the pressure ratios of 10 and 20 with $r_{annulus}$ =10 - 50 units, $\triangle r$ = 2 units. In this pressure ratio, the MOC results did not predict a Mach disc in the core flow of the annular jet but do indicate the formation of a Mach disc where the jet meets the axis of symmetry. The MOC results display the annular jet configurations clearly. An outer incident shock much stronger than an inner incident shock was predicted to occur in the annular jet flow. Application of shock polar analysis was used to confirm this prediction. The Mach number and the stagnation pressure were found to decrease more rapidly at the inner jet boundary than at the outer jet boundary once he incident shocks met the jet boundary. Since there was no static pressure difference between the inner region and the outer region in these computations, it was determined that a geometric effect associated with the reduced radius at the inner jet boundary caused the collapse of the annular jet flow configurations to the axis of symmetry. MOC computations were performed for various specific heat ratios in order to study the effect of gas composition on the annular jet configurations. As the specific heat ratio of the issuing gas became smaller, the jet configuration became thicker and the jet flow met the axis of symmetry earlier.

Three new fuel valve nozzles were designed using the method of characteristics and basic compressible flow theory. The jet flows for each nozzle were analyzed and compared using CFD for both design and off-design valve pressure ratios. The newly designed nozzles showed much improved performance compared with conventional shrouded nozzles for all conditions examined. Of the three new designs the convergent-divergent nozzle performed best, the 15° conical nozzle was next and the Aerospike nozzle was third. The complex geometry in the interior of the valve caused substantial stagnation pressure losses even in subsonic flow regions. These affected both the overall performance of the valve-nozzle combination and the mass flow rate. Careful examination of the transonic flow in the valve using CFD was required to determine the location of the sonic surface, the geometry of the sonic surface and the stagnation pressure at the sonic surface. All were sensitive to valve geometry changes. Simply using the geometry minimum area of a given valve as the sonic area was found to be both inaccurate and inadequate for design purposes. For conical nozzles, 15° conical nozzle showed the best performance while a Mach disc occurred in 30° and 45° conical nozzles.

Bibliography

[1] Anderson, J. D. , Jr., 1990, *Modern Compressible Flow*, 2nd Ed., McGraw Hill, New York.

[2] Shapiro, A. H., 1953, *The Dynamics and Thermodynamics of Compressible Fluid Flow*, Vol. 1 and 2, The Ronald Press Co, New York.

[3] Liepmann, H. W., and Roshko, A., 1957, *Element of Gasdynamics*, John Wiley and Sons, New York.

[4] Zucrow, M. J., and Hoffman, J. D., 1977, *Gas Dynamics*, Vol. 1 and 2, John Wiley and Sons, New York.

[5] Love, E. S., and Grigsby, C. E., 1955, *Some Studies of Axisymmetric Free Jets Exhausting From Sonic and Supersonic Nozzles into Still Air and into Supersonic Streams*, NACA, RM L54L31.

[6] Ferri, A., 1946, "*Applicationof the Method of Characteristics to Supersonic Rotational Flow*," NACA, TR-841.

[7] Pack, D. C., 1948, "*On the Formation of Shock – Waves in Supersonic Gas Jets(Two – Dimensional Flow)*," *Quarterly Journal of Mechanics and Applied Mathematics*, Vol. 1, pp. 1-17.

[8] Wilcox, D. E., Weir, A., Jr., Nicholls, J. A., and Dunlap, R., 1957, "*Location of Mach Discs and Diamonds in Supersonic Air Jets*," *Journal of the Aeronautical Sciences*, Readers' Forum, Vol. 24, No. 2, pp. 150-152.

[9] Adamson, T. C., Jr., and Nicholls, J. A., 1959, "*On the Structureof Jets from Highly Underexpanded Nozzles into Still Air*," *Journal of the Aerospace Sciences*, Vol. 26, No. 1, pp. 16-24.

[10] Eastman, D. W., and Radtke, L. P., 1963, "*Location of the Normal Shock Wave in the Exhaust Plume of a Jet*," *AIAA Journal*, Vol. 1, No. 4, pp. 918-919.

[11] Crist, S., Sherman, P. M., and Glass, D. R., 1966, "*Study of the Highly Underexpanded Sonic Jet*," *AIAA Journal*, Vol. 4, No. 1, pp. 68-71.

[12] Abbett, M., 1971, "*Mach Disk in Underexpanded Exhaust Plumes*," *AIAA Journal*, Vol. 9, No. 3, pp. 512-514.

[13] Hall, C. R., Jr., and Mueller, T. J., 1972, "*Exploratory Analysis of Nonuniform Plug Nozzle Flowfields*," *Journal of Spacecraft and Rockets*, Vol. 9, No. 5, pp. 337-342.

[14] Fox, J. H., 1974, "*On the Structure of Jet Plumes*," *AIAA Journal*, Vol. 12, No. 1, pp. 105-107.

[15] Chang, I.-S., and Chow, W. L., 1974, "*Mach Disk from Underexpanded Axisymmetric Nozzle Flow*," *AIAA Journal*, Vol. 12, No. 8, pp. 1079-1082.

[16] Wang, B. N., and Hoffman, J. D., 1988, "*Calculation of Annular Nozzle Trisonic Flowfields by the Method of Characteristics*," *Journal of Propulsion and Power*, Vol. 4, No. 3, pp. 228-235.

[17] Hsu, A. T. and Liou, M.-S., 1991, "*Computation Analysis of Underexpanded Jets in the Hypersonic Regime*," *Journal of Propulsion and Power*, Vol. 7, No. 2, pp. 297-299.

[18] Hall, C. R., 1970, "*An Analytical and Experimental Study of Nonuniform Plug Nozzle Flowfields*," Ph.D. Thesis, University of Notre Dame, Notre Dame, IN.

[19] Fox, J. H., 1970, "*Axially Symmetric, Inviscid, Real Gas, Nonisoenergetic Flow Solution by the Method of Characteristics*," AEDCTR-69-184, Arnold Engineering Development Center, Arnold Air Force Station, TN.

[20] Chang, I.-S., 1973, "*Mach Reflection, Mach Disk, and the Associated Nozzle Free Jet Flows*," Ph.D. Thesis, University of Illinois at Urbana-Champaign, Urbana, IL.

[21] Wang, B. N., 1984, "*On the Method of Characteristics and Its Application to the Annular Nozzle Flowfields*," Ph.D. Thesis, Purdue University, West Lafayette, IN.

[22] Neumann, J. von, 1963, *Collected Works*, Vol. 6, pp. 239-299, Pergamon.

[23] Hornung, H. G., Oertel, H., and Sandeman, R. J., 1979, "*Transition to Mach Reflexion of Shock Waves in Steady and Pseudosteady Flow with and without Relaxation*," *Journal of Fluid Mechanics*, Vol. 90, Part 3, pp. 541-560.

[24] Hornung, H. G., 1986, "*Regular and Mach Reflection of Shock Waves*," *Annular Review of Fluid Mechanics*,Vol. 18, pp. 33-58.

[25] Chpoun, A., Passerel, D., Li, H., and Ben-Dor, G., 1995, "*Reconsideration of Oblique Shock Wave Reflections in Steady Flows. Part* 1. *Experimental Investigaton*," *Journal of Fluid Mechanics*, Vol. 301, pp. 19-35.

[26] Vuillon, J., Zeitoun, D., and Ben-Dor, G., 1995, "*Reconsideration of Oblique Shock Wave Reflections in Steady Flows. Part 2. Numerical Investigaton,*" *Journal of Fluid Mechanics*, Vol. 301, pp. 37-50.

[27] Ivanov, M. S., Gimelshein, S. F., and Beylich, A. E., 1995, "*Hysteresis Effect in Stationary Reflection of Shock Waves,*" *Physics of Fluids*, Vol. 7, No. 4, pp. 685-687.

[28] Li, H., and Ben-Dor, G., 1996, "*Application of the Principle of Minimum Entropy Production to Shock Wave Reflections. I. Steady Flows,*" *Journal of Applied Physics*, Vol. 80, pp. 2027-2037.

[29] Ivanov, M. S., Markelov, G. N., Kudryavtsev, A. N., and Gimelshein, S. F., 1998, "*Numerical Analysis of Shock Wave Reflection Transition in Steady Flows,*" *AIAA Journal*, Vol. 36, No. 11, pp. 2079-2086.

[30] Ivanov, M. S., 2000, "*Flow-Mach- Number-Variation-Induced Hysteresis in Steady Shock Wave Reflections,*" *AIAA Journal*, Vol. 39, No. 5, pp. 972-974.

[31] Gribben, B. J., Badcock, K. J., and Richards, B. E., 2000, "*Numerical Study of Shock-Reflection Hysteresis in anUnderexpanded Jet,*" *AIAA Journal*, Vol. 38, No. 2, pp. 275-283.

[32] Ben-Dor, G., Ivanov, M. S., Vasilev, E. I., and Elperin, T., 2002, "*Hysteresis Processes in the Regular Reflection $\leftrightarrow$ Mach Reflection Transition in Steady Flows,*" *Progress in Aerospace Sciences*, Vol. 38, pp. 347-387.

[33] Graur, I. A., Elizarova, T. G., Ramos, A., Tejeda, G., Fernandez, J. M., and Montero, S., 2004, "*A Study of Shock Waves in Expanding Flows on the Basis of Spectroscopic Experiments and Quasi-Gasdynamic Equations,*" *Journal of Fluid Mechanics*, Vol. 504, pp. 239-270.

[34] Kirkpatrick, A. T., Li, Y., and Mitchell, C. E., 2001, "*Analytical and Computational Modeling of High Pressure Gas Injection,*" *ASME Fall* 2001 *ICE Conference.*

[35] Olsen, D., and Willson, B., 2001, "*Planar Laser Induced Fluorescence Imaging of Gas Injection from Fuel Valves for Large Bore Natural Gas Engines,*" *ASME Fall* 2001 *ICE Conference.*

[36] Kim, G.-H., Kirkpatrick, A. T., and Mitchell, C. E., 2003, "*Computational Modeling of Natural Gas Injection in a Large Bore Engine,*" *ASME Journal of Engineering for Gas Turbines and Power*, in review.